



NTNU – Trondheim
Norwegian University of
Science and Technology

NANOMECHANICAL TESTING OF CGHAZ OF ARCTIC STEEL

Brage Dahl Snartland

Materials Science and Engineering

Submission date: June 2015

Supervisor: Christian Thaulow, IPM

Norwegian University of Science and Technology
Department of Engineering Design and Materials

THE NORWEGIAN UNIVERSITY
OF SCIENCE AND TECHNOLOGY
DEPARTMENT OF ENGINEERING DESIGN
AND MATERIALS

**MASTER THESIS SPRING 2015
FOR
STUD. TECHN. BRAGE SNARTLAND**

Nanomechanical Testing of CGHAZ of Arctic Steel

Nanomekanisk prøving av CGHAZ av et arktisk stål

The activity in the Arctic areas is on the increase. The exploration of these areas requires high quality materials due to the harsh climate conditions and low temperatures down to -60°C. Understanding material deformation mechanisms under these environmental conditions can help prevent dangerous failure from occurring and allow for the development of both robust and cost-efficient materials. In order to be able to understand the local properties of complex microstructures it is crucial to understand the fundamental deformation mechanisms. The rapid developments within nanotechnology have made it possible to get a detailed characterization of the material by means of nanomechanical testing methods.

In this Thesis focus is to modify the existing testing equipment for low temperature testing and then to characterize the microstructure and quantify the nanomechanical material properties of the Coarse Grained Heat Affected Zone (CGHAZ) of a steel developed for use under arctic conditions.

The following tasks shall be performed:

- The cooling system in ESEM/picoindenter shall be modified in order to obtain reliable temperature control. This shall be done in close cooperation with stud techn Aksel L L Kvaal and PhD student Anette Brocks Hagen, and verified with limited tests of pillars and beams extracted from pure iron.
- The next step is to select an arctic steel in close cooperation with the research project "Arctic Materials". Present the weld thermal simulation testing and the properties obtained after screening testing.
- Microstructural characterization of the microstructure of the CGHAZ
- Mapping of mechanical properties with nanoindentation testing
- Nanomechanical testing with pillars and beams
- Initial testing at room temperature, but the intention is to include lower temperatures, down to minus 90°C.

Formal requirements:

Three weeks after start of the thesis work, an A3 sheet illustrating the work is to be handed in. A template for this presentation is available on the IPM's web site under the menu

“Masteroppgave” (<http://www.ntnu.no/ipm/masteroppgave>). This sheet should be updated one week before the master’s thesis is submitted.

Risk assessment of experimental activities shall always be performed. Experimental work defined in the problem description shall be planned and risk assessed up-front and within 3 weeks after receiving the problem text. Any specific experimental activities which are not properly covered by the general risk assessment shall be particularly assessed before performing the experimental work. Risk assessments should be signed by the supervisor and copies shall be included in the appendix of the thesis.

The thesis should include the signed problem text, and be written as a research report with summary both in English and Norwegian, conclusion, literature references, table of contents, etc. During preparation of the text, the candidate should make efforts to create a well arranged and well written report. To ease the evaluation of the thesis, it is important to cross-reference text, tables and figures. For evaluation of the work a thorough discussion of results is appreciated.

The thesis shall be submitted electronically via DAIM, NTNU’s system for Digital Archiving and Submission of Master’s theses.



Torgeir Welo
Head of Division



Christian Thaulow
Professor/Supervisor

Abstract

An ever increasing demand for energy is forcing the oil industry to push technology forward, as new oil rich fields are discovered further North. The Arctic offers a harsh, cold climate, leading to new challenges within the field of materials technology. Offshore and onshore Arctic production demand strong, and tough materials, able to withstand temperatures down to -60°C , in addition to extreme weather. As the temperature drops the risk for brittle material failure will increase. Understanding material deformation and governing mechanisms under such conditions can prevent material failure, while maintaining cost-efficiency.

Application of nanomechanical testing methods has become increasingly important within materials research. Understanding material properties at the micro- and nano-level, has attracted significant interest. Most small-scale experiments have been conducted at room temperature, as this requires a less complex set-up. However, testing of Arctic steels requires low temperature small-scale experiments to obtain material performance in its field of operation.

The scope of this thesis was to modify existing cryogenic experimental equipment. Characterization of regions in a weld simulated zone of a steel developed for use under Arctic conditions, was to be conducted. Additionally, establishing nanomechanical properties was desired. The approach was to machine micro-sized cantilevers and pillars, using a focused ion beam. The specimens were loaded, and compressed, at room temperature, and at approximately -80°C . The in-house made and modified cryogenic set-up enabled highly accurate low temperature nanomechanical testing. A nanoindenter was utilized to map the hardness at the micro-level, obtaining the variations of hardness in the microstructure.

This thesis yielded interesting results regarding hardness, nanomechanical material properties and testing methods. However, pushing the equipment beyond its specifications resulted in experimental data requiring compensation for several unforeseen effects. The critical stress intensity factors were calculated through the J-integral for both pure iron and steel cantilevers. Pillar compression to obtain the microstructure yield strength, was also conducted, all contributing to the characterization of the microstructure and nanomechanical properties of the steel.

Sammendrag

Et økende, globalt energikrav tvinger oljeindustrien nordover, hvor oljerike reservoarer har blitt oppdaget i senere tid. Områdene nord for polarsirkelen har temperaturer under -60°C og hardt vær, noe som introduserer nye utfordringer innen materialteknologi. Offshore og landbasert oljeproduksjon krever sterke, motstandsdyktige materialer kapable til å håndtere det krevende klimaet. Lave temperaturer øker risikoen for sprøbrudd. Innsikt og forståelse av de grunnleggende deformasjons- og bruddmekanismene under slike forhold kan hindre materialkollaps, samtidig som kostnadsnivået holdes nede.

Bruk av nanomekaniske testmetoder har blitt viktige innen forskning på materialer. Muligheten til å fastslå materialegenskaper på mikro- og nano-nivå, gjennom grundig karakterisering av materialegenskaper, har fått mye oppmerksomhet. Lavtemperatur nanomekanisk forskning krever modifikasjon av utstyr, og har derfor ikke blitt gjennomført i særlig stor grad.

Denne masteroppgaven har som mål å modifisere egenutviklet kryogenisk utstyr, slik at eksperimenter ved lav temperatur kan gjennomføres. Karakterisering av sveisesimulerte mikrostrukturer i et stål utviklet til arktiske regioner ble gjennomført. Nanomekaniske egenskaper skal også testes og etableres. Dette ble gjort ved å maskinere pilarer og bjelker i mikrometerskala ved hjelp av en fokusert ionestråle. Prøvene ble lastet ved romtemperatur og ved omtrent -80°C . Det modifiserte eksperimentelle utstyret kan laste prøvene med høy nøyaktighet ved lave temperaturer. En nanoindenter ble brukt til å kartlegge variasjoner i mikrostrukturens hardhet på nanonivå.

Masteroppgaven ga flere interessante resultater vedrørende hardhet, materialegenskaper på nanonivå, nanomekaniske testmetoder og prøvepreparering. Det eksperimentelle arbeidet presset utstyret forbi dets designede grenser, noe som resulterte i nødvendig kompensasjon for uforutsette effekter. Den kritiske spenningsintensiteten ble beregnet for bjelker i rent jern og stål, ved å regne ut J-integralet. Kompresjon av pilarene ble gjennomført, hvor flytespenningen ble fastslått. Alle testene bidro til karakterisering av mikrostrukturen og de nanomekaniske egenskapene til stålet.

Preface

This report is the master thesis written, and conducted, during the final semester of a Master of Science degree in Materials Science and Engineering at The Norwegian University of Science and Technology. The master thesis was conducted at the Department of Engineering Design and Materials. This report is a partial requirement for a masters degree at the university, and serves as a documentation of the performed work.

As stated in the problem text, the design of the experimental set-up, and the complete experimental procedure, is done in close cooperation with Aksel Louis Legouy Kvaal and PhD candidate Anette Brocks Hagen. Due to similarities in the problem texts for these theses, parts of the report is written as a collaboration between Aksel Louis Legouy Kvaal and Brage Dahl Snartland. This is done in agreement with, and encouraged by, our common supervisor, Christian Thaulow. The following sections are written in collaboration:

- Preface.
- Abstract.
- Sammendrag.
- Introduction.
- Theoretical background.
- Experimental procedure.
- Results and discussion regarding nanoindentation and characterization
- Results and discussion regarding pure iron experiments and a comparison between the weld simulated microstructures.
- Further work.
- Acknowledgments.

Results and discussion regarding the welded microstructure specimens, and conclusion are written independently. The workload has been divided equally between Brage Dahl Snartland and Aksel Louis Legouy Kvaal. Section 4.6 'Experiments and Atomistic Modeling' is a collaboration between Brage Dahl Snartland, Aksel Louis Legouy Kvaal and Marie Jørum.

An extensive amount of work has been laid down in the further development of the cryogenic system at the IPM Nanomechanical Lab. The design process proved challenging, and several time consuming trials were conducted. This was crucial due to the delicate nature of the Hysitron PI-85 PicoIndenter. Representatives from Hysitron, and research groups at UC Berkley and CalTech, were consulted in order to finalize the experimental set-up.

The experimental work was delayed several times due to downtime and high demand on the NTNU NanoLab Focused Ion Beam, and the IPM Nanomechanical Lab ESEM. Most of the experimental work had to be conducted during nighttime, holidays and weekends. Achieving the desired surface roughness suitable for the planned experiments, proved challenging using traditional polishing tools. The majority of the semester has been dedicated to optimizing the experimental

procedure.

Posters presenting the thesis were prepared, and a risk assessment was conducted for the planned work. These are included in the appendix.

The 11th of February, the work from the specialization project, and the planned work for the master thesis, was presented at the Gray Goo Symposium. This was an event where all students doing work related to nanotechnology may present their work. The event was organized by the nanotechnology students and NTNU NanoLab.

Nomenclature

A	Projected Contact Area
A_{pl}	Area Beneath the Load-Displacement Curve
C_0	Particle Diameter
$C_{0,b}$	Thickness of Grain Boundary Particle
E	Young's Modulus of Elasticity
E_r	Reduced Modulus of Elasticity
F	Bending Force
F_Q	Determining Force
G	Shear Modulus
H	Hardness
I	Moment of Inertia
J	J-Integral
K_Q	Preliminary Stress Intensity Factor
K_{IC}	Critical Stress Intensity Factor for Mode I Fracture
$K_{Q,J}$	Preliminary Stress Intensity Factor Based on the J-Integral
L	Bending Length
P_f	Probability of Fracture
P_{max}	Maximum Load
S	Stiffness
T_P	Peak Temperature
T_c	Critical Temperature
U	Strain Energy Stored in the Body
U^*	Complimentary Strain Energy
Δ	Compression Displacement
Δa	Crack Extension
$\Delta t_{8/5}$	Cooling Time from 800 – 500 °C
α	Ferrite
ϵ	Engineering Strain
η	Constant Factor (=2)
γ	Austenite
γ'	Effective Surface Energy

Nomenclature

γ_p	Plastic Work Required to Create New Surface
\mathcal{G}	Energy Release Rate
ν	Poisson's Ratio
ω	Plastic Zone Length
ρ	Dislocation density
σ_I	Local Maximum Stress
σ_f	Fracture Stress
σ_y	Yield Strength
σ_{MA}	Stress in a MA Constituent
σ_{mm}	Strength of a High-Angle Bainite Boundary
σ_{pm}	Strength of a Particle-Matrix Interface
τ	Shear Stress
τ_i	Friction Stress
τ_p	Peierls Stress
τ_y	Yield Shear Stress
τ_{eff}	Effective Shear Stress
a	Notch Depth
$a_{pl.sp.}$	Atomic Plane Spacing
a_{planes}	Distance Between Slipped Planes
b	Cantilever Thickness
b^*	Pentagonal Cantilever Thickness Approximation
b_v	Burger's Vector
$b_{at.sp.}$	Atom Spacing
d	Average Grain Size
d_b	Distance to Grain Boundary
d_n	Shih Factor
d_{top}	Pillar Top Diameter
$f\left(\frac{a}{b}\right)$	Dimensionless Shape Factor
h	Indenter Displacement
h_0	Initial Pillar Height
h_c	Impression Depth
h_p	Pile-Up Height
k	Unloading Stiffness
k_y	Dislocation Pile-Up Constant

l_0	Initial Internal Crack Length
l_0^c	Critical Internal Crack Length
m	Schmid Factor
q	Heat Input
r	Distance to Fusion Boundary
r_p	Rotational Factor
w	Cantilever Width
$w_{disl.}$	Dislocation Width
y	Vertical Distance Between the Upper Surface and the Neutral Plane
AFM	Atomic Force Microscope
ASTM	American Society for Testing and Materials
BCC	Body-Centered Cubic
CCT	Continuous Cooling Transformation
CGHAZ	Coarse Grained Heat Affected Zone
CMOD	Crack Mouth Opening Displacement
CTOD	Crack Tip Opening Displacement
DBTT	Ductile to Brittle Transition Temperature
FCC	Face-Centered Cubic
FIB	Focused Ion Beam
GND	Geometrically Necessary Dislocation
HAZ	Heat Affected Zone
HCP	Hexagonal Close Packed
HSLA	High-Strength Low-Alloy
ICCGHAZ	Intercritically Reheated Coarse Grained Heat Affected Zone

Nomenclature

LEFM	Linear Elastic Fracture Mechanics
MA	Martensite-Austenite
MBM	Multiple Barrier Model
RT	Room Temperature
SEM	Scanning Electron Microscope
TTT	Time-Temperature-Transformation
UTS	Ultimate Tensile Strength

Contents

1	Introduction	1
2	Theoretical Background	3
2.1	The Heat Affected Zone	3
2.1.1	Heat Flow	4
2.1.2	Coarse Grained Zone	5
2.1.3	Intercritically Reheated Coarse Grained HAZ	6
2.1.4	MA Constituents	6
2.2	Deformation and Defects	8
2.2.1	Dislocations	8
2.2.2	Lomer-Cottrell Locking	11
2.2.3	Dislocation Movement in Cantilevers	12
2.3	Fracture Mechanisms	15
2.3.1	Ductile Fracture	15
2.3.2	Cleavage Fracture	15
2.3.3	Cleavage Fracture Initiation	16
2.3.4	Peierls Stress and Peierls-Nabarro Force	19
2.3.5	Ductile to Brittle Transition Temperature	21
2.3.6	Smith's Model	22
2.3.7	Beremin Model	22
2.3.8	Multiple Barrier Model	24
2.4	Linear Elastic Fracture Mechanics Approach	26
2.4.1	Determination of Crack Growth	28
2.4.2	Cantilevers with a Pentagonal Cross Section	28
2.5	Elastic-Plastic Fracture Mechanics Approach	30
2.5.1	J-Integral	32
2.5.2	Crack Tip Opening Displacement	35
2.6	Nanoindentation	36
2.7	Pillar Compression Testing	41
2.8	Focused Ion Beam	43
3	Experimental Procedure	45
3.1	Material and Sample Preparation	45
3.2	Machining of Test Specimen	46
3.2.1	Cantilevers	47
3.2.2	Pillars	50
3.3	Nanoindentation	53
3.4	Low Temperature Nanomechanical System	53
3.5	Pillar Compression	55

CONTENTS

3.6	Fracture Mechanical Testing of Cantilevers	56
4	Results and Discussion	63
4.1	Characterization of the Microstructure	63
4.1.1	SINTEF Weld Screening	64
4.2	Nanoindentation	65
4.3	Determination of Young's Modulus of Elasticity	67
4.4	Determination of Yield Strength	69
4.5	Iron Cantilevers	72
4.5.1	Cantilever Loading	72
4.5.2	Crack Growth	75
4.5.3	J-Integral	77
4.5.4	Crack Tip Opening Displacement	77
4.5.5	Stress Intensity Factor	79
4.6	Experiments and Atomistic Modeling	81
4.7	CGHAZ Cantilevers	84
4.7.1	Cantilever Loading	84
4.7.2	Crack Growth	84
4.7.3	J-Integral	88
4.7.4	Crack Tip Opening Displacement	88
4.7.5	Stress Intensity Factor	91
4.8	CGHAZ Pillars	92
4.9	Pure iron, CGHAZ and ICCGHAZ cantilevers	94
4.10	Gallium implantation	96
5	Conclusion	97
6	Further Work	98
7	Acknowledgements	99
	References	101
A	Sample dimensions	109
B	Risk Assessment	111
C	A3-Posters	124
D	SEM Images of Cantilevers and Pillars	126
D.1	Cantilever Fe3	126
D.2	Cantilever Fe4	128

D.3	Cantilever 1-1 CGHAZ	131
D.4	Cantilever 1-2 CGHAZ	133
D.5	Cantilever 2-3 CGHAZ	135
D.6	Cantilever 2-4 CGHAZ	137
D.7	Cantilever 2 ICCGHAZ	140
D.8	Cantilever 3D ICCGHAZ	142
D.9	Cantilever 4 ICCGHAZ	144
D.10	Cantilever 5D ICCGHAZ	146
D.11	Pillar 4-1 CGHAZ	148
D.12	Pillar 4-2 CGHAZ	149
D.13	Pillar 6-1 CGHAZ	150
D.14	Pillar 6-2 CGHAZ	151
D.15	Pillar 7 ICCGHAZ	152
D.16	Pillar 8 ICCGHAZ	153
D.17	Pillar 10 ICCGHAZ	154
D.18	Pillar 11 ICCGHAZ	155

CONTENTS

1 Introduction

The industrial activity in the Arctic is rapidly increasing. An ever increasing demand for energy is forcing the production of oil further north, where accidents may cause severe ecological ramifications. Rough climate conditions and temperatures as low as $-60\text{ }^{\circ}\text{C}$ require materials with specialized mechanical properties. The materials must display sufficient fracture and wear resistance at low temperatures, while avoiding excessive maintenance and maintaining lifetime integrity.

A strong fundamental understanding of active deformation mechanisms is essential in order to understand the local properties of materials with complex microstructures. The rapid development within the field of nanotechnology and nanomechanical testing methods, enables detailed characterization of material properties. The specimens used in this thesis are machined using a focused ion beam at NTNU NanoLab. The focused ion beam enables machining of precise specimen relatively cost-efficiently. It has therefore become a common instrument when machining micro- and nano-scale specimens. The specimens are subjected to nanomechanical testing methods at room temperature and at $-80\text{ }^{\circ}\text{C}$. The sample containing the machined specimens is loaded in a Hysitron PI-85 PicoIndenter, inside an ESEM.

Pillars and cantilevers were machined from both pure iron and a weld simulated steel microstructure. The specimen dimensions and crystallographic orientations were set to correspond to previously executed research conducted at NTNU. The scope of this thesis is listed below:

- Modification of the existing cryogenic testing system at the Nanomechanical lab at IPM.
- Verification of the experimental set-up by performing nanomechanical tests with pure iron specimen.
- Present weld thermal simulation testing.
- Characterization of the weld simulated microstructure.
- Mapping of the mechanical properties by nanoindentation.
- Low temperature nanomechanical testing of pillars and cantilevers.

2 Theoretical Background

Section 2 outlines the most relevant theoretical aspects of this thesis. Some of the theoretical aspects are used directly in calculations and discussion, and some aspects are included to serve as a basis in order to understand the more advanced subsections. The leitmotif of this section is the understanding of what fracture toughness at the micro-level actually is, and how to benefit from conducting experiments at the micro-scale.

This section presents aspects revolving the relevant microstructures in this thesis. Dislocations in, and deformation of these microstructures serve as a basis for understanding the active mechanisms during fracture. Understanding these mechanisms and microstructures, enables insight into the presented fracture models and mechanics.

2.1 The Heat Affected Zone

Fusion welding is integral to the fabrication of steel structures. There are a number of ways fusion welding is performed, but all methods involve the deposition of a small amount of molten steel in a gap between two components. When the molten steel solidifies, the two components are joined. The metallurgy of the weld can be divided into two major regimes, the fusion zone, and the heat affected zone. The fusion zone is the region of the weld characterized by metal previously in the liquid state, with a solidification microstructure, while the HAZ is any region adjacent to the weld, which has incurred an altered microstructure without entering the liquid state as a result of heat input from the welding process [11, p.287].

Within the HAZ it is desirable to categorize characteristic microstructural zones. There is a well-defined gradient directly correlated to the amount of heat transferred to the surrounding microstructures. This leads to local zones with varying mechanical properties as a function of distance to the fusion boundary [11, p.299]. The local zones and their respective temperature regimes are illustrated in Figure 1. The regions closest to the weld metal are heated to high temperatures and are completely transformed to austenite, γ . Although depending on the alloy composition, the microstructure is typically completely transformed at $\approx 950^\circ\text{C}$ [11, p.299]. The peak weld temperature is well beyond 950°C causing the transformed γ to be annealed, giving rise to the coarse grained zone. At greater distances from the fusion zone the temperatures will not be high enough to cause full annealing, and the grains will not become as coarse, yielding a fine grained zone. Beyond the fine grained zone the heat input is not sufficient to completely transform to austenite, and a partially transformed zone is formed. Outside some threshold distance from the weld, in the subcritical zone, the temperature will not exceed $\approx 950^\circ\text{C}$, and no γ will form [11, p.299][30].

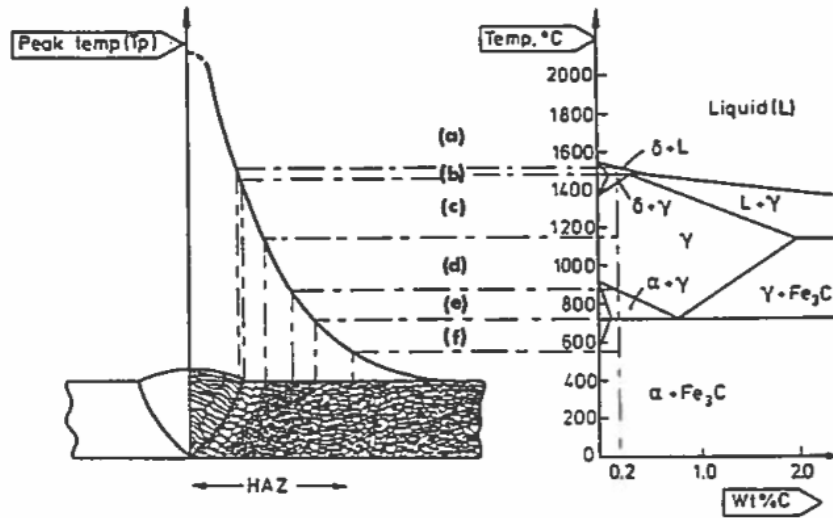


Figure 1: Schematic illustration of the different regions of the HAZ of steel welds and their definition; a) weld metal / fusion zone; b) partially melted zone; c) coarse grained zone (CGHAZ); d) fine grained zone; e) partially transformed zone; f) subcritical zone. Adapted from [30, p.111].

2.1.1 Heat Flow

During welding the HAZ experiences a heating and cooling cycle. The severity of this thermal cycle is dependent on several parameters. The peak temperature, T_P , and the heating rate decrease with distance from the fusion boundary. The cooling rate, on the other hand, is less sensitive to this distance, and is commonly referred to as the time taken to cool over the range 800 – 500 °C; denoted $\Delta t_{8/5}$. This time is crucial for the degree of solid-state transformation of austenitic to ferritic phases.

T_P and $\Delta t_{8/5}$ can be used to describe the thermal cycle at any point in the HAZ. These two parameters increase with the heat input, q [11, 298]:

$$T_P \propto \frac{q}{r}$$

$$\Delta t_{8/5} \propto q^n$$

where r is the distance from the fusion boundary and n has a value (1 or 2), depending on whether the welded component is thick relative to the size of the weld bead. The relative thickness determines whether the heat flow can be considered two- or three-dimensional. This is illustrated in Figure 2 [11, p.299].

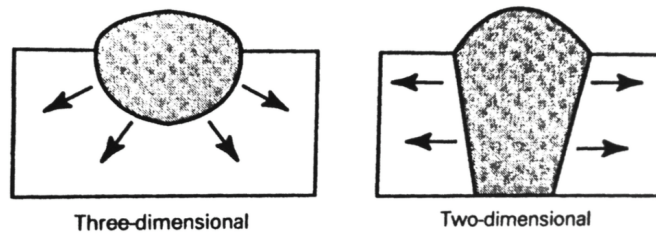


Figure 2: Schematic illustration of two- and three-dimensional heat-flow conditions. Adapted from [11, p.299].

2.1.2 Coarse Grained Zone

The CGHAZ is the weld region that experiences the highest T_P without partially melting. The high temperatures can lead to significant austenite coarsening. The combination of a coarse austenite grain size and rapid cooling rates promote brittle microstructures, which contain high proportions of ferrite side-plates and bainite [61]. The formation of ferrite during cooling of the weld is dependant on the kinetic behavior, which may be determined by C-shaped curves on a TTT diagram, or CCT diagram. These diagrams describe the transformation rate, governed by two opposing factors; rate of diffusion and transformation driving force, both of which are functions of temperature [11, p.301][55].

The CGHAZ experiences T_P ranging from ~ 1100 to 1450 °C. Low density grain boundaries typically prelude full transformation to ferrite, α , during cooling. This leads to a more complex microstructure compared to the parent metal. The complexity is caused by the wide variety of possible transformation products; polygonal ferrite, Widmannstätten ferrite, bainitic ferrite and lath martensite. In addition to these, many carbon rich phases associated with the above mentioned ferrites, may transform into pearlite, degenerate pearlite, carbides and MA particles. The final microstructure in the CGHAZ will be strongly controlled by the alloy composition, $\Delta t_{8/5}$ and the parent material inclusion density [34]. Bainitic lamella and needle structure affect the microstructural properties in the CGHAZ. These formations are illustrated in Figure 3. These phases typically nucleate at γ grain boundaries, and follow the Kurdjumov-Sachs crystallographic orientation. Bainite packet boundaries influence the brittle fracture properties [55][89]. The phase transformation from γ to bainite is done through shear transformation and high density dislocation glide by a military movement of atoms.

As the peak temperature is approached, the coarsening of the grains will become more rapid. For HSLA steels the grain boundary pinning particles will control the coarsening before they are dissolved. Large grains have a higher hardenability than smaller grains, which leads to a more brittle microstructure susceptible to different undesired effects, e.g. atomic hydrogen [11, p.304].

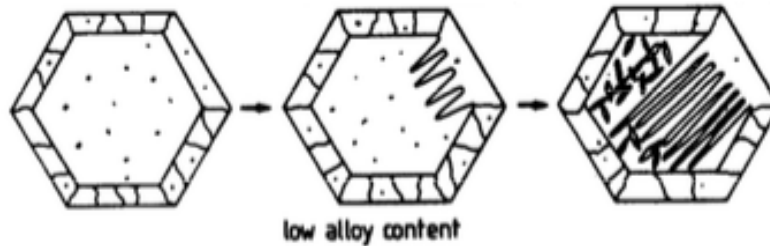


Figure 3: Schematic illustration of bainite transformation at γ grain boundaries in a low-alloy steel. Adapted from [38].

2.1.3 Intercritically Reheated Coarse Grained HAZ

Historically, the lowest toughness was expected in the CGHAZ. However, in recent years it has been found that the region of highest degradation in the HAZ occurs in the intercritically reheated coarse grained heat affected zone [61]. The ICCGHAZ is the region of the CGHAZ reheated to temperatures between $A_{c1} < T_{p2} < A_{c3}$ by subsequent welding passes [4]. A schematic diagram of the HAZ produced during multipass welding is displayed in Figure 4. The peak temperature of the intercritical thermal cycle is typically between 820 °C and 770 °C [37]. During the intercritical thermal cycle, partial transformation to austenite occurs, particularly where austenite stabilisers, such as carbon or manganese, are segregated in the initial microstructure. These areas include pearlite/bainite colonies [61]. The high carbon regions transform to pearlite/bainite or MA constituents upon cooling, depending on the hardenability of the austenite and the cooling rate. The MA phase is a high carbon martensite with some retained austenite.

2.1.4 MA Constituents

The presence of MA constituents is generally regarded as the major factor which reduces the HAZ toughness [4]. For HSLA steels, it has been found that the CGHAZ and the ICCGHAZ show the worst properties. C.L. Davis and J.E. King found that the ICCGHAZ microstructure consisting of upper bainite, with large prior austenite grain size, and blocky MA particles located at the prior austenite grain boundaries, showed the worst toughness properties during CTOD and Charpy V impact testing. The MA particles were determined to have significantly higher hardness than the bulk bainitic microstructure [22].

P. Mohseni et al. [66] conducted thorough investigation of cleavage fracture initiation in a HSLA steel. The paper concluded that the cracks initiated either from debonded MA constituents or from the region between two or more closely separated MA particles. In the paper the most important aspects of cleavage mechanisms related to the MA constituents are described:

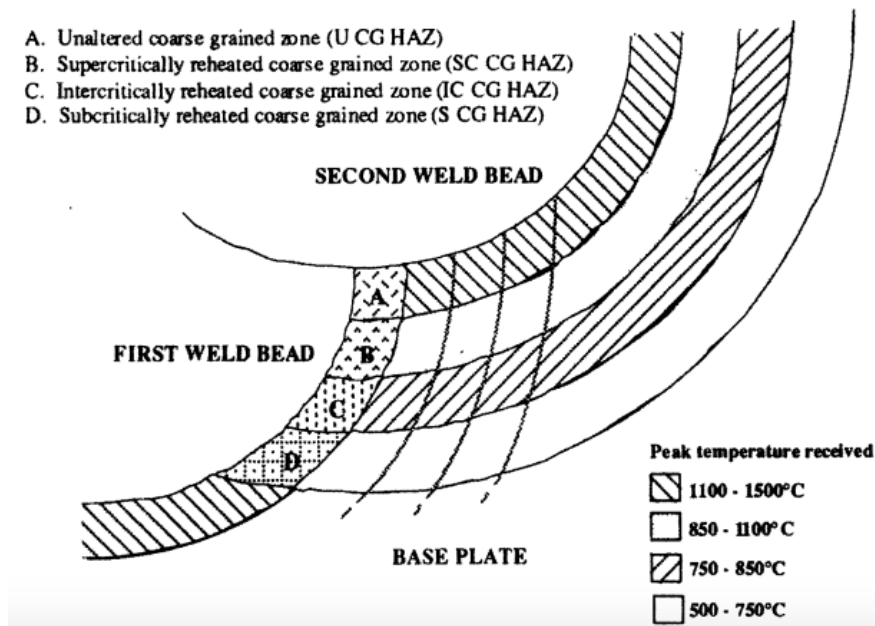


Figure 4: Schematic diagram of the HAZ produced during multipass welding. Adapted from [22].

1. **The MA phase is brittle** and cracks readily, which may promote cleavage fracture initiation. This effect becomes more important for the blocky constituents at lower temperatures. The stringer type MA phases have shown to crack readily and provide no effective obstacle to crack propagation.
2. **Residual stresses** induced by transformation are produced in the surrounding ferrite matrix. Austenite forms at prior austenite grain boundaries and transforms to MA constituents during cooling. The transformation from FCC to BCC results in a volume expansion, introducing stress concentrations in the surrounding matrix. The proximity of two or more blocky MA phases generates overlapping stress and strain fields that amplify the stress concentrations.
3. **The hardness** of the MA constituents is significantly higher than that of the surrounding matrix. During deformation, the difference in hardness promotes stress concentration and eventually cleavage fracture. Upon loading, the matrix will deform plastically and an internal stress may be generated close to the MA constituents, especially in the area between two or more closely located MA constituents. A large stress will develop across the interface which may cause the MA constituents to debond from the matrix.
4. **Debonding** at the MA-matrix interface introduces microcracks that propagate in a brittle manner or by linking with other debonded regions [21][60][66][67].

A later study, by some of the same authors, concluded that the presence of the MA phases is the dominant factor in determining the toughness of the welded microstructures. A correlation

was identified between fracture toughness and both the area fraction and the maximum size of MA particles [61]. The findings by P. Mohseni et al. is in agreement with earlier work and experiments conducted by C.L. Davis and J.E. King, which revealed that two closely spaced blocky MA particles are cleavage initiation sites [22][21].

2.2 Deformation and Defects

With sufficient stress a material deforms. It is convenient to divide the deformation mechanism into two stages, the elastic stage and the plastic stage. The elastic stage originates from stretching of interatomic bonds. When the applied stress is relieved, the material returns to its initial state. If stress is instead increased to a critical value, the plastic stage is initiated. During the plastic stage, interatomic bonds are broken and rebuilt, which leaves permanent changes.

To understand the principles of deformation it is convenient to consider a single crystal, meaning that all the atoms are part of the same periodic pattern. Even though all the atoms are part of the same periodic crystal structure, the arrangement of atoms in most crystalline materials is not perfect. The regular patterns are interrupted by crystallographic defects, such as vacancies, interstitials, impurities, line dislocations, or planar defects like stacking faults. Around these type of defects the surrounding planes bend around the defect to allow the crystal structure to achieve perfection on either side. Frenkel calculated the theoretical strength of a material [26]. The theoretical strength is the stress a material without defects can endure without inducing plastic deformation. In a perfect material the deformation occurs by a military movement of atoms. This requires a very high shear stress, τ , given by [23]:

$$\tau = \frac{Gb_{at.sp.}}{2\pi a_{pl.sp.}} \cdot \sin\left(\frac{2\pi x}{b_{at.sp.}}\right) \quad (1)$$

where G is the shear modulus, $b_{at.sp.}$ is the atomic spacing, $a_{pl.sp.}$ is the atomic plane spacing, and x is the distance displaced. However, defect free structural materials do not exist; deformation by dislocation movement is the main deformation mechanism in structural metals. In well-annealed metal crystals, the dislocation density, ρ , is usually between 10^{10} and $10^{12} \frac{m}{m^3}$, but it increases rapidly with plastic deformation. A typical value for a heavily cold-rolled metal is about 10^{14} to $10^{15} \frac{m}{m^3}$ [40, p.19].

2.2.1 Dislocations

The term dislocation, referring to a defect on the atomic scale, was coined by G.I. Taylor in 1934 [92]. There are two primary types of dislocations, edge and screw. In addition, one can combine both for a mixed type of dislocation. Edge dislocations are the easiest to describe and can be considered as an inserted half plane. In Figure 5a an edge dislocation is schematically illustrated.

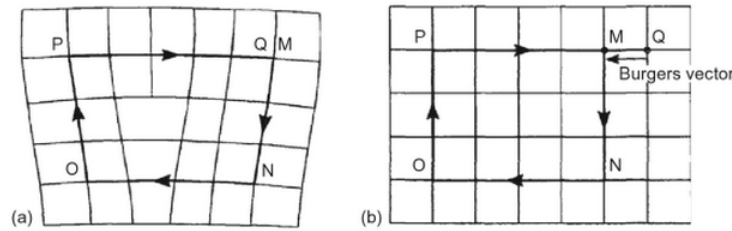


Figure 5: a) Burgers circuit round an edge dislocation; b) the same circuit in a perfect crystal; the closure failure is the Burgers vector. Adapted from [40, p.17].

When the lattice in (a) is compared to that of a perfect lattice (b) an additional vector is needed to close the circuit. This is called the Burgers vector; it represents the magnitude and direction of the lattice distortion. The Burgers vector of an edge dislocation is normal to the line of the dislocation. Upon plastic deformation, the inserted half plane will break existing atomic bonds and form new ones. It will continue to propagate in this manner until the dislocation is forced to stop, or it has moved through the crystal and formed an edge. The edge dislocation can slip in a direction parallel to the Burgers vector enabling it to *climb*. Dislocation climb is dependant on the diffusion rate because the mechanism is fundamentally dependent on the upward or downward diffusion of atoms.

In Figure 6 a screw dislocation is schematically illustrated and the Burgers vector identified. For a screw dislocation, the Burgers vector is parallel to the line of the dislocation [40, p.16-17]. This limits the number of atomic planes suitable for propagation exclusively to the denser atomic planes. The $\{110\}$ planes in a BCC structure are an example of a plane dense enough for screw dislocation propagation [23]. However, once nucleated, the screw dislocations are less restricted in terms of propagation compared to an edge dislocation, and the screw dislocation is able to glide in any plane that contains the dislocation. This gives the screw dislocations increased mobility, enabling them to change plane of propagation, called *cross-slip*, which is illustrated in Figure 7. Cross-slip causes a surface to show wavy slip lines after plastic deformation [23].

Every material has a critical temperature, T_c , defined as the temperature where the edge and screw dislocations are equally mobile, implying that the flow stress will be insensitive to the temperature. This temperature is important since it dictates what deformation mechanism is governing the deformation. If a material is deformed at temperatures below the critical temperature, cross-slip will dominate the deformation and wavy slip lines will occur throughout the sample [78]. The critical temperature varies between BCC materials, explained by the variation in atomic bond strength, i.e., a variation in the Peierl's potential [79].

Twinning deformation is another important mechanism. Deformation by twinning is explained by a local change in lattice orientation, mirrored over a plane. This mode of deformation com-

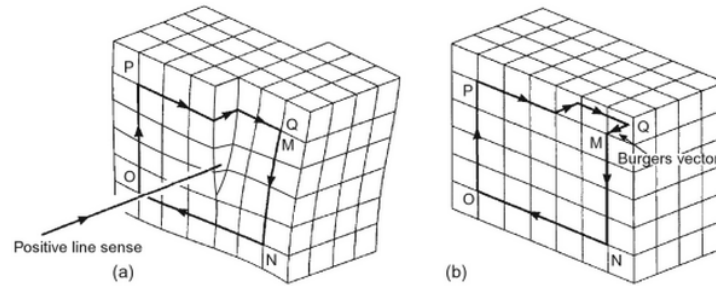


Figure 6: a) Burgers circuit around a screw dislocation; b) the same circuit in a perfect crystal; the closure failure is the Burgers vector. Adapted from [40, p.17].

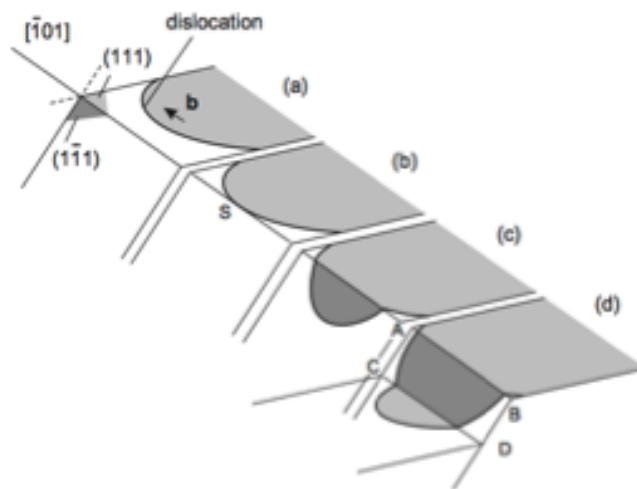


Figure 7: Illustration of cross-slip for a screw dislocation changing planes of propagation. Adapted from [36].

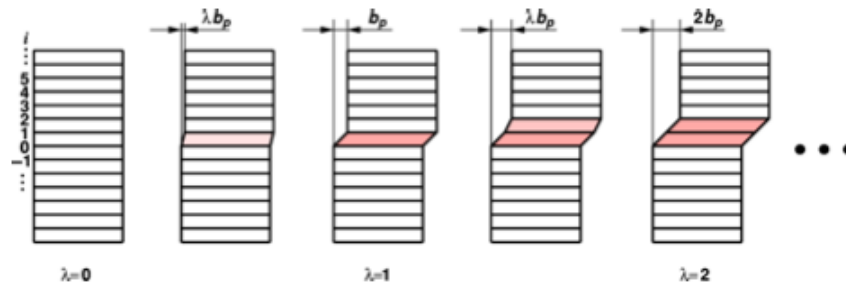


Figure 8: Illustration of deformation twinning. λ represents a fraction indicating a relative position. Adapted from [2].

petes with deformation by slip in metals, and is illustrated in Figure 8. Twinning deformation, if nucleated, may dominate dislocation slip [59]. Nucleation of twinning deformation requires more energy than nucleation and movement of screw dislocations. As the temperature is lowered, the stress build-up necessary to move dislocations increases, favoring twinning [2].

Curved dislocations are important when considering the mechanical properties of metals. At an atomistic scale, curved dislocations consist of short straight segments with sharp corners: kinks and jogs. The kink is a dislocation shifting one atomic distance in a direction perpendicular to the dislocation line, fully contained in the glide plane, illustrated in Figure 9. The dislocation propagation may then be recognized as kinks moving laterally along the dislocation line, increasing a dislocation's mobility [39]. Some dislocations form double-kinks, meaning that the dislocation shifts back into the original dislocation line. This is considered as a fault in the dislocation line. After a double-kink is formed, the two single kinks may separate, causing the dislocation to propagate. However, separated double-kinks may stabilize at increased atomic distances, enabling a new double-kink to form on the already nucleated double-kink [24][5]. The jogs operate similarly to the kinks; instead of shifting inside the current glide plane, jogs will cause dislocation climb, meaning that the dislocation shifts from one glide plane to the next. Any dislocation will contain both kinks and jogs to a varying degree [39].

2.2.2 Lomer-Cottrell Locking

Cottrell proposed a model for the nucleation of cleavage cracks in BCC metals. The author presented a dislocation theory in which micro-cracks were formed by plastic deformation, but grew under tensile stress. This enabled an explanation of the transition temperature, radiation embrittlement, and other fracture effects [18]. Dislocation locking, often referred to as Lomer-Cottrell locking, occurs when two perfect dislocations encounter one another in a slip plane; splitting the dislocations into two Shockley partials. One of the partial dislocations becomes a leading dislocation, and the other a trailing dislocation. When two leading partial dislocations combine, they

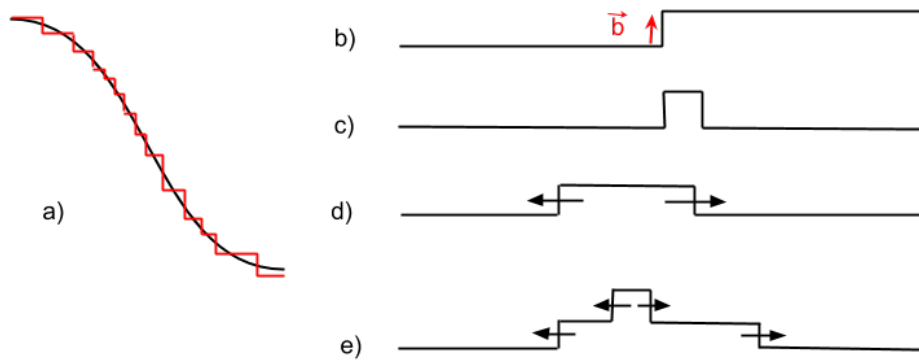


Figure 9: Schematic illustration of the kink dislocation mechanism; a) illustrates how curved dislocations exist of a number of kinks and jogs at the atomic level; b) a plain kink on a perfect screw dislocation; c) illustration of a simple double-kink; d) shows how double-kinks separate, helping the dislocation to propagate; e) illustrates how double-kinks may form on already nucleated double-kinks.

form a new dislocation which does not have its Burgers vector in the slip plane. The interaction is schematically simplified and illustrated in Figure 10, where two dislocations slipping on intersecting $\{101\}$ -planes interact to form the immobile Lomer-Cottrell dislocation. This dislocation has its Burgers vector normal to the cleavage plane and is known as the Lomer-Cottrell locking dislocation. The interaction promotes cleavage fracture, because it is accompanied by a reduction in dislocation energy [20]. This type of dislocation is immobile in the slip plane, acting as a barrier for other dislocations. The trailing dislocations pile up behind the locking dislocation, further increasing the amount of energy required to move the cluster of dislocations associated with the Lomer-Cottrell locking dislocation [17].

2.2.3 Dislocation Movement in Cantilevers

The modes of dislocation nucleation and behavior are described in Section 2.2.1. As the scope is shifted from general cases to constrained areas, e.g. cantilevers, the complexity of the mechanisms augments. The strength of a material increases with decreasing sample size [77]. The increase in yield strength is attributed to the presence of strain gradients within the field of deformation. One of the prominent theories of explaining the change in mechanical properties with down-sized samples is the strain gradient plasticity model. This theory integrates a strain gradient with the plastic strain. This strain gradient is compensated for by GNDs [68][27]. As the specimen volume is reduced, a higher density of GNDs is required to accommodate the deformation. If plane-strain conditions are assumed to fit the deformation of a cantilever, the one-directional strain will be given by the bending curvature in the plastically deformed region [68]. This will induce a small tilting of the

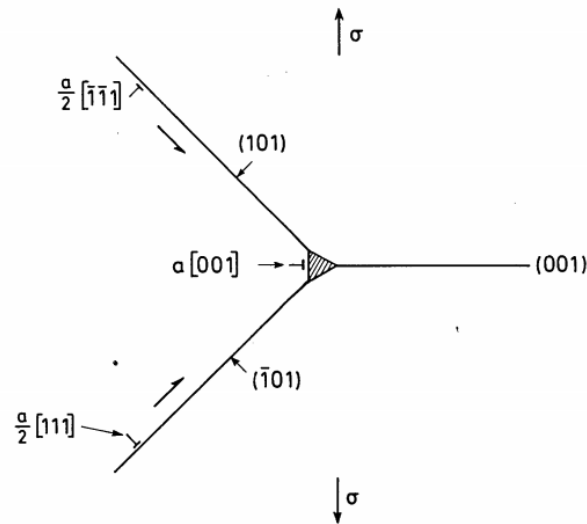


Figure 10: The Lomer-Cottrell model of cleavage crack nucleation in BCC metals. Adapted from [18].

deformed section of the cantilever. There is an optimal arrangement of the GNDs to accommodate the strain gradient, illustrated in Figure 11.

It is useful to note that the model illustrated in Figure 11 is simplified. It is likely that dislocation sources on several slip systems will be activated during deformation, leading to a complex arrangement of dislocations [68]. This may be visualized by choosing only the slip system with the maximum shear stress, which is aligned by an angle of 45° , and only one dislocation source per slip plane, illustrated in Figure 12. Under this condition, the generated dislocations will not be able to move freely; the GNDs will be affected by other dislocations and the distance to the cantilever surface. The generated GNDs will pile up around the dislocation source, and at the center of the cantilever. This will increase the necessary stress required to further deform the cantilever. If the cantilever volume is reduced, the possibility of finding a dislocation source in the deformed volume will decrease, and the average length between the source and the cantilever center will consequently also decrease. This will again increase the dislocation pile-up and the flow stress [68].

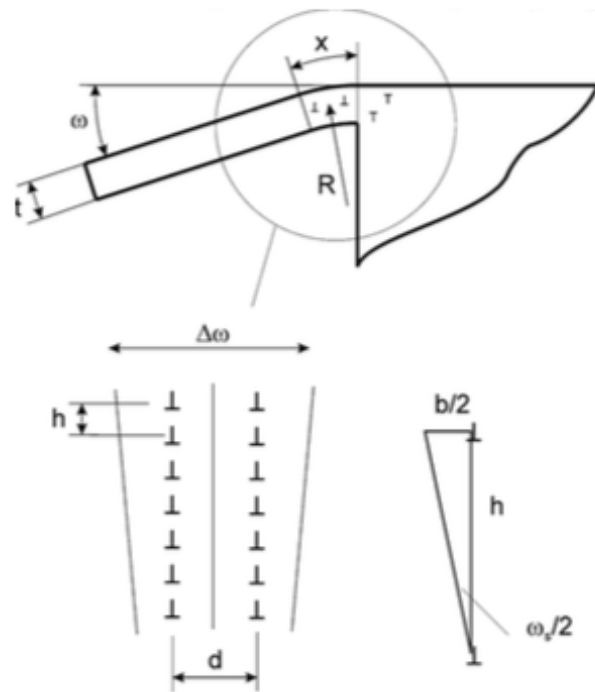


Figure 11: Schematic illustration of the optimal distribution of GNDs in a cantilever, in order to accommodate the strain gradient. Adapted from [68].

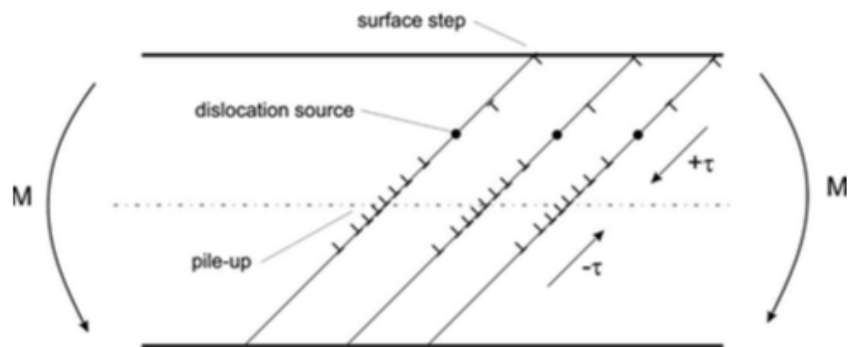


Figure 12: Schematic illustration of a deformed cantilever, with activated dislocation sources. Adapted from [68].

2.3 Fracture Mechanisms

There are three main types of fracture mechanisms in metals: ductile, cleavage and intergranular fracture. Ductile materials fail by nucleation and coalescence of voids in the matrix or at inclusions and second-phase particles. Cleavage fracture, often referred to as brittle or transgranular fracture, propagates by separation along specific crystallographic planes. Intergranular fracture propagates along grain boundaries. This section will elaborate on the fracture mechanisms of metals, with an emphasis on cleavage fracture.

2.3.1 Ductile Fracture

A ductile fracture is characterized by extreme plastic strains related to a reduction in the material cross section area. The work hardening of the material will match the strains as the stress builds up, but eventually the strain hardening will fall behind, and unstable deformation begins, called necking. This will happen as the maximum load is achieved. The purity of the ductile material strongly influences ductile fracture behavior. Pure metals will show sharp necking points, and exercise extreme local strains with an almost 100% reduction in cross sectional area. Materials containing impurities will collapse at much lower strains [3, p.219]. The necking phenomenon is illustrated in Figure 13. This is due to nucleation of microvoids at impurities, which spread and lead to material failure. When describing ductile fracture, the word 'crack' is avoided. Ductile materials rupture, and are 'pulled apart', leaving a rough surface.

A ductile fracture is separated into different sections describing the different active mechanisms during the fracture. First, voids form in the matrix, or at impurities. This can occur either by decohesion or by shearing of a particle. Secondly, voids grow due to plastic strains and stresses. Finally, voids will coalesce with adjacent voids, forming a fracture surface. As more voids merge, the merging rate increases, and material failure is imminent. The stepwise process of ductile fracture is illustrated in Figure 14 [3, p.219].

2.3.2 Cleavage Fracture

Cleavage fracture is characterized by rapid and unstable crack propagation in absence of significant plastic deformation. A material may only fail by cleavage if there is a sufficiently large local discontinuity at the crack front, able to break the atomic bonds. This leaves a sharp and blocky fracture surface with river markings merging in the direction of the crack growth, emanating from the point of initiation. These river markings are typically formed when the crack is re-initiating at the boundary of a new grain with a different crystallographic orientation. Expansion of a cleavage crack prefers the atomic planes with the lowest atomic packing factor, i.e., planes with low Miller indices, often referred to as cleavage planes. These planes require the breaking of fewer atomic

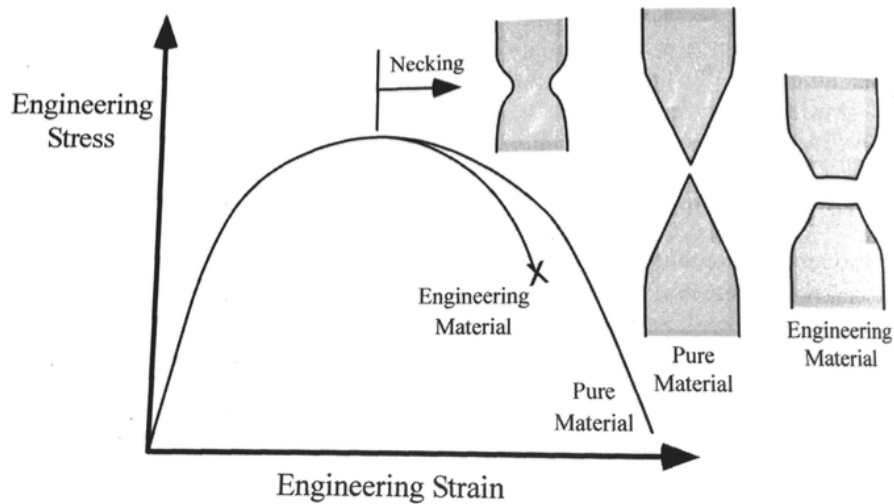


Figure 13: Illustration of necking for pure metals and engineering materials, e.g. alloys. Adapted from [3, p.220].

bonds than denser planes. For the ferritic steel investigated in this thesis, cleavage should occur in $\{100\}$ planes [3, p.234][11, p.235].

Cleavage fracture typically occurs when plastic flow is restricted. FCC crystal structures are typically not susceptible to cleavage fracture due to a high number of active slip systems; BCC and HCP have a limited number of active slip planes, and are therefore susceptible to cleavage. At lowered temperatures these structures will fail by cleavage [3, p.234]. This is due to a temperature dependant transition from a ductile to brittle fracture mode, described in Section 2.3.5.

2.3.3 Cleavage Fracture Initiation

There are several key factors influencing the onset of brittle fracture in BCC materials:

1. Grain size.
2. Development of sharp yield points.
3. Temperature dependence of the yield stress.
4. Nucleation of cracks at particles.
5. Nucleation of cracks at twins.

1. Grain size is an especially important factor influencing the DBTT. As the grain size is reduced the transition temperature decreases. A reduced grain size also increases the yield strength and ductility simultaneously. N.J. Petch showed that the transition temperature related linearly to

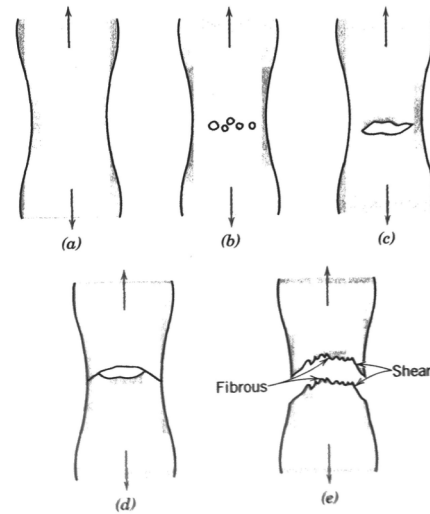


Figure 14: Stepwise illustration of ductile fracture from the initiation of necking (a), to cup-cone fracture (e). Adapted from [13].

$\ln \frac{1}{\sqrt{d}}$ [73]. This relationship can be derived from a dislocation model concerning crack initiation at dislocation pile-ups near grain boundaries. Conceptually, smaller grain size leads to fewer dislocations piling up at grain boundaries, which ultimately reduce the local stress concentration. This results in the Hall-Petch equation, Equation 2, where τ_y is the yield shear strength, τ_i is the friction stress, k_y is the dislocation pile-up constant and d is the average grain size [3, p.238]:

$$\tau_y = \tau_i + k_y \frac{1}{\sqrt{d}} \quad (2)$$

2. Interstitial atoms tend to cause steels to exhibit sharp yield points. There are two dislocation motion theories that describe conditions suitable for rapid localized dislocation movement as a result of high stresses favoring crack nucleation. The Cottrell-Bilby theory describes a catastrophic release of dislocations. It states that the temperature dependence of the yield point is explained by thermal fluctuations enabling dislocations to break away, helping other dislocations to do the same [19]. The Gilman-Johnston theory describes rapid movement of generated dislocations. This theory states that the yield stress is not dependant on existing dislocations, but instead determined by the material's resistance to dislocation glide of newly generated dislocations [48].

3. BCC metals show clear yield stress temperature dependence, even when the concentration of interstitial impurities is low, i.e., the Peierls-Nabarro force is temperature dependant. The Peierls-Nabarro force is presented in Section 2.3.4. The velocity of a propagating dislocation is proportional to the yield stress. With decreasing temperature, initial dislocation propagations travel

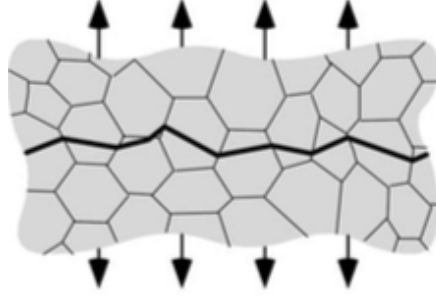


Figure 15: Illustration of cleavage crack propagation. Adapted from [3, p.236].

with increased velocity, increasing the probability of forming a crack nucleus through coalescence of dislocations [20][11, p.237-238].

4. Second-phase particles serve as suitable nucleation sites for cracks. These particles can crack during high stresses, or plastic strain in the surrounding matrix, creating a micro-crack. These micro-cracks, called Griffith-cracks, may, if the stresses ahead of the micro-cracks are sufficient, propagate through the material resulting in catastrophic cleavage fracture. The presence and concentration of brittle particles play a major role in the fracture characteristics of steel. Inclusions, if brittle, may also induce micro-cracks [11, p.238-239]. If a given particle is round and produce a penny-shaped micro-crack, the fracture stress, σ_f , will be given by the following equation:

$$\sigma_f = \sqrt{\frac{\pi E \gamma_p}{(1 - \nu^2) C_0}} \quad (3)$$

where γ_p is the required plastic work in order to create the fracture surface, C_0 is the particle diameter, ν is the Poisson's ratio, and E is the Young's modulus of elasticity. In fine grained steels, the critical event may be propagation across the first encountered grain boundary. Equation 3 then changes to Equation 4, which was originally proposed by Griffith.

$$\sigma_f = \sqrt{\frac{\pi E \gamma_p}{(1 - \nu^2) d}} \quad (4)$$

where d is the average grain size. Martensitic and bainitic microstructures will further alter the equation, introducing packet diameter as the decisive parameter [3].

5. Twins are a major contributor to the nucleation of cracks at lower temperatures. When the temperature is decreased to a point where the the critical stress for twinning deformation is reached, deformation by twinning may become significant. Different twin-formations tend to nucleate cracks, e.g. when two twins intersect, or at points where twins are in contact with grain

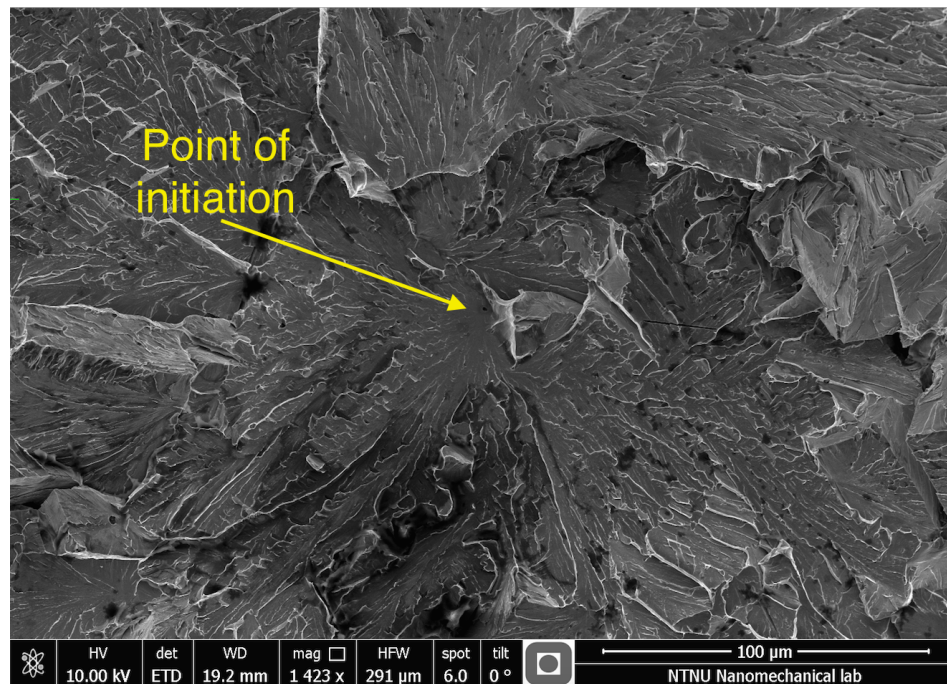


Figure 16: SEM picture of a cleavage fracture surface. The local initiation point is marked by the yellow arrow.

boundaries. As temperature is lowered, the plastic deformation at the tip of a moving crack is impeded, thus aiding further propagation of cracks [11, p.238].

2.3.4 Peierls Stress and Peierls-Nabarro Force

The Peierls stress and Peierls-Nabarro force both refer to dislocation movement in crystal lattices. These highly related theories, which describe nuances of the same phenomenon, are both important to consider to fully understand a material's resistance to dislocation movement. The plastic flow of metals is controlled by a $\frac{a}{2} < 111 >$ screw dislocation. Dislocation movement induces friction stresses in the crystal lattice, called Peierls stress. Nature always minimizes the energy required for operations, such as the plastic flow of metals. It is therefore reasonable to assume that initially slipped planes will grow at the expense of unslipped planes. The dislocation's width affects the required stress for dislocation movement. Wide dislocations reduce the elastic energy in the crystal lattice, and these dislocations reduce the interface energy between the dislocation and atoms. The Peierls stress takes the width of the dislocation into account when calculating the stress necessary to achieve dislocation movement, thus quantifying the dislocation mobility [23][52][82]. The Peierls

2 THEORETICAL BACKGROUND

stress for a given material is the stress required to move a dislocation through the crystal lattice in a given direction. The mathematical expression for the Peierls stress, τ_p , is presented in the following equation:

$$\tau_p \approx \frac{2 \cdot G}{1 - \nu} \cdot \exp\left(\frac{-2 \cdot \pi \cdot w_{disl.}}{b_v}\right) \approx \frac{2 \cdot G}{1 - \nu} \cdot \exp\left(\frac{-2 \cdot \pi \cdot a_{planes}}{(1 - \nu)b_v}\right) \quad (5)$$

where a_{planes} is the distance between slip planes, $w_{disl.}$ is the dislocation width, G is the shear module, b_v is the Burgers vector, and ν is the Poisson's ratio [23].

The expression given in Equation 5, is derived from a sinusoidal force related to the positioning and distance of a given dislocation. The energy barrier, i.e., the Peierls energy barrier, is recognized as the force threshold that must be exceeded in order to achieve plastic deformation. This barrier is strongly dependant on the atomic density. As the interatomic distance increases, the force threshold will decrease [23]; thus explaining why slip occurs in the closest packed atomic planes. Due to the periodic magnitude of the barrier, this factor will be important as the temperature is lowered. The periodic change of the energy barrier will cause the dislocations to propagate by kinks [12][31]. The periodic variation of the Peierls barrier is illustrated in Figure 17; the atoms in the figure represent the last atoms in the inserted half planes for edge dislocations.

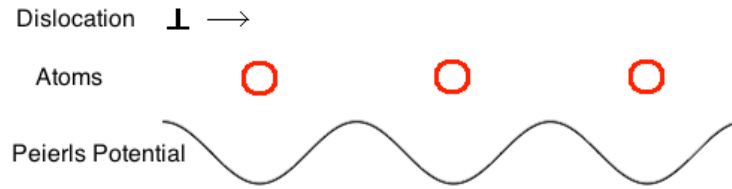


Figure 17: Schematic illustration of the periodic variation of the Peierls potential between atoms, during dislocation movement. Adapted from [87].

All strengthening factors affecting the yield stress accumulate in the general, additive, equation. The Peierls stress will contribute to this equation, expressed in the following equation:

$$\sigma_y = \frac{\tau_p}{m} + \sigma_0 \quad (6)$$

where σ_y is the accumulated yield stress, σ_0 is the yield stress due to all other strengthening factors, m is the Schmid factor, and τ_p is the Peierls stress [33]. However, the Peierls-Nabarro force, or Peierls stress, is not completely accurate. This is because it does not take into account that the dislocations are experiencing stress-induced narrowing [62].

2.3.5 Ductile to Brittle Transition Temperature

The DBTT is the temperature a material changes mode of characteristic failure. As the temperature is lowered, a material that previously failed by ductile fracture will change to a brittle fracture. This transition is rapid and indicates a material's susceptibility to cleavage fracture in service. The DBTT is illustrated in Figure 18 [73][3]. BCC structures exercise a rapid transition, illustrated in

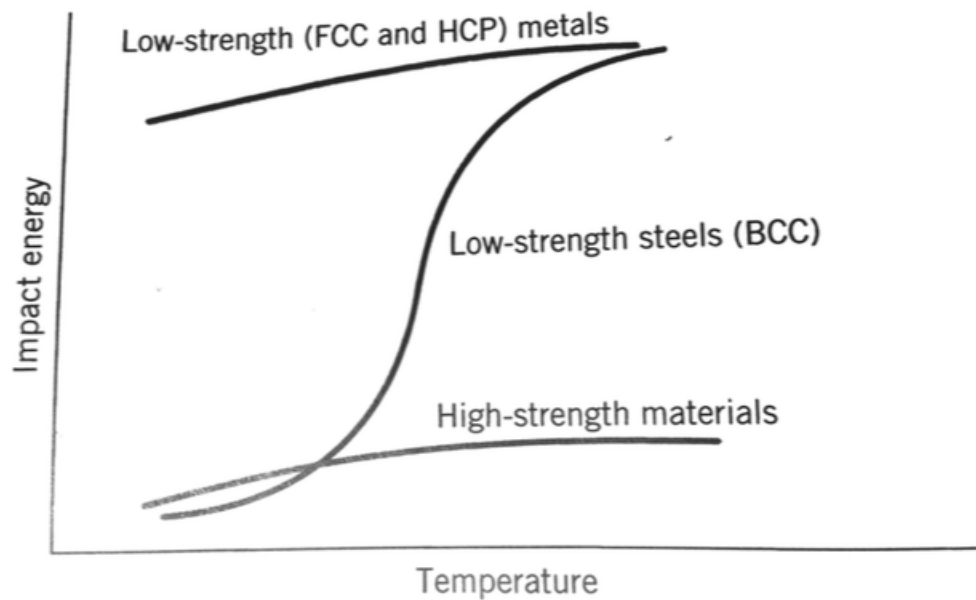


Figure 18: Illustration of how the absorbed impact energy changes with temperature, for different materials. Adapted from [13].

Figure 18, due to a reduced number of available slip systems as the temperature is lowered. FCC and HCP structures have a much higher number of available slip systems, and are not as dependent on temperature. A material subject to stresses, while having only a limited number of slip systems available, will experience an energy build-up. The energy is typically released in a fatal collapse of the material.

Full understanding of the DBTT, requires a defined transition criterion. The change in fracture mode from ductile to brittle occurs over a temperature range that is closely interconnected with the change in deformation energy. Inside this temperature range, the metal exhibits fracture characteristics from both modes. There will be some ductile fracture near the notch, which changes to cleavage as the crack propagates. This is due to an increase of the triaxiality of the stress as the propagation speed increases [73]. This implies that the fracture will switch from ductile to brittle when the stress ahead of the fracture tip becomes capable of Griffith propagation. From this, N.J.

Petch derived the following ductile-brittle transition fracture criterion:

$$\sigma_0 \simeq \frac{\frac{4qG\gamma'}{k^*} - k^*}{\sqrt{d}} \quad (7)$$

where σ_0 is the friction stress, q is a factor, G is the shear modulus, γ' is the effective surface energy, k is a constant, and d is the grain diameter [73].

The temperature dependence of the ductile-brittle transition criterion, Equation 7, is introduced through γ' and σ_0 . An increase in temperature will decrease σ_0 and increase γ' . γ' is increased due to a weakening of dislocation locking. Experimental work has shown that σ_0 has a larger impact on the temperature dependence than γ' , and that the temperature dependent part of σ_0 represents a significant Peierls-Nabarro stress [73]. The temperature variation of the Peierls-Nabarro stress is explained by an increase in dislocation width as the temperature increases.

2.3.6 Smith's Model

Smith proposed a theoretical model of cleavage crack nucleation and propagation. The crack mechanism that this model is based on is illustrated in Figure 19. Dislocation pile-up causes a grain boundary particle to crack as a Griffith defect. Dislocation pile-up and coalescence, explained in Sections 2.2.1 and 2.2.2, along with the grain boundary diameter, have a strong influence on this cleavage model [20]. Smith proposed that the distribution of dislocations, both inside and outside the crack, is determined by the true operative stress, and that all dislocations satisfy equilibrium energy conditions [84]. The model implies that the nucleated crack is affected by the applied stress, but the dislocations propagating from a source are affected by an effective shear stress. It is also assumed that dislocations of both signs are emitted from the dislocation source, and that crack nucleation is possible at both ends of the activated slip band [85]. By examining the energy change with increasing crack length, the cleavage fracture stress may be calculated by:

$$\left(\frac{C_{0,b}}{d_b}\right)\sigma_f^2 + \tau_{eff}^2 \left[1 + \frac{4}{\pi} \sqrt{\frac{C_{0,b}}{d_b} \frac{\tau_i}{\tau_e}}\right]^2 \geq \frac{4E\gamma_p}{\pi(1-\nu^2)d_b} \quad (8)$$

where $C_{0,b}$ is the thickness of the grain boundary particle, d_b is the distance from the dislocation coalescence to the grain boundary, σ_f is the cleavage fracture stress, τ_{eff} is the effective shear stress, τ_i is the lattice friction shear stress, E is Young's modulus of elasticity, γ_p is the effective surface energy, and ν is the Poisson's ratio [20].

2.3.7 Beremin Model

The Beremin model is an important statistical local fracture criterion. It is based on the elastic-plastic stress-strain history at the origin of the fracture. This is done by utilizing a micromechanical

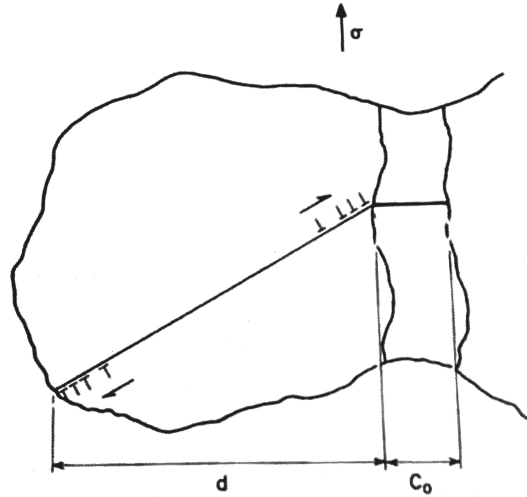


Figure 19: Schematic illustration of Smith's model of cleavage fracture, where σ is the applied stress, $C_{0,b}$ is the diameter of the grain boundary carbide, and d_b is the distance from the dislocation coalescence to the source [85]. Adapted from [86].

cleavage model [9][14][10]. The model is ultimately based on the assumption that the first element to fracture will cause volume fracture, meaning that the initiation of the first fracture surface will cause catastrophic failure.

Cracks proliferate inside grains due to plastic deformation of the material. This may induce shearing of carbide particles located at the grain boundaries. As the stress reaches a critical value, σ_c , these micro-cracks will propagate. The critical stress is expressed by the following equation:

$$\sigma_c = \sqrt{\frac{2E\gamma}{\pi(1-\nu^2)l_0}} \quad (9)$$

where E is Young's modulus of elasticity, γ is the surface energy of the crack, ν is the Poisson's ratio, and l_0 is the cracks initial length [9]. This equation is not sufficient by itself since scatter and volume fraction are also necessary to recognize. By invoking the Griffith criterion, and assuming that size distribution and scatter of micro-cracks follow a power law, a probability function describing the assumed scatter of cracks inside a grain may be utilized [14]. This probability function may be further tailored to accommodate the probability of finding a micro-crack of the critical length, i.e., probability of fracture in a given volume at a certain stress. This results in the probability function, P_f , where l_0^c is the critical crack length, and $P(l_0)$ is given by $\alpha l_0^{-\beta}$, where α and β are

material constants:

$$P_f = \int_{l_0^c}^{\infty} P(l_0) dl_0 \quad (10)$$

This model is comprehensive and extensive, requiring a strong data collection and extensive computation. However, since this model accommodates several key elements of cleavage fracture, the accuracy and reliability of this model mirrors its complexity. Beremin demonstrated the model's flexibility, while still achieving successful predictions, proving the model an exceptional tool when facing problems outside the linear elastic domain [9]. One of the main advantages of the Beremin model is the ability to transfer calculated fracture data between different structures, quantifying the relationship between micro and macro [14]. Another important ability of the Beremin model is the capability to predict the transition temperature from ductile to brittle fracture [10].

2.3.8 Multiple Barrier Model

Lambert-Perlade et. al. developed a MBM for cleavage fracture [55]. In order to achieve cleavage fracture in a material, several barriers, or steps, must be breached. As presented in Sections 2.1 and 2.3.3, welding of HSLA steels produce a weakened zone with reduced fracture toughness. The HAZ will contain a different, non-favorable microstructure with brittle second-phase particles. Cleavage fracture in HSLA steels will therefore intermittently occur by dynamic propagation of micro-cracks nucleated by deformation cracking of these brittle second-phase particles. In order to achieve cleavage of a material, three key barriers must be overcome, illustrated in Figure 20, [55]:

1. Nucleation of a micro-crack by shearing at, or near, a second-phase particle or MA constituent.
2. Crack propagation across the particle-matrix interface and into the matrix.
3. Propagation of the nucleated crack across a grain boundary, into neighbouring grains, inducing material failure.

This model may be recognized as a refined expansion of the Smith model, with focus on crack propagation instead of dislocation propagation and coalescence, presented in Section 2.3.6. The models are linked when considering stress concentration and build-up, inside a grain. The MBM integrates the weakest-link assumption to determine the fracture probability of the material, which is given by the combined probabilities of all three events occurring in the same location of the microstructure [55]. An example of a probability function used for this purpose is given in Equation 10. Lambert-Perlade applied three different weakest-link models to account for the DBTT's influence on the fracture toughness. The DBTT is covered in Section 2.3.5. The Beremin model is one of the three applied weakest-link models, described in Section 2.3.7. Weakest-link models assume that the first element to fracture will induce critical failure of the material.

To determine what stresses are required in order to breach the three main barriers, it is necessary to define the relevant stress variables [55]:

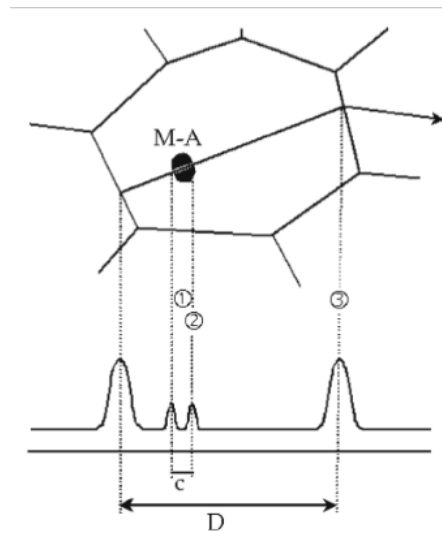


Figure 20: Schematic illustration of nucleation of a cleavage micro-crack from a second-phase particle. Adapted from [29].

- The stress in a MA constituent or second-phase particle σ_{MA} , of the critical value σ_{MA}^c .
- The local maximum stress σ_I .
- The strength of a high-angle bainite boundary σ_{mm} .
- The strength of the particle-matrix interface σ_{pm} .

σ_{mm} is assumed to be temperature dependant, increasing with increasing temperature. σ_{pm} will be lower than σ_{mm} at elevated temperatures.

Figure 21 describes the stress requirements necessary in order to overcome each barrier, resulting in cleavage fracture. The effect of temperature on the failure mechanism can be described, when sectioned into four intervals, in the following way [55]:

1. At very low temperatures, $T < -170^\circ\text{C} \Rightarrow \sigma_{mm} < \sigma_{pm} < \sigma_y$. This means that the first crack nucleation ($\sigma_{MA} \geq \sigma_{MA}^c$) will cause material failure if $\sigma_I \geq \sigma_y$. Ultimately, this implies that failure is nucleation controlled at low temperatures.
2. At slightly higher temperatures, $-170^\circ\text{C} < T < -60^\circ\text{C} \Rightarrow \sigma_{mm} < \sigma_y < \sigma_{pm}$. As σ_I increases upon loading, such that $\sigma_y < \sigma_I < \sigma_{pm}$, the result is nucleation of micro-cracks that arrest temporarily at the particle-matrix interface (if $\sigma_{MA} \geq \sigma_{MA}^c$). Once σ_I exceeds σ_{pm} , the crack will propagate into the bainitic matrix. At this stage, the σ_I will be high enough to induce material failure. This implies that the strength of the particle-matrix interface, σ_{pm} , governs failure.
3. As the temperature is heightened, $-60^\circ\text{C} < T \lesssim -20^\circ\text{C}$, the boundary strength will increase, leading to $\sigma_y < \sigma_{pm} < \sigma_{mm}$. As σ_I increases, until $\sigma_{MA} \geq \sigma_{MA}^c$, a nucleated crack will

propagate through the matrix, but arrest at the matrix-matrix interface. The crack will arrest at the boundary until $\sigma_I > \sigma_{mm}$, when the crack may propagate through grains, inducing material failure. Thus, the failure is controlled by the strength of the matrix-matrix interface, i.e., high-angle bainite packet boundaries.

4. At higher temperatures, $T \gtrsim -20^\circ\text{C}$, σ_{mm} is significant, and ductile fracture occurs prior to cleavage fracture. The ductile fracture may be initiated at second-phase or MA particles.

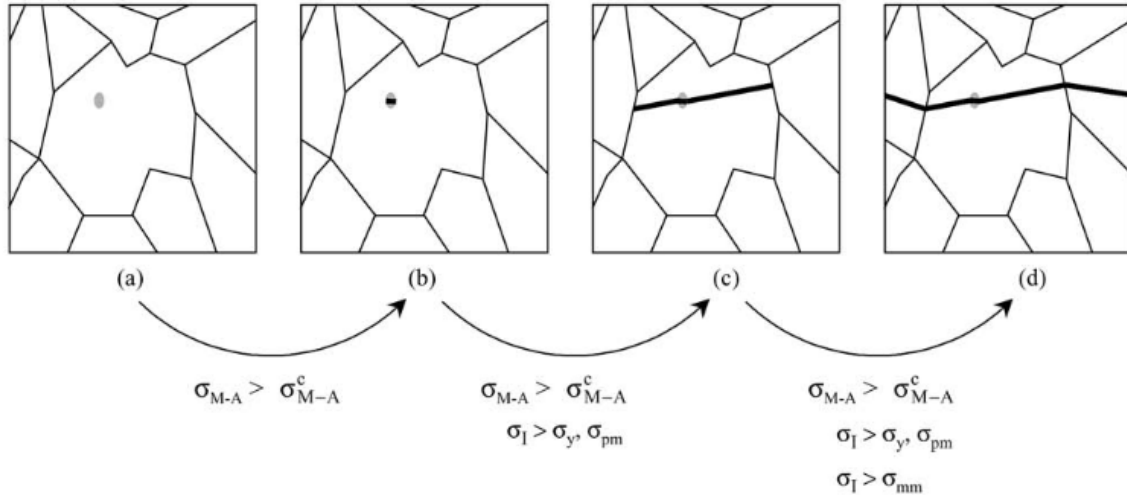


Figure 21: Schematic illustration of the role and stress requirements of microstructural barriers on failure mechanisms. Adapted from [55].

Utilization of the MBM requires reliable data of the mechanical properties of the material, and quantitative information on the local stress requirements necessary to propagate cracks. The material’s ability to arrest micro-cracks will also affect the accuracy of the model. Nanomechanical testing methods should be suitable, but experience and a strong theoretical understanding is required.

2.4 Linear Elastic Fracture Mechanics Approach

LEFM lays the foundation for measuring fracture toughness. However, when testing samples in the order of micrometers, instead of millimeters, the fracture behavior may alter. Fracture experiments are based on the plastic deformation in front of the crack tip. This plastic zone spreads out a certain length scale. When the plastic zone becomes significant relative to the specimen size, which in this case is a minuscule cantilever, it may affect the fracture behavior of the specimen. Small scale yielding is a prerequisite for the application of LEFM. The size of the plastic zone, ω , must be

significantly smaller than the length of the crack and sample dimensions in order to apply LEFM. ω , has the following relationship [95]:

$$\omega \propto \frac{K_{IC}^2}{\sigma_y^2}$$

where σ_y is the yield stress, and K_{IC} is the critical stress intensity factor of the material for fracture mode I. Both of these material properties are temperature dependent. General theory related to the plastic zone is covered in K. Greina's master thesis, from 2014 [29]. It is natural to mention that the transition from small scale yielding to full scale yielding may occur for macro-sized samples as well. This occurs when the fracture toughness is significant, or the yield strength is low. The ASTM E399 standard for measuring fracture toughness values sets the lower limit of the crack length and sample thickness to $2.5 \frac{K_{IC}^2}{\sigma_y^2}$ [95]. In other words, for LEFM to be applicable, one needs a relatively large yield strength and low fracture toughness, which is typical for brittle materials. Wurster et al. [95][96] conducted experiments on micro-sized cantilevers of single crystalline tungsten. This was done in order to explore the fracture mechanics of BCC metals in the brittle regime. The authors concluded that LEFM does not deliver correct fracture toughness values, rather only a lower bound for critical stress intensities. However, the values of the preliminary stress intensity, K_Q , deliver good approximations for the first deviation of the curves from ideal elastic behavior indicating a massive emission of dislocations, and pronounced plastic deformation [95]. Generally, HSLA steels have a higher yield strength than pure tungsten, and also several orders of magnitude larger fracture toughness [15][99][95]. This does not bode well for the applicability of LEFM, but the same approach as Wurster et al. may yield approximations for the first deviation from the ideal elastic behavior [95].

Micro-fracture experiments with cantilevers can be useful, as they allow testing of single microstructural constituents, e.g. grain boundaries [6][7]. This feature will be used in this work to investigate the micromechanical properties of CGHAZ and ICCGAZ. Based on the work by Wurster et al. and the ASTM standard, the conditional critical stress intensity factor, K_Q , is derived [95][45]:

$$K_Q = \frac{F_Q L}{w b^{\frac{3}{2}}} \cdot f\left(\frac{a}{b}\right) \quad (11)$$

where F_Q is the determining force, according to ASTM E-399 [45], L the bending length, a the crack depth, b the thickness of the specimen, and w the width of the specimen. $f\left(\frac{a}{b}\right)$ is a shape factor dependent on the cantilever geometry, and the input is the crack depth and the specimen thickness.

The actual minimum limit for sample size according to ASTM would be about 230 μm [45]. The cantilevers are about two orders of magnitude smaller than this requirement. However, LEFM is sufficient for the determination of mechanical properties for small components, as it results in a complete description of the reaction of a specimen to a load [95]. In macroscopic samples, fracture

toughness has been successfully determined during large-scale yielding using different methods like the J-integral, crack tip opening displacement (CTOD), or crack tip opening angle (CTOA).

2.4.1 Determination of Crack Growth

When investigating the fracture toughness of a specimen, it is necessary to obtain information about the crack growth. Usually, this can be measured directly, but this becomes difficult in practice when specimen dimensions are only a couple of micrometers. Ideally, it would be possible to measure the displacement at the crack mouth using the SEM while conducting the experiments, but experience from earlier work yields this method difficult in practice [53][87]. In order to obtain information about the crack growth, the unloading stiffness method is utilized [95][70]. The support on the fixed end of the cantilever is approximated to be infinitely stiff and indentation of the cantilever is neglected as test indents yielded depths of < 50 nm.

Several unloading steps has to be made to determine the crack growth for each specimen. The stiffness of the cantilever decreases when the crack grows. With reference to Figure 27, the ligament length $(b - a_i)$ in the i -th step of unloading can be calculated based on the deflection of the cantilever [95]:

$$(b - a_i) = \sqrt[3]{\frac{4kL^3}{wE}} \quad (12)$$

where k is the unloading stiffness from the load-displacement diagrams, E is the Young's modulus of elasticity, L the bending length, and b the sample thickness. The small distance from the notch to the cantilever's base is not taken into account.

Equation 12 is valid for a fixed cantilever [95]. This equation can also be used the other way around to determine the Young's modulus by inserting the notch depth determined in the SEM. Equation 12 is a rough assumption, but Wurster et al. used this to obtain results in agreement with observations [95].

2.4.2 Cantilevers with a Pentagonal Cross Section

Pentagonal cantilevers have been increasingly popular in recent years for nanomechanical purposes, since a FIB allows for a relatively easy method to produce cantilevers of satisfactory quality. However, there is no consensus for the method of taking into account the geometry of the cantilever; the standards are made for cantilevers with square cross sections. Wurster et al. used a shape factor designed for a square cantilever [95], but pentagonal cantilevers will be used in this work. In the literature, there are numerous variants of the shape factor used to calculate the preliminary stress intensity factor, K_Q , [64][97][69][90][95]. The symbols describing the dimensions of a pentagonal cantilever are displayed in Figure 22.

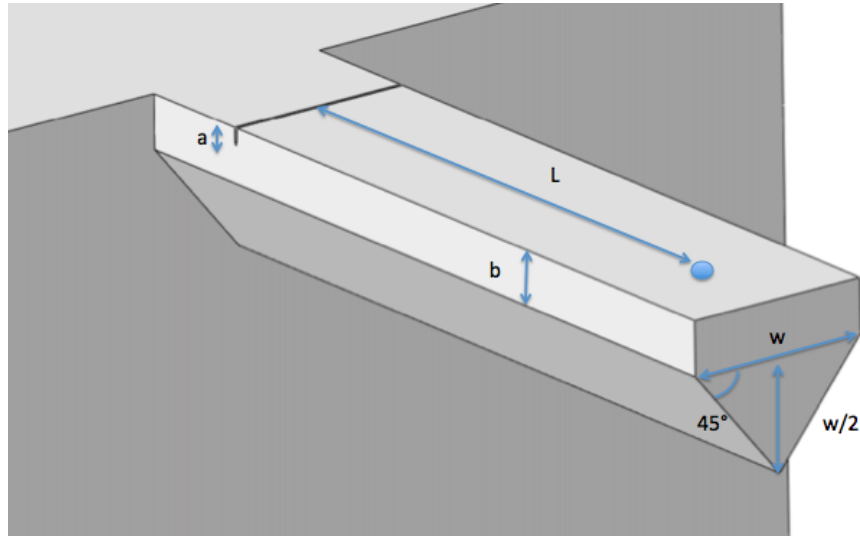


Figure 22: Schematic illustration of the symbols for the cantilever dimensions.

Three papers with extensive work on pentagonal cantilevers are the basis for this section. The authors of the papers are: Di Maio and Roberts (2005) [64], Zhao et al. (2008) [97], and Armstrong et al. (2011) [6]. The work done by Zhao et al. is based on Murakami [69], and is almost identical to Srawley and Gross's [90] solution from 1975, which is not for pentagonal cross sections. The author does not elaborate on this problem. The paper by Armstrong et al. refers to the geometry factor used by Di Maio and Roberts, but the factor presented in the paper is not the same. This is illustrated in Figure 23. This figure may indicate that Di Maio and Roberts are the only authors taking the pentagonal shape into consideration; their shape factor is less affected by the a/b -ratio, which makes sense considering a constant triangle cross section at the bottom not being a part of the ratio. Two different approaches to the calculation of K_Q for pentagonal cantilevers will be presented and used in the analysis.

The first approach is to use Equation 11, which was used by Wurster et al. for cantilevers with a square cross section. In order to take the pentagonal shape into account, a new thickness of the cantilever will be defined [95]. With reference to Figure 22, the new thickness, denoted b^* , is defined as:

$$b^* = \frac{A_{pent-crssec}}{w} = b + \frac{w}{4} \quad (13)$$

which will then be the input for the shape factor for square cantilevers used by Wurster et al. This simplification is based on the assumption that the fracture toughness is predominantly affected by

the area of the cross section, rather than the geometry. The shape factor is:

$$f\left(\frac{a}{b}\right) = 4 \cdot 3 \cdot \sqrt{\left(\frac{a}{b}\right)} \cdot \frac{1.23 - \left(\frac{a}{b}\right) \left[1 - \left(\frac{a}{b}\right)\right] \cdot \left[-6.09 + 13.96\left(\frac{a}{b}\right) - 14.05\left(\frac{a}{b}\right)^2\right]}{2\left(1 + 2\left(\frac{a}{b}\right)\right) \cdot \left(1 - \left(\frac{a}{b}\right)\right)^{1.5}} \quad (14)$$

The second approach is the method used by Di Maio and Roberts. Instead of Equation 11, the equation for the critical stress intensity for mode I fracture can be expressed as:

$$K_{Q,DiMaio} = \sigma_c \sqrt{\pi a} \cdot f\left(\frac{a}{b}\right) \quad (15)$$

where σ_c is the fracture stress, a is the crack length, and $f\left(\frac{a}{b}\right)$ is a dimensionless shape factor dependent on sample geometry. In order to obtain σ_c it was assumed that only small deformations occur, hence σ can be calculated as [64]:

$$\sigma = \frac{FLy}{I} \quad (16)$$

where F is the applied bending force from the indenter, L is the bending length, I is the moment of inertia of the beam cross section, and y is the vertical distance between the upper surface and the neutral plane. For a pentagonal beam, as illustrated in Figure 22, I and y can be calculated respectively [64]:

$$I = \frac{wb^3}{12} + bw \cdot \left(y - \frac{b}{2}\right)^2 + \frac{w^4}{288} + \frac{w^2}{4} \cdot \left(\frac{b}{6} + b - y\right)^2 \quad (17)$$

$$y = \frac{\frac{b^2w}{2} + \frac{w^2}{4} \left(b + \frac{w}{6}\right)}{bw + \frac{w^2}{4}} \quad (18)$$

The shape factor was estimated by calculating the relation between applied load and specimen/crack geometry. The result was [64]:

$$f\left(\frac{a}{b}\right) = 1.85 - 3.38\left(\frac{a}{b}\right) + 13.24\left(\frac{a}{b}\right)^2 - 23.26\left(\frac{a}{b}\right)^3 + 16.8\left(\frac{a}{b}\right)^4 \quad (19)$$

2.5 Elastic-Plastic Fracture Mechanics Approach

A number of fracture criteria, which remain applicable even in the presence of large scale plasticity, have been developed. This enables a reduction in size of test specimen, compared to those required for linear elastic fracture mechanics testing. The most successful among these criteria has been the CTOD. The J-integral is also applied, because it is easily measured and a well-known and accepted criterion [76].

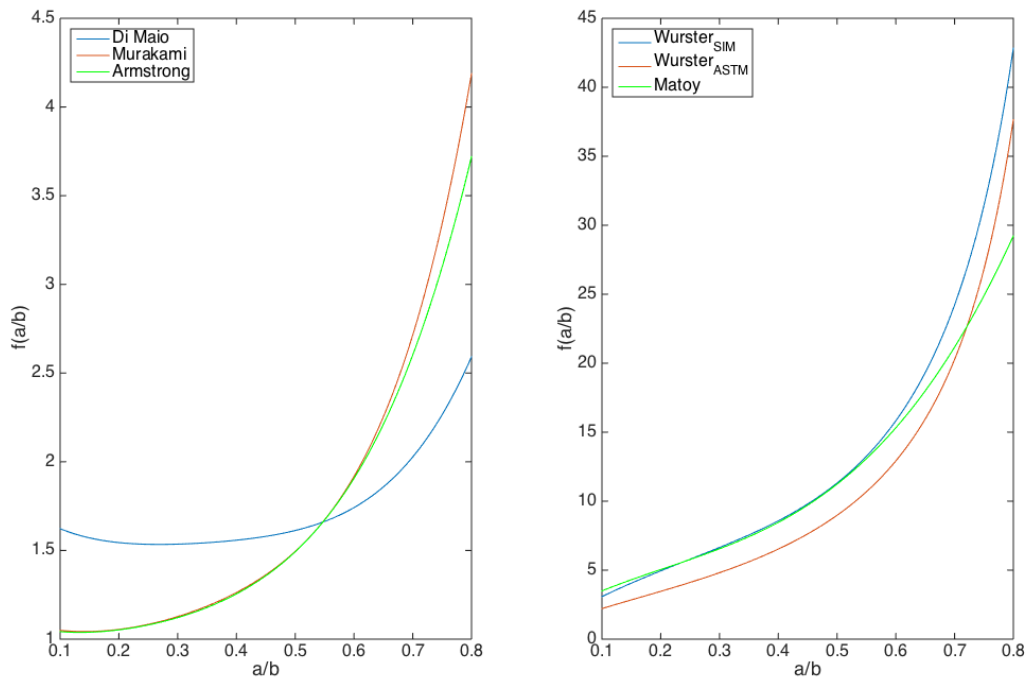


Figure 23: Comparison of the geometry factors presented in different papers, labeled by main author. Left and right plots are for shape factors in Equations 11 and 15, respectively.

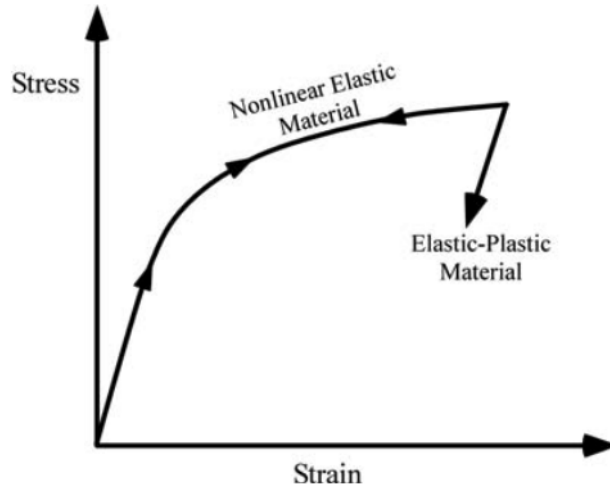


Figure 24: Schematic comparison of the uniaxial stress-strain behavior of elastic-plastic and non-linear elastic materials. Adapted from [3].

2.5.1 J-Integral

The J-integral has been a successful tool to characterize fracture for non-linear materials. Rice idealized the elastic-plastic deformation as non-linear elastic, and thereby extended the basis for fracture mechanics well beyond the validity of LEFM [74]. The difference between elastic-plastic and non-linear elastic materials is illustrated in Figure 24. The difference in unloading behavior makes it harder to analyze materials that exhibit irreversible plasticity. Rice applied deformation plasticity, i.e., non-linear elasticity, to the analysis of a crack in a non-linear material. He showed that the non-linear energy release rate, J , could be written as a path independent line integral [74]. Hutchinson [41] and Rice and Rosengren [75] also showed that J uniquely characterizes crack-tip stresses and strains in non-linear materials. This indicates that the J-integral can be considered both an energy parameter per unit fracture surface area, and a stress intensity parameter [3, p.107].

The energy release rate interpretation is the most convenient way to understand the J-integral. Irwin [46] defined an energy release rate, \mathcal{G} , which is a measure of the energy available for an increment of crack extension:

$$\mathcal{G} = -\frac{d\Pi}{dA} \quad (20)$$

where Π is the potential energy and A is the crack area. This relation describes the rate of change of potential energy relative to the crack area. Since \mathcal{G} is the derivative of a potential, it is also called the crack extension force, or the crack driving force. The same definition holds for non-linear

elastic materials, except that \mathcal{G} is replaced by J [3]:

$$J = -\frac{d\Pi}{dA} \quad (21)$$

The potential energy, Π , is given by:

$$\Pi = U - F \quad (22)$$

where U is the strain energy stored in the body, and F is the work done by external forces. Figure 25 illustrates a cracked plate which exhibits a non-linear load-displacement curve. If the plate has unit thickness, $A = a$, for load control:

$$\Pi = U - P\Delta = -U^* \quad (23)$$

where U^* is the complimentary strain energy, defined as:

$$U^* = \int_0^P \Delta \cdot dP \quad (24)$$

Combining Equations 24, 23 and 21, yields for load control of the plate in Figure 25 [3, p.109]:

$$J = \left(\frac{dU^*}{da} \right)_P \quad (25)$$

and correspondingly for crack growth at a fixed displacement [3, p.109]:

$$J = -\left(\frac{dU}{da} \right)_\Delta \quad (26)$$

According to Figure 25, dU^* for load control differs from $-dU$ for displacement control by the amount $\frac{1}{2}(dP \cdot d\Delta)$, which is negligibly small compared to dU . This implies that J for load control is equal to J for displacement control [3, p.109].

In order to determine the J-integral, a multiple specimen technique could have been applied, as proposed by Landes and Begley [56][8]. Because of the compromise between production time and cantilever quality, it is preferable to use a single specimen technique. The ASTM standard for the determination of the J-integral relies on very accurate measurements of the crack extension [44]. This work relies on unloading to get data on the crack extension, which is addressed in Section 2.4.1. If unloading was done with very small intervals it would become a low cycle fatigue experiment instead of a fracture experiment. For this reason, as proposed by Wurster et al. [95], the J-values will be calculated using an older standard [43]. This older standard is in good agreement with the theory on crack growth by Anderson [3, p.127]. $J_{(i)}$ at the unloading step i , is given as the sum of elastic and plastic components, respectively:

$$J_{(i)} = \frac{(K_{(i)})^2(1 - \nu^2)}{E} + \frac{\eta \cdot A_{pl}(i)}{w(b^* - a_0)} \quad (27)$$

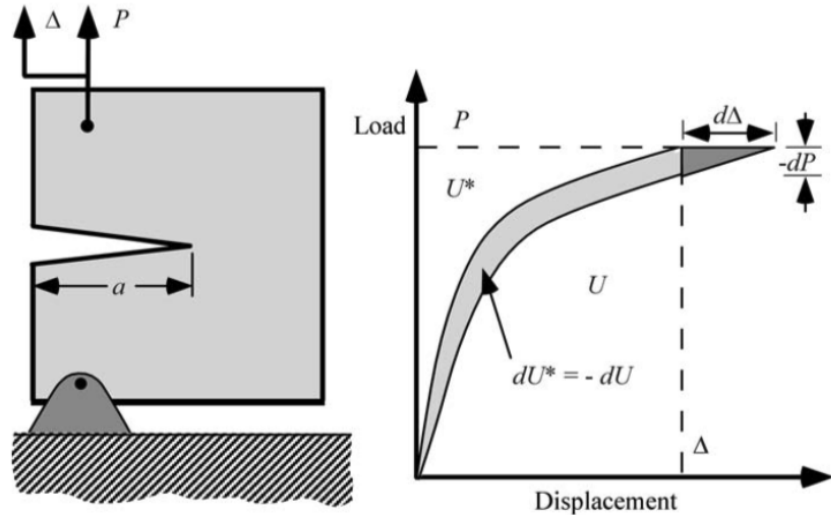


Figure 25: Non-linear energy release rate for a cracked plate with unit thickness, $A = a$. Adapted from [3, p.109].

where $K_{(i)}$ is determined by Equation 11, η is a constant factor equal to 2 and ν is the Poisson's ratio. $A_{pl}(i)$ represents the area beneath the load versus displacement curve, excluding a triangle that is defined by the unloading line, and $(b^* - a_0)$ represents the initial ligament.

Wurster et al. presents two ways of evaluating the $J-\Delta a$ curve [95]. The first is based on determination of the critical unloading step, which is determined from a crack extension curve, which is then used to evaluate the J-curve to obtain a critical J-value.

The second way of determining the critical J-values is to fit the data to two linear functions. One linear fit for the initial part, based on all equal cantilevers, and individual fits for the final part of each cantilever. An example of this fitting is illustrated in Figure 26. The intersection between these two straight lines holds the J-value at the transition from one stage of fracture to the other and is used to determine the fracture toughness.

The fracture toughness, $K_{Q,J}$, can be calculated from the J-integral using:

$$K_{Q,J} = \sqrt{\frac{JE}{1-\nu^2}} \quad (28)$$

ASTM Standard E813 restricts the initial ligament size $(b^* - a_0)$ and the width, w , to be greater than

$$(b - a_0), w > \frac{25J_{IC}}{\sigma_Y} \quad (29)$$

with J_{IC} being the critical J-value, i.e., the value at the onset of stable crack extension [43].

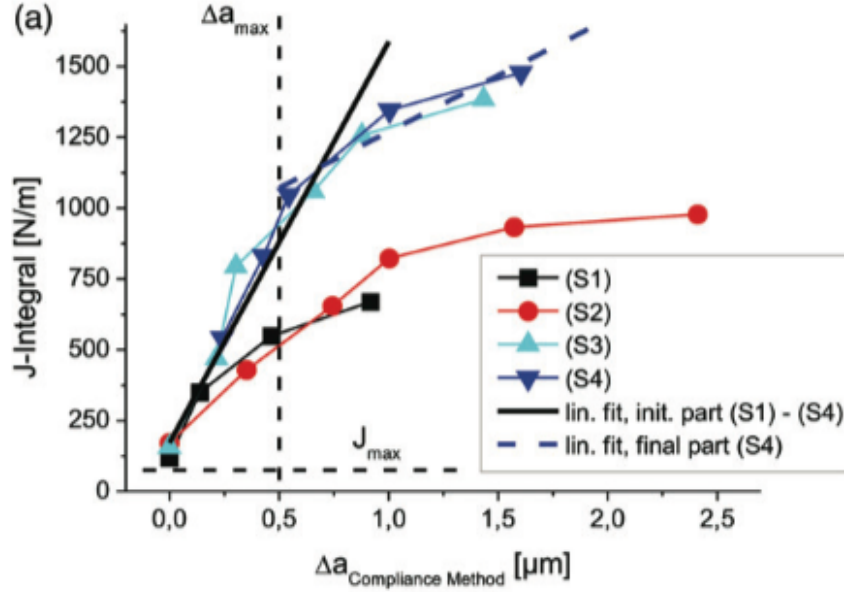


Figure 26: Illustration of the fitting and the determination of critical J-values. The first function is based on data from all the cantilevers. The second linear fit is based on only one cantilever. Adapted from [95].

2.5.2 Crack Tip Opening Displacement

CTOD is a different approach to describe the fracture toughness of a material. To be able to determine this parameter it is common practice, for a macro-sized specimen, to measure the CMOD. This can be used to calculate the CTOD by the assumption that the two parts, divided by the notch, rotate about a hinge point [3, p.103-107]. For this work, the determination of the CTOD will be based on a hinge model of a three-point bend specimen, adapted for notched cantilevers. This model is known from both standards and literature on fracture mechanics [42][3]. The hinge point is assumed to be approximately at the depth of $0.45(b^* - a)$ below the notch front. The CMOD can be measured in the SEM before testing, and then again post-loading, eventually using the model described in Figure 27 to calculate the CTOD. The model can be expressed as:

$$CTOD = CTOD_{elastic} + CTOD_{plastic} \quad (30)$$

where the components are:

$$CTOD = \frac{K_{IC}^2(1-\nu^2)}{2E\sigma_y} + \frac{r_p(b^* - a)CMOD_0}{r_p(b^* - a) + a} \quad (31)$$

where r_p is the rotational factor assumed to be 0.45, K_{IC} is the critical stress intensity, ν is the Poisson's ratio, $CMOD_0$ the initial CMOD.

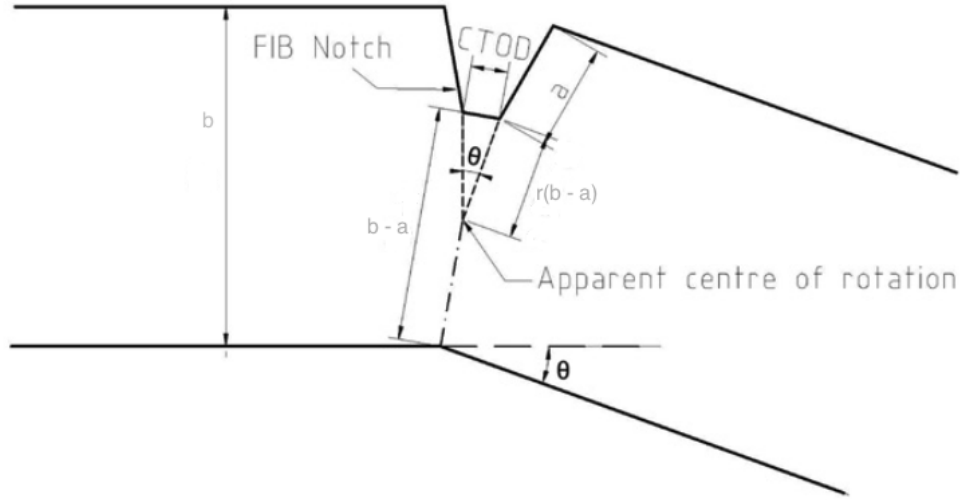


Figure 27: Hinge model adapted for micrometer-sized notched cantilevers. Adapted from [42].

The CTOD can be calculated directly from the relationship with the J-integral, which is given by [3, p.120][95]:

$$CTOD = d_n \frac{J}{\sigma_y} \quad (32)$$

where d_n is the Shih factor, which is 0.78 for plain strain conditions [81].

2.6 Nanoindentation

Nanoindentation is a relatively new method for probing mechanical properties, e.g. hardness and modulus of elasticity. This method enables the establishment of local mechanical properties on the submicron level, increasing the resolution of the mechanical testing relative to microindentation. Previous technologies are based on imaging the indentation crater in order to establish the mechanical properties. Development of equipment able to continuously measure force and displacement permits determination of properties from craters not large enough to efficiently be imaged by regular optical microscopes, thus one is able to probe mechanical properties with augmented resolution [71]. Utilizing an automated nanoindentation instrument facilitates thorough mapping of the specific mechanical properties distributed over the material microstructure. Calculation of the material properties is conducted by analyzing the loading data acquired from one complete loading cycle, i.e., loading and unloading, and estimating the contact area from the indenter tip.

Heinrich Hertz developed load-displacement relationships for elastic indentations for different geometries used when performing indentations. This relationship can conveniently be formulated

as:

$$P = \alpha h^m \quad (33)$$

where P is the applied load, and h is the indenter displacement. α and m are constants; m typically ranges between 1 and 2, depending on the tip geometry. However, the situation complicates when considering plastic deformation of the material. This is due to a necessary consideration of the non-linear constitutive equations, material parameters for the indenter, and the indented material. Since both the indented material and the indenter will experience elastic deformation, it is necessary to compute the resulting effective modulus of elasticity. This is called the reduced modulus of elasticity, and is calculated by the following relationship:

$$\frac{1}{E_r} = \frac{1}{2} \left[\frac{1 - \nu_A^2}{E_A} + \frac{1 - \nu_B^2}{E_B} \right] \quad (34)$$

where E_r is the reduced modulus of elasticity. E_A and ν_A are the Young's modulus and Poisson's ratio for the sample, respectively. E_B and ν_B are the corresponding parameters for the indenter [72][91, p.302]. In order to calculate the modulus of elasticity for the specimen, a correlation between E_r and the load-displacement curves, must be established. Oliver-Pharr proposed the following correlation:

$$S = \frac{dP}{dh} = \frac{2}{\sqrt{\pi}} E_r \sqrt{A} \quad (35)$$

where S is the experimentally measured stiffness, and A is the projected contact area between the specimen and the indenter tip [71]. The stiffness is measured by elastically probing the specimen, measuring the gradient of the upper part of the unloading curve. This is illustrated in Figure 28.

The contact area is the next important parameter to establish, within a reasonable margin of error. This could be achieved by utilizing an AFM or by repeated probing of a material with known properties [71][98][72]. When this relationship is established, one can extrapolate the contact area from the load-displacement curves. Once the contact area is determined, the modulus of elasticity, and the specimen hardness, H , may be computed:

$$H = \frac{P_{max}}{A} \quad (36)$$

However, the method of extrapolating the area of contact in the impression is based on the assumption that the unloading curve is linear; this is not always the case [71].

Recent discoveries show that the Oliver-Pharr method is not satisfyingly accurate [98]. The Oliver-Pharr method assumes sink-in of the specimen during indentation, but the real case is that the material will pile up during indentation. This can be shown by analysing an indentation impression with an AFM; this is illustrated in Figure 29.

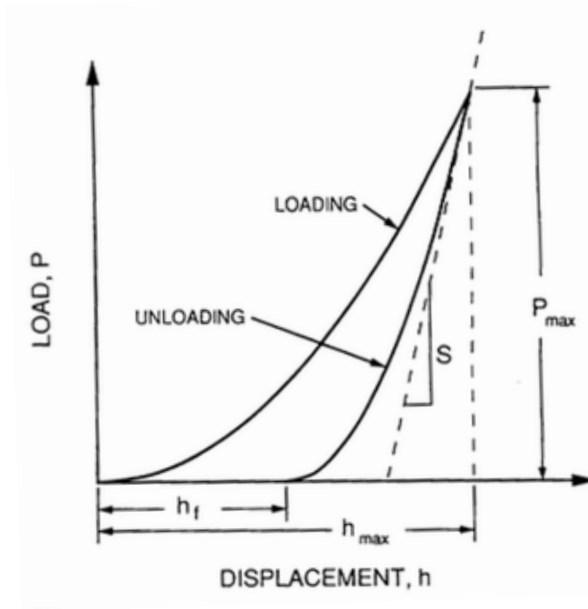


Figure 28: Schematic representation of load versus indenter displacement. The illustrated quantities are the peak indenter load, P_{max} , the calculated stiffness, S , the peak indenter displacement h_{max} , and the initial depth of the impression, h_f . Adapted from [71].

As shown in Figure 30, the depth of the impression, h_c , will vary depending on the material's behavior during indentation. This will affect the accuracy of the calculations, and an improved computational method is therefore required. Li-na Zhu et. al. proposed a way of calculating a mean value for h_c , and the height of the pile up, h_p . These heights may be measured on the edges of the AFM impression. This is illustrated in Figure 30. The real contact area then becomes:

$$A = \sum_{n=0}^8 C_n (h_c)^{2-n} = C_0 h_c^2 + C_1 h_c + \dots + C_8 h_c^{1/128} \quad (37)$$

where C_0 to C_8 are fitting constants [98][72].

The roughness of the prepared sample surface strongly influences the experimental data, since the tip is in the micro- or nano-meter scale. Figure 31 illustrates different scenarios of indenter-sample interaction. The equations are based on perpendicular interaction; smoothness on the nano-meter scale is crucial. Ideally, the specimen surface should be completely plane. This is usually achieved through electropolishing of the sample after mechanical preparation. However, this may prove challenging, depending on the sample material. If the selected material proves difficult to electropolish, chemical polishing with a fine silica suspension may be a viable second choice. This will leave some surface roughness, but deeper indentations should counteract the residual

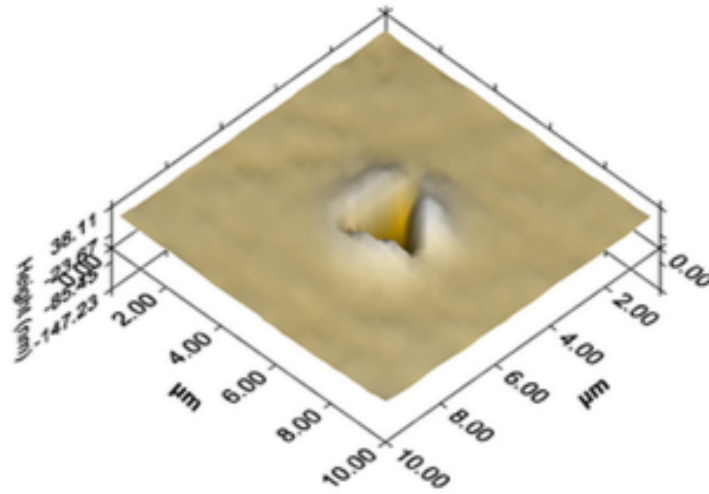


Figure 29: Typical AFM image of the specimen impression. Adapted from [98].

roughness. Deep impressions will ensure full contact with the sample, resulting in comparable data. In order to do this, several trial indentations and calibrations are recommended.

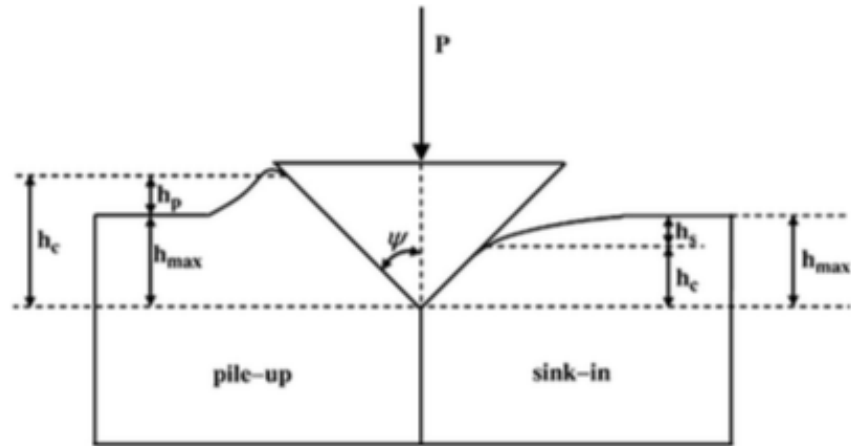


Figure 30: Schematic illustration of possible contact profiles between specimen and indenter. Adapted from [98].

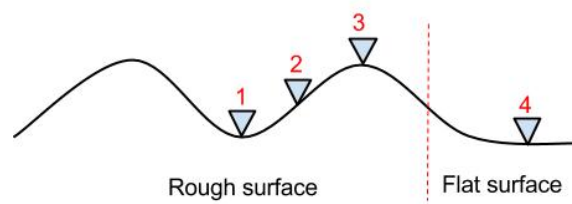


Figure 31: Schematic illustration of different indentation scenarios. Scenario 1-4 yield different results.

2.7 Pillar Compression Testing

Compression testing of pillars is a simple approach to regular tensile testing. Mechanical properties and deformation mechanisms can be obtained and studied using this testing method. The load-displacement data provide precise data of selected material properties. The deformation of pillars with a flat-punch tip, was used to determine the yield strength necessary for analysis of the cantilevers.

High friction between the top of the pillar and the indenter tip may cause undesired edge conditions, which may affect the experimental results. Buckling and barreling are also undesired phenomena. Barreling is caused by high friction between the indenter and the pillar, restraining the top surface, causing the cross section in the middle to expand. This will cause the experimental results to yield an increased UTS. A large height-to-width ratio is undesirable due to buckling. From experience, a ratio below 4, will not result in buckling [87]. Using a FIB it is very challenging to obtain an untapered pillar; tapering may cause all the deformation to occur at the uppermost part of the pillar, making the results hard to analyze.

A detailed description of the active deformation mechanisms and slip systems will not be given in this thesis. The mechanisms are thoroughly described in A.B. Hagen's master thesis [32], and in the specialization project by B.D. Snartland [87].

The experimental data will be converted to engineering stress, σ , and engineering strain, ϵ , by the following equations:

$$\sigma = \frac{4F}{\pi d_{top}^2} \quad (38)$$

$$\epsilon = \frac{\Delta}{h_0} \quad (39)$$

where F is the applied force, d_{top} is the top diameter of the pillars, Δ is the compression displacement, and h_0 is the initial pillar height. Using the top diameter as the determining value when calculating the pillar area, assumes that the pillar has no tapering. However, since most of the deformation occur in the top half of the pillars, this is considered a reasonable assumption.

Research shows that the yield strength is independent of alloying composition for small samples, as long as the variation in composition is low [28][50]. Since the steel is a HSLA steel, it is considered similar to iron at the lower micro level, due to the size effect illustrated in Figure 32. The selected value for the yield stress will therefore also be used in the pure iron cantilever calculations.

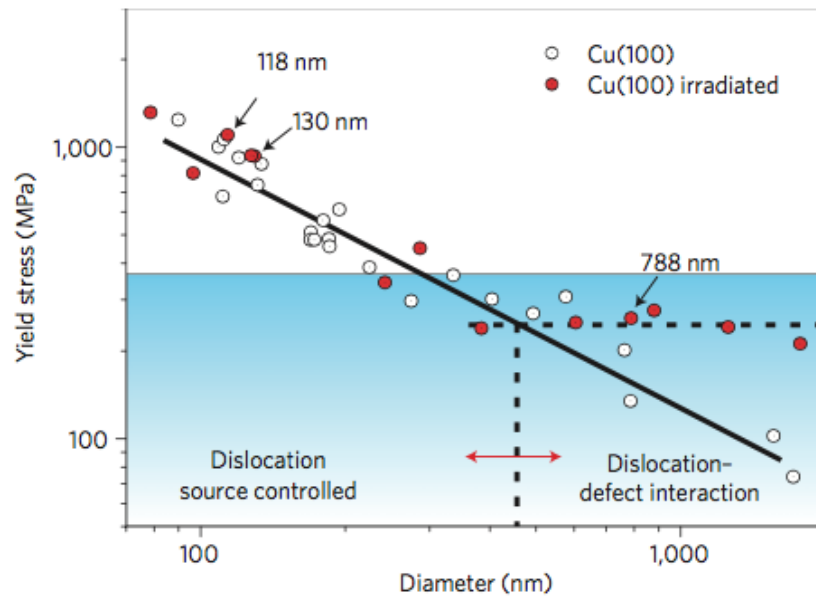


Figure 32: Illustration showing how the yield strength evolves as a function of sample size for similar materials. Adapted from [50].

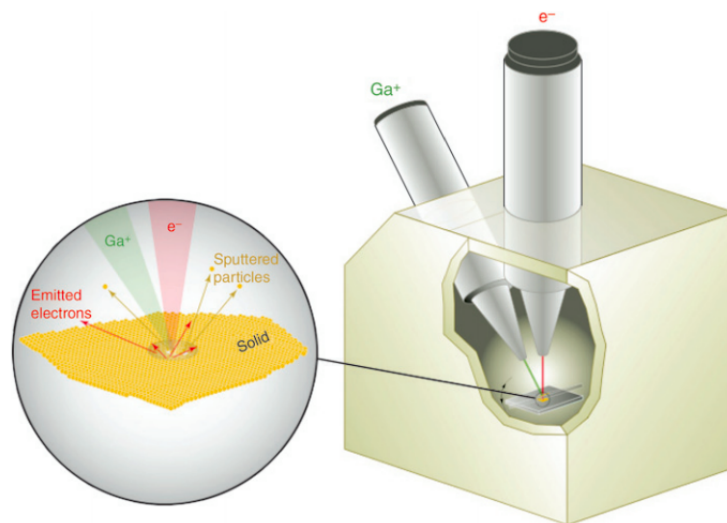


Figure 33: Schematic illustration of a dual-beam FIB-SEM instrument. Expand view shows the electron and ion beam sample interaction. Adapted from [93].

2.8 Focused Ion Beam

To produce the cantilevers and pillars, a FIB instrument was used. A FIB is a scientific instrument that resembles a SEM. However, while the SEM uses a focused beam of electrons, a FIB uses a focused beam of ions instead, e.g. gallium ions. The Ga ion has a much higher energy when accelerated due to its larger mass, which is enough to sputter atoms from a bulk material. A typical FIB instrument has a SEM column, thus making it a versatile dual-beam platform for imaging, material sputtering or deposition. The dual-beam principle is illustrated in Figure 33.

Imaging and milling with Ga ions results in implantation of Ga atoms near the sample surface. The ion beam damage can take the form of sample surface amorphization, point defect creation, dislocation formation, phase formation, grain modification, or other unusual effects. Atom fractions from 1 at.% to 50 at.% are expected near the sample surface [93]. Systematic investigation of FIB damage has been conducted in recent years. In a study conducted on FIB damage on Cu specimens to evaluate possible consequences for miniaturized mechanical tests, concentrations of up to 20 at.% Ga were found several nanometers below the surface. Ga contents of more than 2 at.% were detected within a depth of up to 50 nm [51]. In addition, several defects were found in the bombarded area: point defects, dislocations and precipitates. The contribution of the Ga damaged surface layers to the flow stress evaluated for micron-sized Cu pillars was estimated from several MPa, to the order of GPa for certain hardening mechanisms. Thus, care must be taken for submicron specimen machined using a FIB [51].

3 Experimental Procedure

Section 3 outlines the experimental work conducted in this thesis. The working methods are explained thoroughly. The difficulties encountered are discussed, along with the measures taken to overcome these challenges.

3.1 Material and Sample Preparation

The HSLA steel is manufactured by SSAB. It was delivered to SINTEF in form of 6 plates measuring 50x400x2000 mm. The plates were cut into rods measuring 11x11x100 mm. To produce a CGHAZ, the rods were weld simulated with a peak temperature of 1350 °C, and a cooling rate, $\Delta t_{8/5}$, of 15 s. For the ICCGHAZ, a two-cycle simulation was employed with $T_{p1} = 1350$ °C and $T_{p2} = 780$ °C, with cooling rates of $\Delta t_{8/5} = 15$ s and $\Delta t_{6/4} = 17.2$ s, respectively.

Table 1: Chemical composition.

Element	Wt%	Element	Wt%	Element	Wt%
C	0,019	Nb	0,037	Mo	0,206
Si	0,25	V	0,012	N	0,003
Mn	1,59	Ti	0,011	B	0,0002
P	0,008	Cu	0,257	Sn	0,003
S	0,002	Cr	0,23	Pb	0,0000
Al	0,027	Ni	0,34		

The weld simulated rods were cut into three samples, measuring approximately 2x10x10 mm. The samples were cut from the centre of the weld simulated area, with the thermocouples intact. The thermocouples were used for reference in order to navigate on the sample, but also to make sure that test specimens were not manufactured in the proximity of the couples. The area around the thermocouples experienced a higher cooling rate than intended when the heat input was cut.

The samples were ground and polished. This process was performed stepwise, reducing the roughness of the grinding paper between every step. The samples were washed in an ultrasonic bath filled with ethanol before each polishing step.

After grinding and polishing, the samples were etched with Nital for 10 s in order to reveal the microstructure. This step was necessary in order to achieve high quality pictures in an optical microscope. However, this step left a certain surface roughness, which was removed before proceeding to nanoindentation and FIB machining. The same procedure outlined above was re-employed.

Table 2: Main grinding and polishing steps.

Grinding	
Step	Paper grit
1	120
2	220
3	500
4	1000
5	2500
Polishing	
1	3 μm
2	1 μm

The sample was polished with OP-U, which is a multipurpose colloidal silica suspension, for 5 min, after the final traditional polishing step. This was done as an alternative to traditional electro-polishing, which proved difficult for the HSLA steel. The resulting surface quality was deemed sufficient when performing nanomechanical testing and nanoindentation.

The ICCGHAZ and the CGHAZ were suspected to contain a small volume fraction of MA constituents. This phase is not revealed by traditional attack-etching, and requires a more specialized etching procedure. For this thesis the LePera etching method was copied from the original article, written by F.S. LePera [58]. The etch consists of a mixture of two solutions, which must be combined moments before etching. The first solution consisted of 4% picric acid diluted in ethanol, and the second solution consisted of 1 g sodium thiosulfate mixed in 100 mL distilled water. The samples were submerged in the etch until the surface turned murky yellow. This occurred after roughly 5 – 10 s. After this step, the samples were washed with ethanol and dried, turning the surface brown with a blue tint. The samples were subsequently imaged in an optical microscope and SEM for characterization purposes. The LePera etch requires picric acid which is a controlled substance. This acid is hard to obtain, and the quality of the acid varies. The first picric acid obtained was of inadequate quality, causing the first set of etching experiments to yield unsuccessful results. This issue was rectified for the second acid obtained, which proved of adequate quality.

3.2 Machining of Test Specimen

To produce pillars and cantilevers at a micro scale, a FIB instrument was used. Within the same material, the sputter rate, which quantifies how quickly the FIB removes atoms from the sample, varies with the orientation. For pure iron, within a single grain, this rate is more or less uniform, allowing predictable behavior. Steel, especially with bainite-like structures, is chaotic and yields great variations within the same grain. For this reason a step-by-step procedure for milling is not

producibile. The milling process is an iteration process with an undefined number of steps. In this section a series of main steps will be proposed.

It is necessary to be deliberate while machining, because of potential FIB damage, which is mentioned in Section 2.8. This includes avoiding utilization of the actual FIB imaging function more than necessary, especially while using higher currents and larger magnifications. This may quickly ruin the geometry and sharp corners, and introduce unnecessary gallium to the surface, eventually affecting the mechanical properties.

The principle that this is an iterative process must be emphasized; the test specimen may be ruined with even the slightest miss-step. Long, time consuming steps are not recommended due to drift in the system. During milling the FIB system had a tendency to display more drift for the first hours of work after a new sample had been loaded. The best results are obtained by series of short steps with duration between 1 and 3 minutes. For many steps a range of parameters is given. It is desirable to use the rougher parameters first, and then move on to the finer, and more time consuming parameters, as the process is iterated.

3.2.1 Cantilevers

This section outlines how to use a FIB to produce pentagonal cantilevers in a HSLA steel. The desired geometry and definition of symbols are presented in Figure 22 in Section 2.4. The desired dimensions are presented in Table 3. The procedure for milling in steel is outlined in Table 4. A thorough step-by-step guide for pure iron can be found in K. Greina's master thesis [29] and the specialization project by A.L.L. Kvaal [53].

Table 3: Desired cantilever dimensions.

Unit name	Unit symbol	Length [μm]
Bending length	L	10
Height	b	1
Width	w	1
Crack depth	a	0.4

The notch is hard to produce because of an unpredictable sputter rate and redeposition of material while milling. These parameters vary from material to material, so this needs to be assessed for every new material tested. It is also hard to measure the notch depth, because of insufficient resolution and contrast while using a traditional SEM. This will be measured post-fracture by analysing the fracture surface. In order to mill a notch of $\sim 0.4 \mu\text{m}$, a series of tests with different parameters for line patterns was conducted with a cleaning cross section executed to evaluate the notch depths. An illustration of the tests is presented in Figure 34. It was found that using $z = 1 \mu\text{m}$ and a current of 28 pA, produced a decent notch for both pure iron and the HSLA steel.

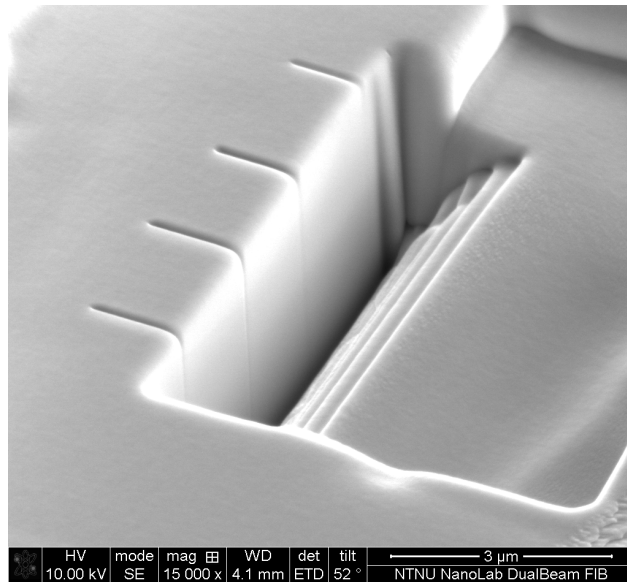


Figure 34: Tests conducted to determine FIB parameters to obtain a decent notch profile and depth. The material in this image is pure iron.

Table 4: FIB milling procedure for cantilevers in a HSLA steel.

Illustration	Description and parameters
	<ul style="list-style-type: none"> – Pattern type: Rectangle. – Beam current: 21 nA. – Sample tilt: 52° to SEM axis. – z: 10 μm <p>The purpose of this step is to create space for sputtered material to escape, and for the displacement of the cantilever. The goal is to have a pit 10 μm deep. The beam should have a width of 3 – 3.5 μm and length of 13 – 15 μm.</p>
Continued on next page	

Table 4 – continued from previous page

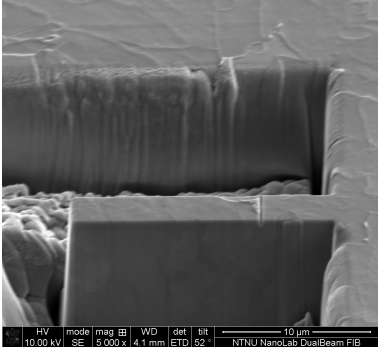
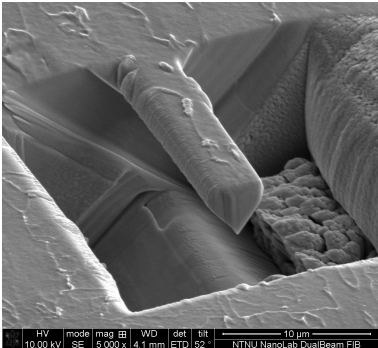
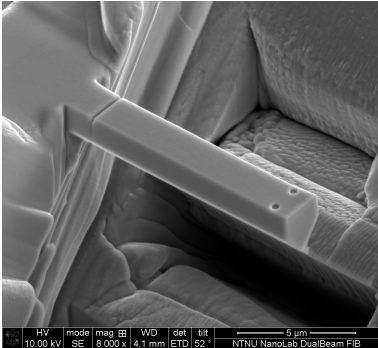
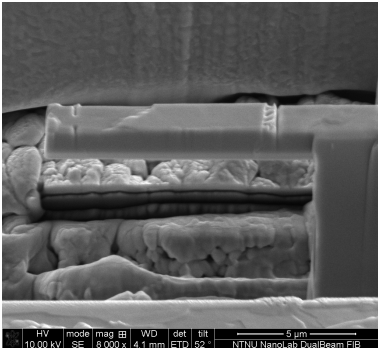
Illustration	Description and parameters
	<ul style="list-style-type: none"> – Pattern type: Regular cross section. – Beam current: 2.8 – 0.92 nA. – Sample tilt: 52° to SEM axis. – z: 2 μm <p>The purpose of this step is to remove unnecessary material in a controlled manner, making the edges sharper. The goal is to have the width down to 2.5 – 3 μm.</p>
	<ul style="list-style-type: none"> – Pattern type: Regular cross section. – Beam current: 2.8 – 0.92 nA. – Sample tilt: 7° to SEM axis. – z: 1 – 2 μm <p>The purpose of this step is to remove the material underneath. This is done by tilting the FIB 45° to the sample surface, which is equal to tilting the sample 7° to the SEM axis. The height of the cantilever, b, should be about 2 – 2.5 μm. This obtained by iterating, i.e., gradually closing in to the desired height. A 180° rotation of the sample is required to reach the other side of the cantilever.</p>
Continued on next page	

Table 4 – continued from previous page

Illustration	Description and parameters
	<ul style="list-style-type: none"> – Pattern type: Line and circle. – Beam current: 28 pA. – Sample tilt: 52° to SEM axis. – z_{notch}: 1 μm and z_{marks}: 0.3 μm. <p>The purpose of this step is to make a notch, and loading marks at a known bending length, L. The image is taken from a pure iron test specimen to better illustrate the principle.</p>
	<ul style="list-style-type: none"> – Pattern type: Cleaning cross section – Beam current: 0.46 nA. – Sample tilt: 52° and 7° to SEM axis. – z: 1 μm. <p>The purpose of this step is to achieve the exact geometries desired. Extreme care must be taken through the meticulous iterative process. Obtaining the exact geometry and symmetry is difficult and time consuming. It is recommended to acquire the width first, and then tilt the sample to obtain the desired height.</p>

3.2.2 Pillars

This section outlines how to use a FIB to produce pillars in a HSLA steel. A thorough step-by-step guide for pure iron can be found in the master thesis by A.B. Hagen [32] and the specialization project by B.D. Snartland [87]. The desired dimensions for the pillars are presented in Table 5. The pillars have to be within a certain height-to-width ratio. This criteria is further discussed in the work done by B.D. Snartland. There are no tilting operations involved in the production of pillars. All operations are done with the FIB normal to the surface, i.e., 52° to the SEM axis.

Table 5: Desired pillar dimensions.

Unit name	Unit symbol	Value
Height	h	3 – 4 μm
Diameter	d	1 μm
Criteria	h/d	<4

Table 6: FIB milling procedure for pillars in a HSLA steel.

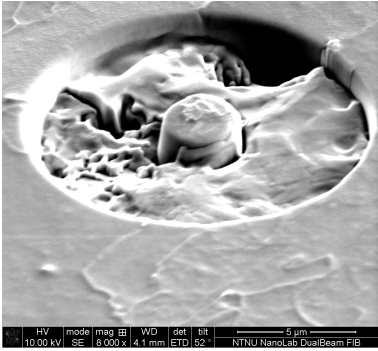
Illustration	Description and parameters
	<ul style="list-style-type: none"> – Pattern type: Circle. – Beam current: 2.8 nA. – Outer diameter: 14 μm. – Inner diameter: 4 μm. – z: 0.5 μm. <p>The purpose of this step is to create space for sputtered material to escape, and for the compression of the pillar. The goal is to have a pit with a uniform depth of $\sim 0.5 \mu\text{m}$, which is often not achieved with the first pattern.</p>
Continued on next page	

Table 6 – continued from previous page

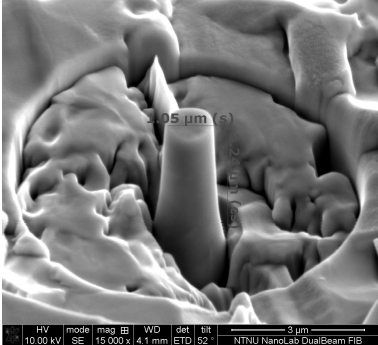
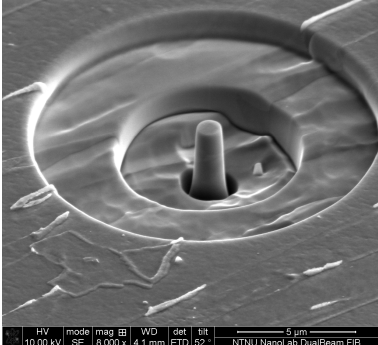
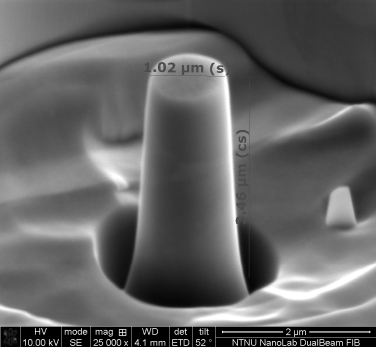
Illustration	Description and parameters
	<ul style="list-style-type: none"> – Pattern type: Circle. – Beam current: 0.46 – 0.28 nA. – Outer diameter: 8 μm. – Inner diameter: 1.5 μm. – z: 0.3 μm. <p>The purpose of this step is to reduce the diameter of the pillar. The goal is to have a pillar with the diameter of ~1.2 μm and the same height around the base of 3.5 – 3 μm. Because of different sputter rates in adjacent grains this may be difficult, and step 3 may be necessary. If iteration is necessary, one can reduce the outer diameter and z-value for each step.</p>
	<ul style="list-style-type: none"> – Pattern type: Polygon or cleaning cross section. – Beam current: 0.46 nA. – z: 0.2 μm. <p>The purpose of this step is to even out differences in depth around the pillar. The pillar should have a uniform height around the base. This step is optional, but must be carried out if there are great differences in milling rates. This is typical when pillars are machined on grain boundaries.</p>
<p>Continued on next page</p>	

Table 6 – continued from previous page

Illustration	Description and parameters
	<ul style="list-style-type: none"> – Pattern type: Polygon or cleaning cross section. – Beam current: 28 pA. – Outer diameter: 2.5 μm. – Inner diameter: 1.2 μm. – z: 0.13 μm. <p>The purpose of this step is to reduce the tapering of the pillar. The step can be repeated for a better result, but the z-value should be reduced with each iteration. Too many iterations of this step may cause the top to become rounded.</p>

3.3 Nanoindentation

One of the prepared CGHAZ samples was tested by nanoindentation in a Hysitron TI-950 TriboIndenter. The surface was polished using OP-U and was not etched. Attack-etching results in an increased roughness, which is disadvantageous when performing nanoindentations. This is elaborated upon in Section 2.6. Without etching, it is not possible to distinguish the microstructure, forcing the experiment to be conducted blindly.

The idea behind this experiment was to use the nanoindenter as a microstructural characterization tool by performing several thousand indentations. These indentations were to be placed in a grid covering an area of the microstructure, and thereby retrieving data capable of creating a topographic map of the hardness of the microstructure. Lack of equipment caused the number of experiments to be restricted to one, and the number of indentations to 49.

The 49 indentations were placed in a grid, with a 6 μm separation between the indentations, which is approximately the same separation as used by S. Dziazyk et al. [25]. A schematic illustration of the mesh is presented in Figure 35, and an image of the indentations from the Hysitron TriboIndenter is presented in Figure 36. The indentations are highlighted and marked in Figure 37.

3.4 Low Temperature Nanomechanical System

The nanomechanical cryogenic system used in this thesis was developed by A.B. Hagen and K. Greina in 2013. The same set-up was used by B.D. Snartland and A.L.L. Kvaal in the specialization project work in 2014. This cryogenic system is thoroughly described in the previous work of

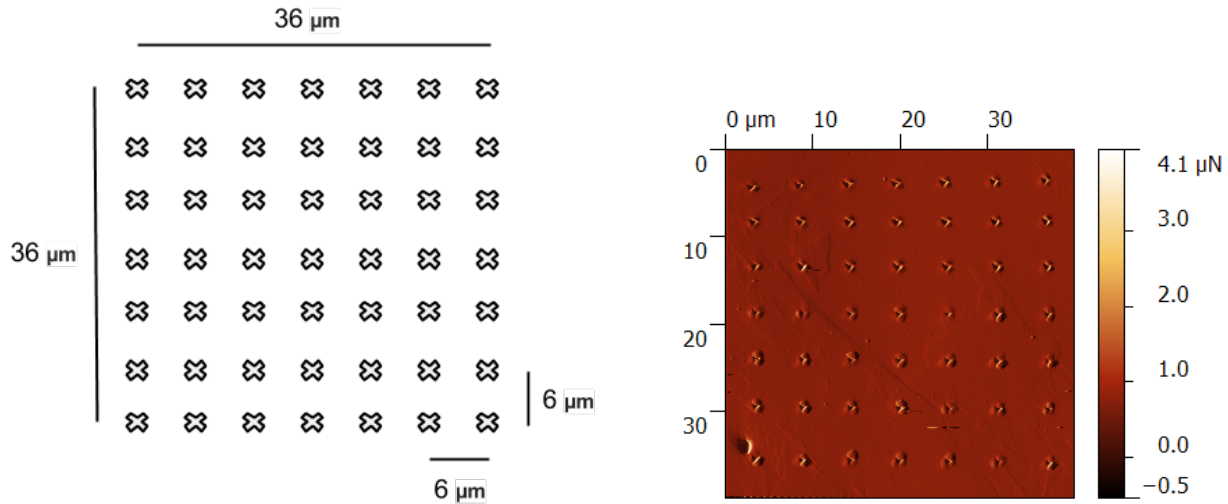


Figure 35: Schematic illustration of the mesh used to place the indentations.

Figure 36: Image of the indented surface, captured from the Hysitron TriboIndenter optical camera.

the aforementioned students [29][87][53][32]. However, in the project work in 2014, some problems with the system were discovered. The indenter tip was not cooled, resulting in unreliable experimental data. The sample was cooled to $-90\text{ }^{\circ}\text{C}$, while the tip was RT, resulting in a heat flow between the two components.

The improved design is schematically illustrated in Figure 38. Improvement of the cryogenic system was a collaborative work between A.B. Hagen, B.D. Snartland and A.L.L. Kvaal. The final design was inspired by research groups from CalTech [57] and UC Berkeley [63]. In order to cool the indenter tip, the cold finger had to be branched. The new branch was connected to the Hysitron PicoIndenter PI-85 frame. The copper block fastened to the frame was insulated by a layer of vacuum compatible Teflon, in order to hinder extensive cooling of the transducer and indenter frame. The copper block was connected to the indenter by 10 layers of thin aluminium foil. The layers of aluminium foil were not interconnected in order to minimize the stiffness. Copper foil was initially used, but the stiffness of the copper foil, acting as a support, affected the calibrations of the indenter. The aluminium foils were glued with silver paste to a custom aluminium extension at the indenter rod. This extension was manufactured by the Finmekanisk Verksted at NTNU. Finally, the indenter tip was attached to the extension. The set-up is presented in Figure 39. Figure 40 shows the cryogenic system after it is installed on the SEM stage.

In order to test the cryogenic system, various cooling experiments were performed, with the goal to verify that the tip was sufficiently cooled, and to check if the PI-85 was able to perform acceptable calibrations with configurations. The system was set up under full experimental conditions, and

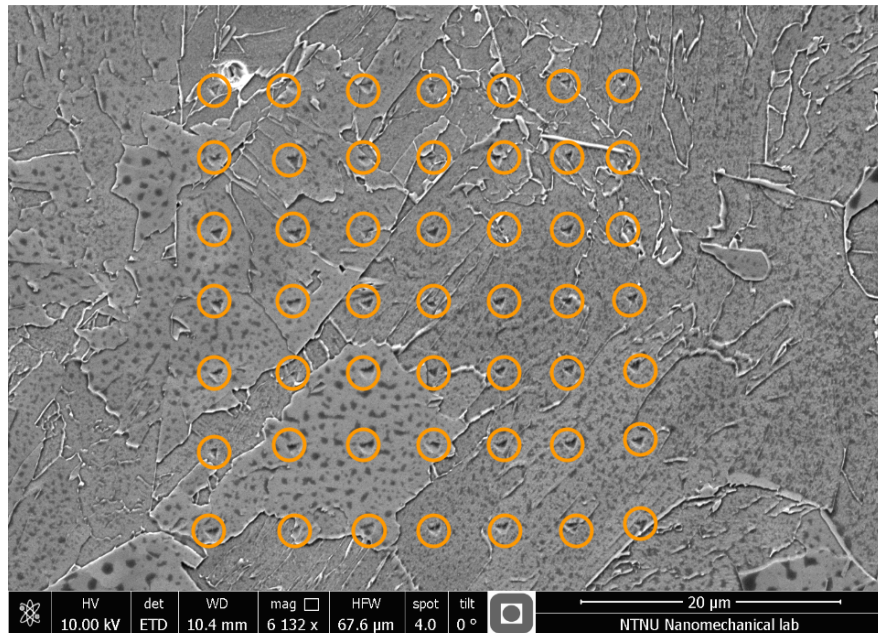


Figure 37: Image of the indentation after etching. Each indentation is highlighted by an orange circle.

liquid nitrogen was introduced. The temperatures of the tip and the sample were logged every ~15 min. The cooling experiments were conducted with 1, 5, and 10 layers of aluminium foil, and the cooling curves are presented in Figure 41. Figure 42 shows that the system calibration with 10 layers of aluminium foil was satisfactory.

3.5 Pillar Compression

The experimental procedure used in this thesis is almost identical to that described in the specialization project by B. D. Snartland [87]. The sample was installed on the PI-85 PicoIndenter stage. Two pillars were compressed at RT, and two at -80°C . A $4\ \mu\text{m}$ wide flat-punch tip was used for the compression of pillars. Table 7 displays the testing parameters used in the experimental procedure.

During the experimental work in B. D. Snartland's specialization project, thermal drift was observed. This was believed to be caused by the temperature difference between the indenter tip and the sample, described in Section 3.4. This drift was not observed during the experimental work in this thesis, and was likely avoided by the improvements to the cryogenic system.

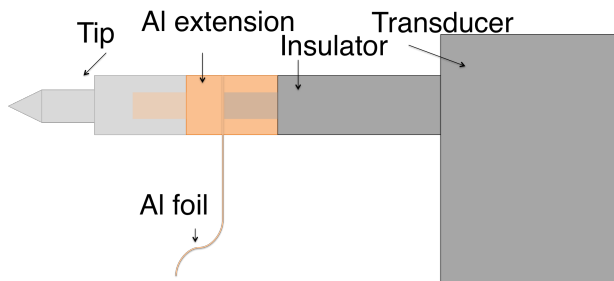


Figure 38: Schematic illustration of cryogenic set-up for the indenter tip.

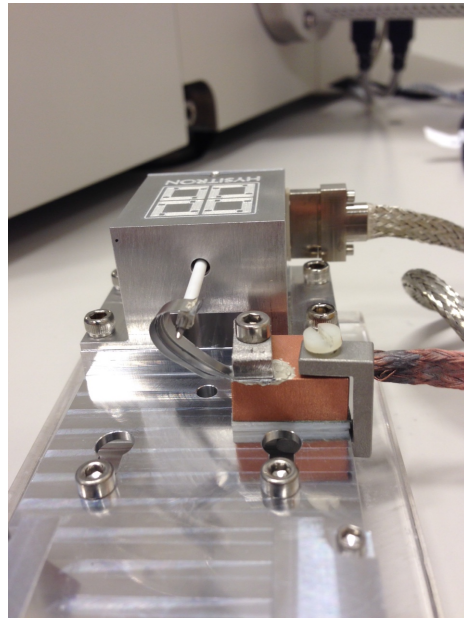


Figure 39: Image of the cryogenic set-up for the indenter tip.

3.6 Fracture Mechanical Testing of Cantilevers

The cantilevers were loaded using the same system and set-up as the pillars; a cube corner tip was installed instead of the flat punch tip. The 90° tip is made of conductive diamond, with a tip radius <40 nm. Figure 44 shows the indenter tip. A sharp tip is chosen in order to minimize the friction stress between the cantilever and the tip.

The cantilevers were loaded at room temperature and at approximately -80°C . Earlier experiments by K. Greina [29], and A. L. L. Kvaal [53], used an open-loop loading function, while attempting to measure the crack growth in-situ during the experiments. Obtaining accurate information on the crack growth was difficult with this approach, therefore the unloading stiffness method was employed. This method is described in Section 2.4.1. This method requires a displacement controlled loading function, which is difficult; several parameters in the Hysitron software require tuning. This is illustrated in Figure 45. Table 8 presents the parameters used during the automated approach and the repeated loading of the cantilevers.

Three of the pure iron cantilevers were tested prior to the PID tuning, which resulted in extremely unstable loading of the cantilevers. The first cantilever was completely razed due to instabilities during loading. The second loading was successful, though in retrospect this might have been by chance. After the indenter razed the third cantilever, the loading function was changed, because the instabilities occurred only at higher displacements. The new loading procedure consisted

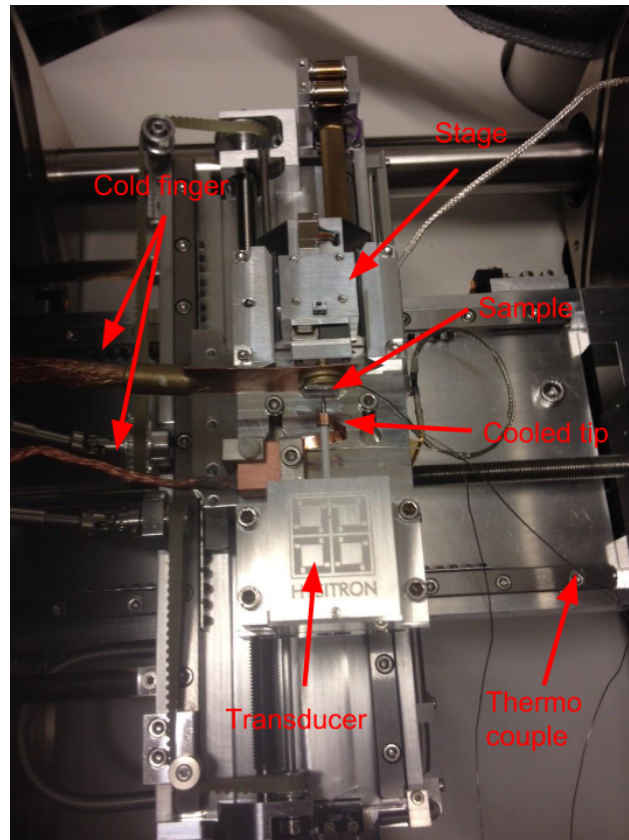


Figure 40: Image of the complete system installed on the SEM stage.

of several short loading runs, instead of performing the whole sequence in one run. All remaining cantilevers were loaded using the repeated loading method; Figure 46 shows the loading function used for this purpose. Figure 47 shows the placement of the indenter as the first loading run is initiated.

3 EXPERIMENTAL PROCEDURE

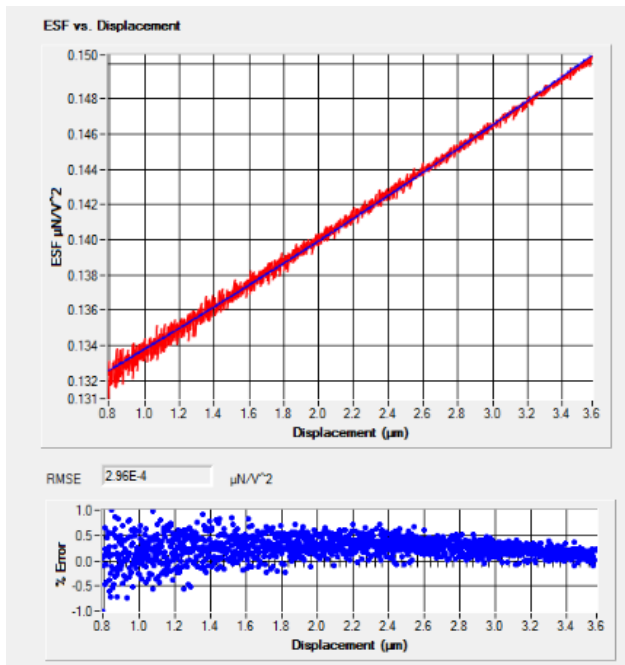
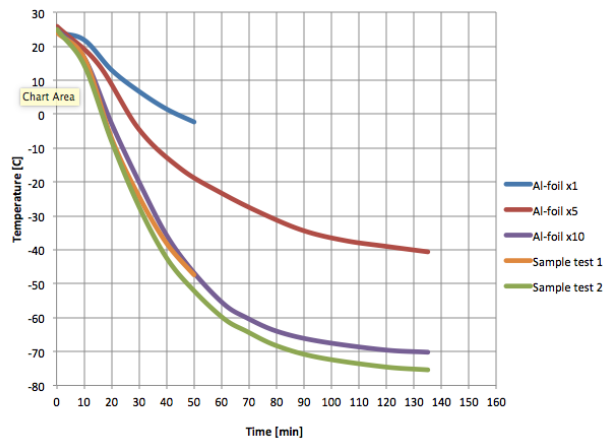


Figure 41: Temperature curves of the sample and tip; **Figure 42:** Calibration curve from the Hysitron PI-85 software, with 10 layers of aluminium foil.

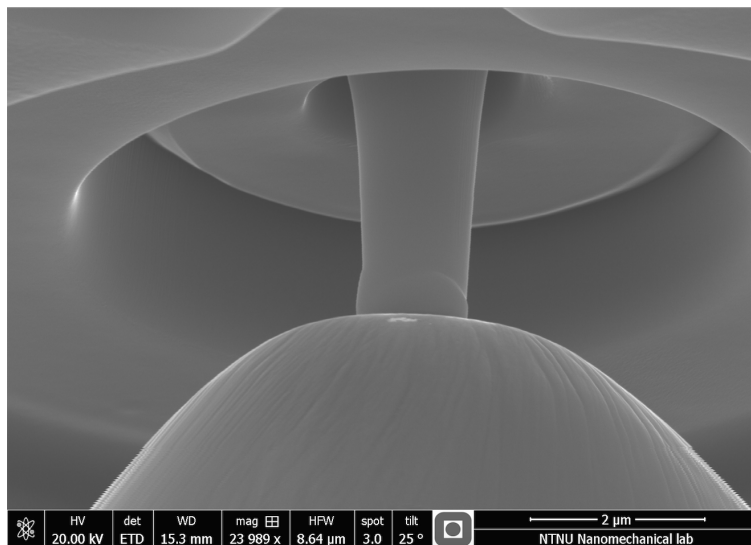


Figure 43: SEM image of compression testing in progress.

Table 7: Parameters used during pillar approach and compression testing.

Approach		Compression	
Step size [nm]	10	Q-gain	0.06
Velocity [$\frac{nm}{s}$]	50	Peak force [μN]	5000
Force threshold [μN]	20	Loading rate [$\frac{\mu N}{s}$]	50
Back off distance [nm]	50	Back off distance [nm]	100

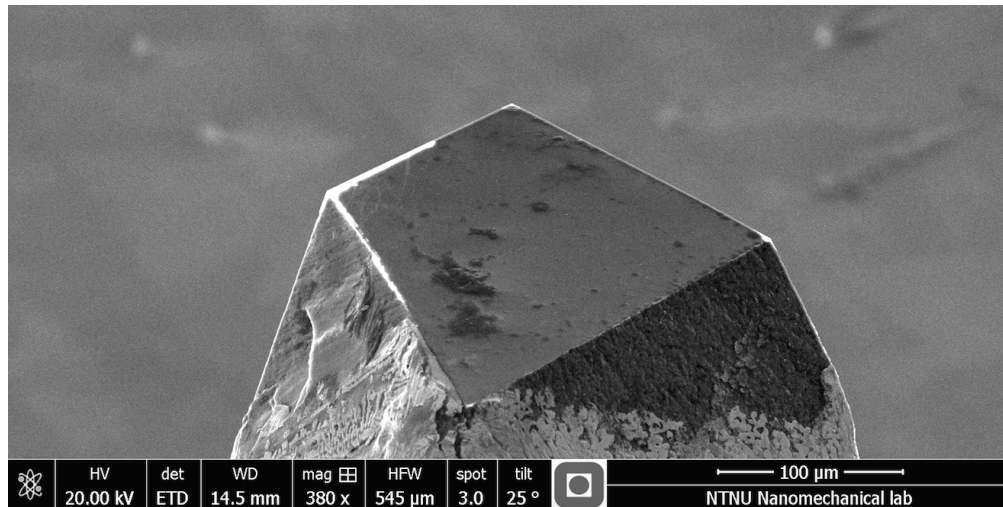


Figure 44: Image of the cube corner tip used for cantilever loading.

Table 8: Parameters used during cantilever approach and displacement controlled loading.

Approach		Loading		PID	
Step size [nm]	10	Q-gain	0.05	Proportional	0.07
Velocity [$\frac{nm}{s}$]	50	Peak displacement [nm]	2000	Integral	0.3
Force threshold [μN]	20	Loading rate [$\frac{nm}{s}$]	16,67	Derivative	0.07
Back off distance [nm]	50	Back off distance [nm]	50	Adaptive	0

3 EXPERIMENTAL PROCEDURE

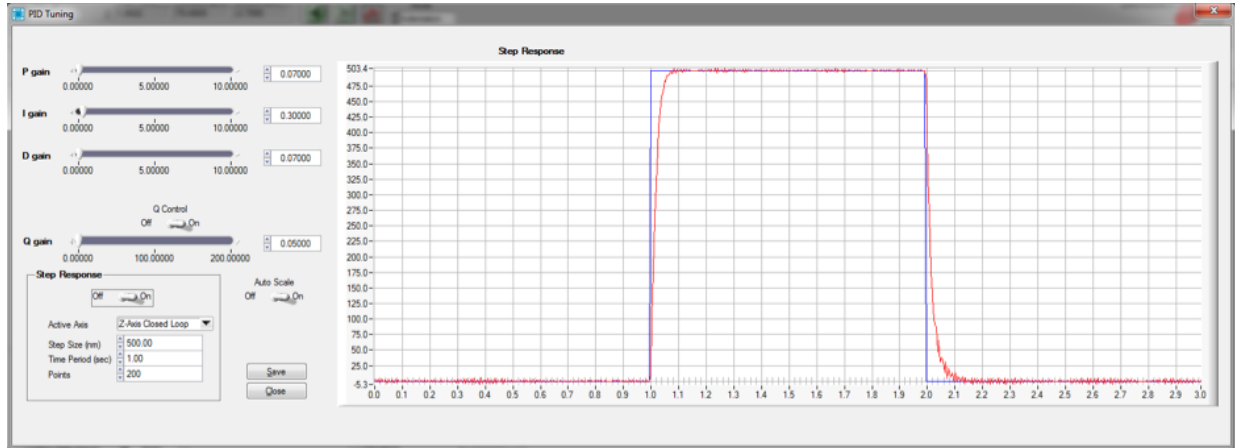


Figure 45: PID tuning interface in the Hysitron software.

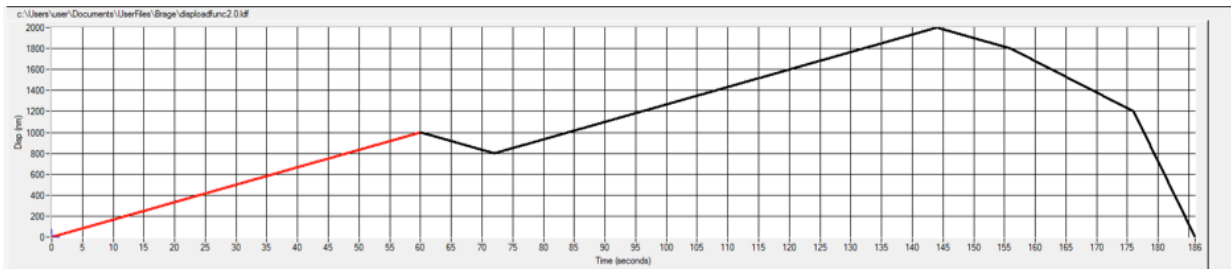


Figure 46: The displacement controlled loading function used for repeated loading runs.

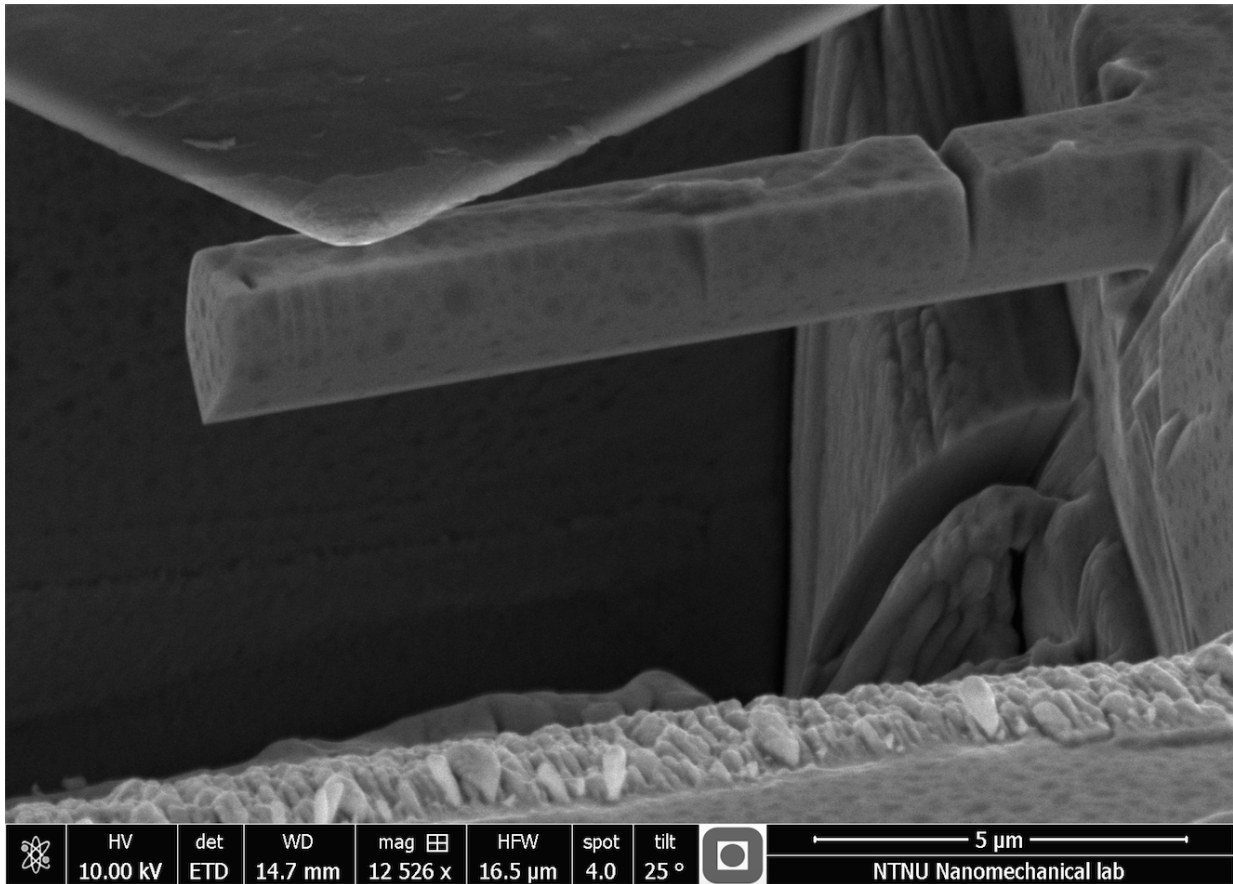


Figure 47: Image of the cantilever and indenter positioning at initiation of the first loading run.

4 Results and Discussion

Section 4 outlines the results from the experimental work conducted in this thesis. The results will be analysed and discussed according to section 2.

4.1 Characterization of the Microstructure

In order to properly assess the microstructure, both optical and electron microscopy were employed. Optical microscopy produces images with colors that are convenient to differentiate the types of microstructure. CGHAZ and ICCGHAZ samples are compared in Figures 48 and 49. Both types of HAZ display what resembles a highly bainitic structure. Upper bainite, lower bainite and martensite are often hard to distinguish, and are sometimes used interchangeably when discussing a microstructure on a general level. There are not any clear visible differences in the microstructure, which is expected at this magnification. The MA constituents are expected to be up to 7 μm , but they are hard to see with regular Nital etching and optical microscopy.

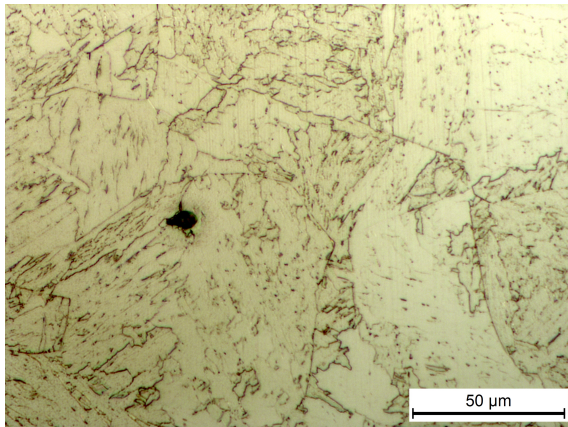


Figure 48: Optical micrograph of the CGHAZ. 50 X, Nital etch.

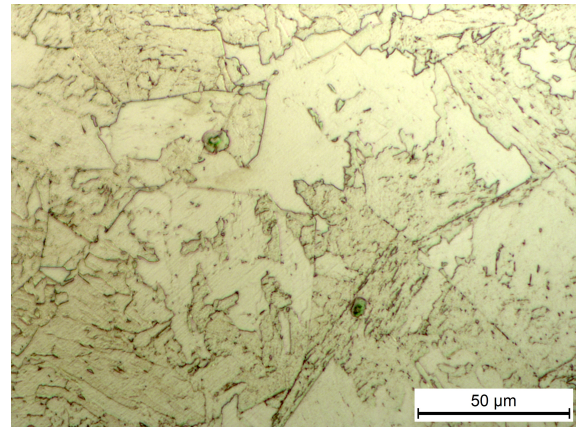


Figure 49: Optical micrograph of the ICCGHAZ. 50 X, Nital etch.

The MA constituents described in Section 2.1.4 are interesting for this work. Identifying these can be difficult and an advanced procedure using controlled substances, described in Section 3.1, was used to enhance the contrast of these phases. Using this type of etch, the MA constituents display a brighter contrast to the bulk material; however, other impurities may display similar effects, and the shape and location must be evaluated to be able to conclude that MA phases are present. In Figures 50 and 51 optical micrographs of the CGHAZ and the ICCGHAZ are displayed respectively, after treated with the LePera etchant.

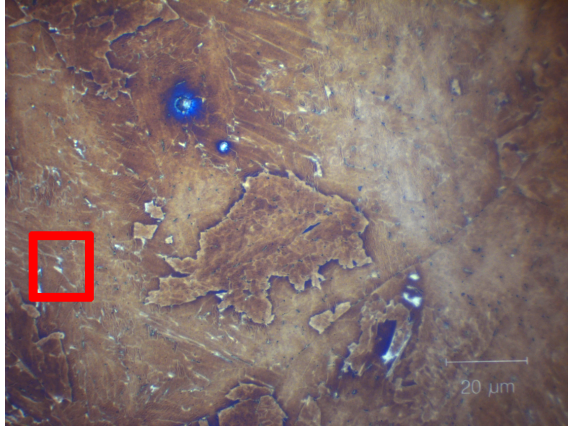


Figure 50: Optical micrograph of the CGHAZ. 100 X, LePera etchant.

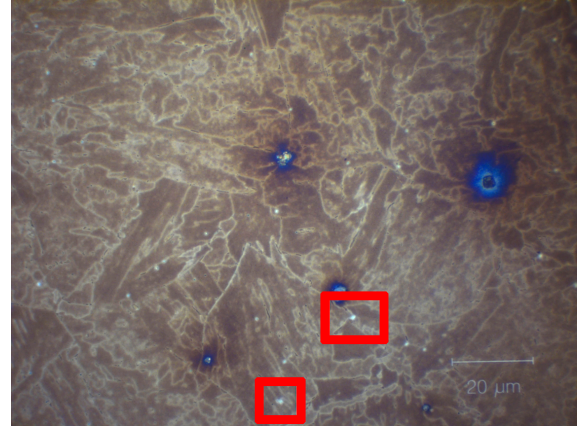


Figure 51: Optical micrograph of the ICCG-HAZ. 100 X, LePera etchant.

SEM imaging was used to produce images with higher magnification. Results are presented in Figures 52 and 53. Examination and comparison of the two HAZs yielded that there was not much difference in size, shape or amount of the MA constituents. The MA particles were identified at both prior austenite grain boundaries, and at bainite lath boundaries. C.G. Hartwig [35] conducted a more thorough examination of the same steel and weld simulations parallel to the experiments in this thesis. Her findings are in good agreement with this result. Her work also concluded that the blocky phases were typically smaller than $1\ \mu\text{m}$, while the stringer constituents were no longer than $\sim 2\ \mu\text{m}$.

4.1.1 SINTEF Weld Screening

SINTEF conducted a thorough screening of the material for the Arctic Materials II project, of which this work is also a part [83]. This report found that the maximum hardness of the HAZ was relatively close to that of the base metal. The maximum HAZ hardness varied between 198 and 225 HV_{10} , while the base metal had a range from 189 to 211 HV_{10} . When real welds were compared with weld simulated samples, the weld simulated samples were found to have greater hardness, and no difference between the hardness of the single cycle and the double cycle specimens. The weld simulated samples had hardness of around 250 HV_{10} .

Tensile experiments were conducted and stress-strain curves were produced to evaluate the yield strength. For the base metal, the yield strength, $\sigma_{0.2}$, was determined to be 480 and 491 MPa, for RT and $-60\ ^\circ\text{C}$, respectively. The UTS was determined to be 575 and 626 MPa for the same temperatures, respectively.

Charpy V notch experiments were performed to evaluate the toughness of the steel. Surpris-

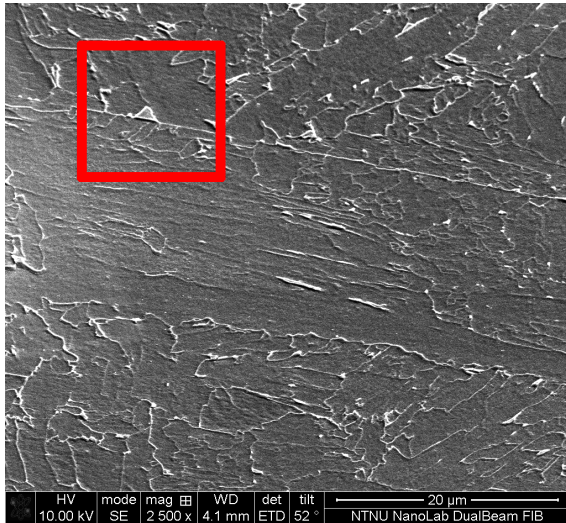


Figure 52: SEM micrograph of the CGHAZ. MA constituent is highlighted.

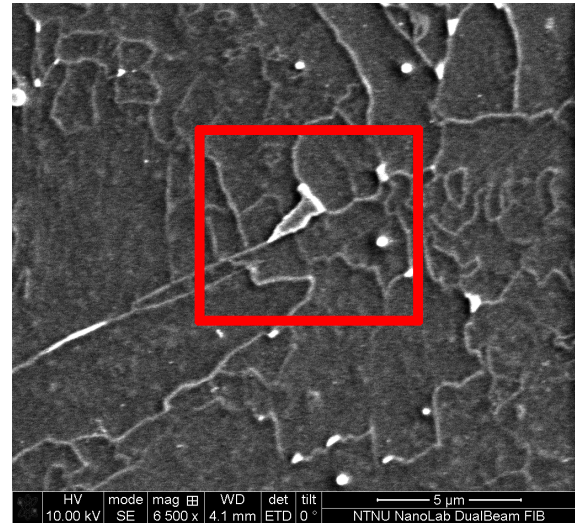


Figure 53: SEM micrograph of the ICCGHAZ. MA constituent is highlighted.

ingly, the CGHAZ and ICCGHAZ toughness levels seemed to increase with increasing $\Delta t_{8/5}$ values (increasing heat input), which is contrary to the trend normally observed in such experiments. The ICCGHAZ impact properties were low (< 50 J). The steel's low carbon content should prevent the formation of blocky MA particles, but this thesis concludes that these are indeed present.

The weld simulated microstructure was also examined. Bainite was determined to be the primary microstructure constituent, but mostly without the typical aligned second phase, normally seen in more conventional low carbon micro alloyed steel. At high magnifications there seemed to be some fine ferrite grains nucleated. It was also concluded that the microstructure of the ICCGHAZ did not seem to change much compared to the CGHAZ. This is in good agreement with the findings in this thesis.

4.2 Nanoindentation

The automated indentation sequence, described in Section 3.3, was performed successfully using a Berkovich tip. Load-displacement curves were recorded, and the Hysitron software calculated hardness, reduced modulus of elasticity, and contact area. The average value for Young's modulus of elasticity was calculated to be 235.1 ± 10.87 GPa. The procedure for calculating these properties is explained in Section 2.6. The calculations required calibration of the Berkovich tip, by performing several indentations in a material with known properties. The calibration was performed by PhD candidate Tarlan Hadjilou.

Figure 54 shows the hardness results from the indentations presented as a topographic map. The

4 RESULTS AND DISCUSSION

measured hardness from the indentations was placed in a matrix matching the automated grid, and plotted using a mesh plot. This was calculated using MatLab. One of the 49 indentations failed. The hardness value from this point of indentation was excluded, and the average value of the other indentations was used instead. Image analysis uncovered that the failed point was of no special interest when considering the local microstructure, and the average value was therefore determined to be a reasonable value.

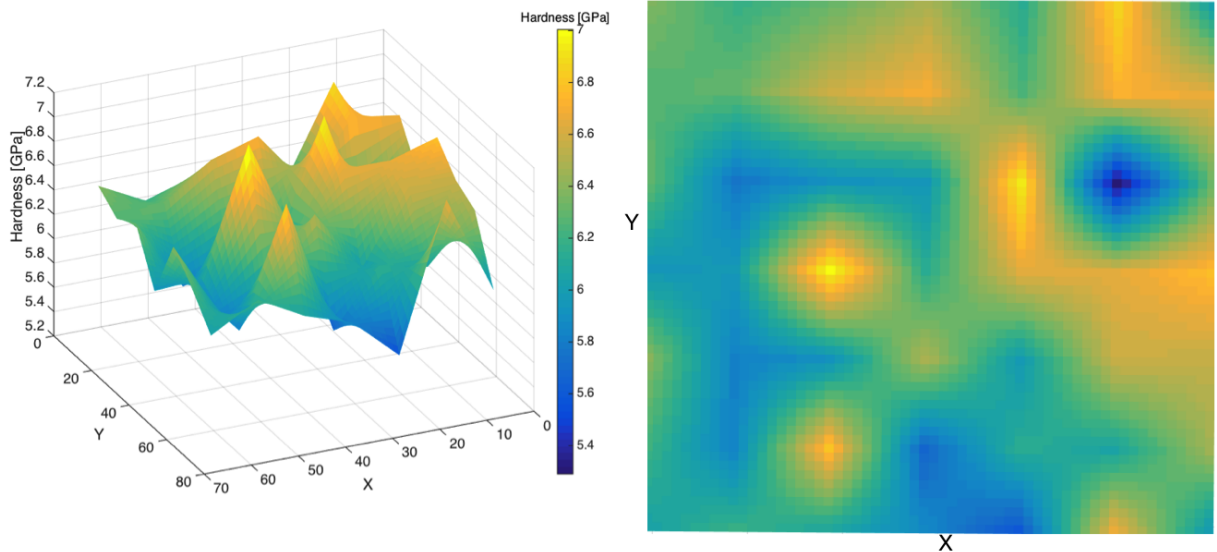


Figure 54: Topographic map of the hardness. 3D-view to the left; top view to the right.

Figure 37 shows that the indentations were performed in the varied region of the microstructure, containing different grain orientations, particles, grain boundaries and phases. This composition of microstructural features yields a measure of the variation of hardness, indicating that this method is a decent tool for material characterization.

The results show a relatively high difference in hardness between the different indentations. The average hardness was 6.26 ± 0.39 GPa, and the maximum and minimum hardness was 7.00 GPa and 5.29 GPa, respectively. The majority of the indentations show a hardness close to average, indicating a consistency in the method. However, local hardness variations in hardness are present, which is a red flag when considering material failure, discussed in Section 2.3. Inspection revealed that the majority of the indentations with high hardness are located on bainite packet boundaries or in the proximity of particles. Some of the indentations on the bainite packets boundaries showed average hardness. The latter two statements imply that MA constituents may have been hit, which is in agreement with the observed presence of MA particles.

4.3 Determination of Young's Modulus of Elasticity

The Young's modulus of elasticity, E , also known as tensile modulus or elastic modulus, is measured using different approaches. The approaches will be outlined, the results presented and compared. The modulus varies with temperature, but the results do not show this trend, thus the temperature dependence of the modulus is neglected [94].

The first approach to obtain the modulus of elasticity is through the procedure of nanoindentation. The theory and procedure is presented in Sections 2.6 and 3.3, respectively. The instrument is designed for the purpose of measuring hardness and the modulus of elasticity. The software of the Hysitron TI-950 TriboIndenter returns the reduced modulus of elasticity, E_r . This can be combined with the modulus of the tip and Equation 34 to calculate the Young's modulus for the steel. Since the load is normal to the surface, and the tip will deform the material equally in all directions, the procedure yields the isotropic modulus of elasticity. Nanoindentation was only conducted for CGHAZ, as explained in Section 3.3. This was determined to 235 ± 11 GPa. This is the value that will be used for the analysis of steel cantilevers in both CGHAZ and ICCGHAZ.

Another approach is briefly discussed in Section 2.4.1. Equation 12, which describes the remaining ligament beneath the crack, can be back solved to yield E . The ligament becomes an input value, which is given by the initial crack depth measured in the SEM and the measured dimensions of the cantilever. Wurster [95] used this approach to obtain data on the Young's modulus for tungsten, which was in agreement with values from the literature. This approach is sensitive to the orientation of the slip systems, which are hard to predict in a bainite steel microstructure.

Using this approach on the pure iron samples yielded the anisotropic modulus of elasticity for the $\{100\}$ orientation; the result was 152 ± 2 GPa, however this is based on results from only two cantilevers because the two others were destroyed by instability of the picoindenter. This is in reasonable agreement with the reported anisotropic modulus of elasticity $E_{100} = 132$ GPa [1]. Because there are so few datapoints the reported modulus is chosen for the analysis of the iron cantilevers.

It is assumed that the chaotic steel microstructure will produce an isotropic modulus of elasticity, because there are not defined orientations within a grain as opposed to pure iron. The measurements vary between 109 – 542 GPa; because of this great scatter it is necessary to use data from all eight cantilevers from both master theses. The idea is that an average of these can give an estimate to the isotropic modulus of elasticity, because the measurements will cover many different orientations. An average of several cantilevers will also reduce the margin of error. This approach resulted in $E = 225 \pm 164$ GPa; the result is in good agreement with the first approach, although the standard deviation is high. This approach is sensitive to the initial crack depth from the SEM, which has proven difficult to determine at magnifications of $\sim 150\,000$ X. One of the best images obtained is presented in Figure 55. Table 9 presents the measured initial crack length, a_0 , the calculated initial ligament, and the measured initial ligament. The relative deviation between the calculated ligament

length and the measured initial ligament length was on average 18.9 %. There are several reasons for the deviation between calculated and measured ligament length. The calculated ligament length is calculated at the first unloading step. Some deformation may have occurred before the first unloading step, causing it to be underestimated. It is also difficult to determine the initial crack length in a SEM, making the measured initial crack lengths inaccurate. In addition, the measured ligament length is calculated using b^* , presented in Equation 13.

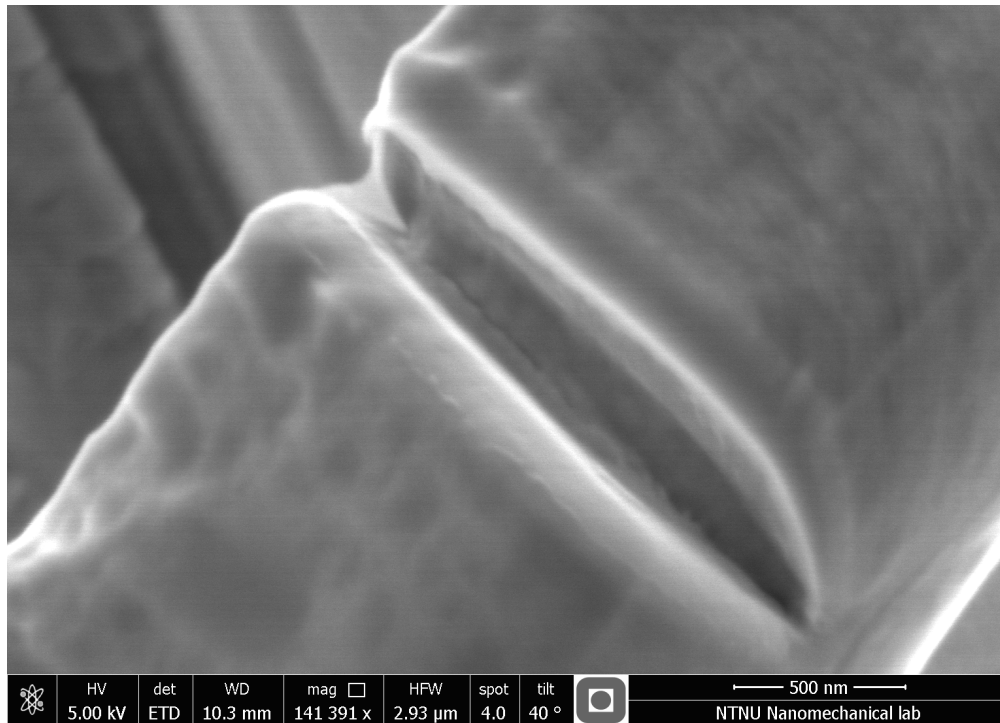


Figure 55: Example of images used to determine the initial notch depth; even the best images are hard to interpret.

The third method for determining the modulus is to use the stress-strain curves produced by compression testing of pillars, as outlined in Section 3.5. This approach yields $E \in [40, 87]$ GPa, which is obviously far too low. The reason for this is that the top diameter of the pillar is used, and the pillar is tapered all the way to the bottom. Also, the elastic deformation in the bulk material below the pillar is not accounted for.

Table 9: Calculated initial ligament, and measured initial ligament, for all cantilevers. The initial crack length of cantilever CGHAZ 2-4 was not possible to estimate by SEM.

Cantilever	Measured a_0 [nm]	Ligament _{unl1} [nm]	Ligament _{SEM} [nm]	Percent off [%]
Pure iron, Fe3	371	1360	1301	4.3
Pure iron, Fe4	394	1350	1191	4.7
CGHAZ, 1-1	511	974	1186	21.8
CGHAZ, 1-2	342	1365	1155	15.4
CGHAZ, 2-3	534	1272	928	27
CGHAZ, 2-4	-	1060	-	-
ICCGHAZ, 2	324	1095	1406	28.4
ICCGHAZ, 3D	373	1150	1082	5.9
ICCGHAZ, 4	198	1152	1482	28.6
ICCGHAZ, 5D	194	1058	1418	34
Average	360	1173	1239	18.9

4.4 Determination of Yield Strength

The determination of the yield strength is not straight forward, and several approaches are used ubiquitously. The exact point at which the material yields, is dependent on the interpretation of the stress-strain curve. The determination of the yield strength for the weld simulated microstructures used in these theses, are based on four pillars from the CGHAZ, and two pillars from ICCGHAZ. When the ICCGHAZ pillars were compressed, two pillars slid off the indenter tip, and one pillar exercised extensive barreling. Therefore, only the completely successful deformation and the barreling pillar form the basis for determining the yield strength for the ICCGHAZ cantilevers. The pillar subject to barreling, yields before extensive barreling occurs, enabling determination of the yield strength. It was decided to use two different values for the yield strength for the two different temperatures; this is due to an increase of the yield strength as the temperature is lowered. This phenomenon is described in B.D. Snartland's specialization project [87]. Since both ICCGHAZ pillars tested at -80°C provided unreliable results, the yield strength for the ICCGHAZ determined at

4 RESULTS AND DISCUSSION

room temperature, will be used at lower temperatures.

The stress-strain curves were evaluated using several different methods, which were later compared. The methods used were:

- Upper and lower yield strength determined from visual inspection of the stress-strain curves.
- Stress at 5%, 3%, 2.5% and 1.5% strain.

The determined values for each pillar are displayed in Table 10. The different methods are illustrated in Figure 56. Other possible methods would be the classical 0.2% offset yield strength, or the first point of deviation from elasticity; these two were not applied.

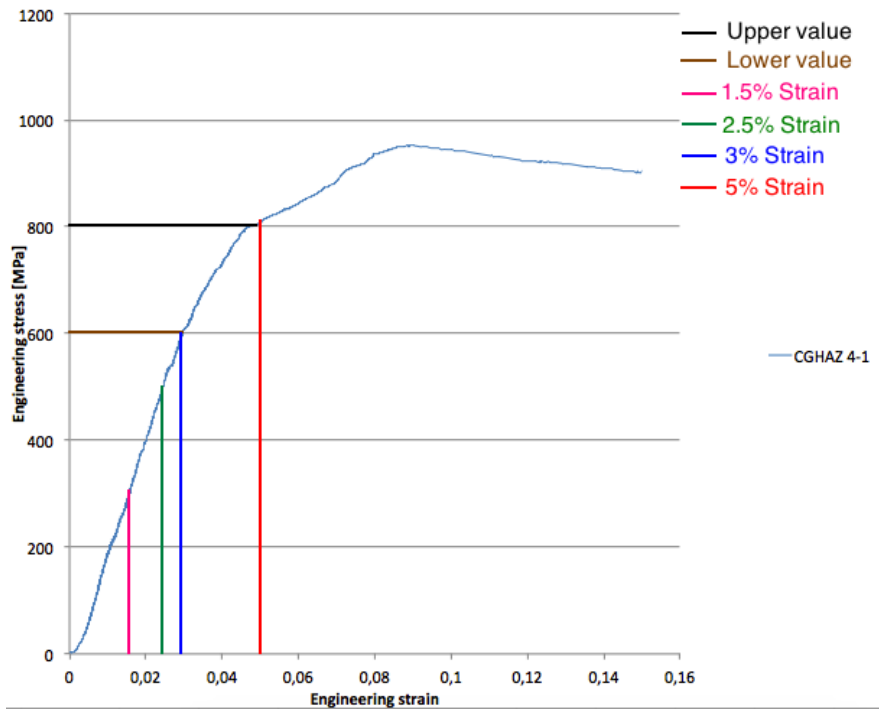


Figure 56: Illustration of the different methods used for determining yield strength.

Average values for the pillars compressed at RT and -78°C were calculated, and each method's reliability was evaluated by visual inspection of the stress-strain curve. None of the applied methods proved reliable for both RT and -78°C . It was therefore decided to use $\sigma_{2.5\%Strain}$ at RT, and $\sigma_{1.5\%Strain}$ at -78°C . $\sigma_{2.5\%Strain}$ and $\sigma_{1.5\%Strain}$ was found to be 548.5 MPa and 589 MPa, respectively for the CGHAZ pillars. These values will be used in the calculations for pure iron and CGHAZ cantilevers. The average $\sigma_{2.5\%Strain}$ for the ICCGAZ was found to be 953.5 MPa, and will be used in the calculations for the ICCGAZ cantilevers.

Table 10: Determined values for the yield strength for each CGHAZ pillar, and the two ICCGAZ pillars.

σ_y	4-1, RT	4-2, RT	6-1, -78 °C	6-2, -78 °C	P10 M-A, RT	P11, RT
$\sigma_{y,Upper}$ [MPa]	800	710	653	680	1274	1000
$\sigma_{y,Lower}$ [MPa]	700	617	525	591	1072	730
$\sigma_{5\%Strain}$ [MPa]	808	763	812	895	1470	1129
$\sigma_{3\%Strain}$ [MPa]	609	666	730	815	1145	1035
$\sigma_{2.5\%Strain}$ [MPa]	514	583	702	776	986	921
$\sigma_{1.5\%Strain}$ [MPa]	283	366	580	598	585	600

4.5 Iron Cantilevers

The pure iron cantilever experiments provided valuable experience through both failure and success. This was, as described in the problem text, done in close cooperation with A.B. Hagen. This section is dedicated to understanding the results from the cantilever experiments. The section also attempts to generalize fundamental principles, trends and mechanisms, to better understand the results from the steel cantilever experiments.

4.5.1 Cantilever Loading

During cantilever loading, the sharp tip may pierce the cantilever surface, affecting the displacement recorded. However, the indentation depth was evaluated after loading experiments and deemed negligible.

Section 3.6 describes the problems encountered when the cantilevers were loaded and the proposed countermeasures. An additional problem with the loading of the cantilevers, was an increasing negative value of the measured force. As the loading sequence was completed, the equilibrium force ended at a negative value, rather than zero. The resulting negative value varied between runs. The loading function was tested several times in vacuum, revealing that the negative values showed some proportionality to the displacement; however, within the run, the correlation was not linear. Because of this non-linear, unpredictable relationship, a complete compensation would require extensive work, and a linear compensation of the negative value was used instead. This compensation tilted the load-displacement curve linearly with the displacement, aligning the curve with the x-axis. This is not a perfect countermeasure, but a definite improvement. The tilting method was discussed with S. Wurster, via e-mail, regarding how it would affect the calculations. Example of a tilt-corrected curve compared to the raw data is presented in Figure 57.

Figure 58 presents the load-displacement curves for the two pure iron cantilevers after tilt correction. Cantilever Fe3 was loaded by several runs at -78°C . Cantilever Fe4 was loaded in a single run at RT. The difference between a single run and multiple runs are described in Section 3.6. Figure 58 shows that Fe4 started deforming at a lower load than Fe3, probably influenced by the difference in sample geometry.

Both cantilevers were plastically deformed, but no brittle fracture occurred. Figure 59 shows an image of a plastically deformed CGHAZ cantilever. The pure iron cantilevers exhibited similar behavior. Both cantilevers displayed a small drop in the measured load as the linear deformation turned plastic. This was also observed by K. Greina in her master thesis [29]. This sudden drop might be caused by the initiation of crack growth, which was observed for both cantilevers, during post-loading SEM examinations. Figures 60 and 61 present images of the cracks of both Fe3 and Fe4. Fe3 shows signs of non-uniform deformation, i.e., uneven crack propagation, while Fe4 shows uniform deformation. The shape of the Fe3 crack indicates crack propagation. Fe4 displays no clear visual signs of crack extension.

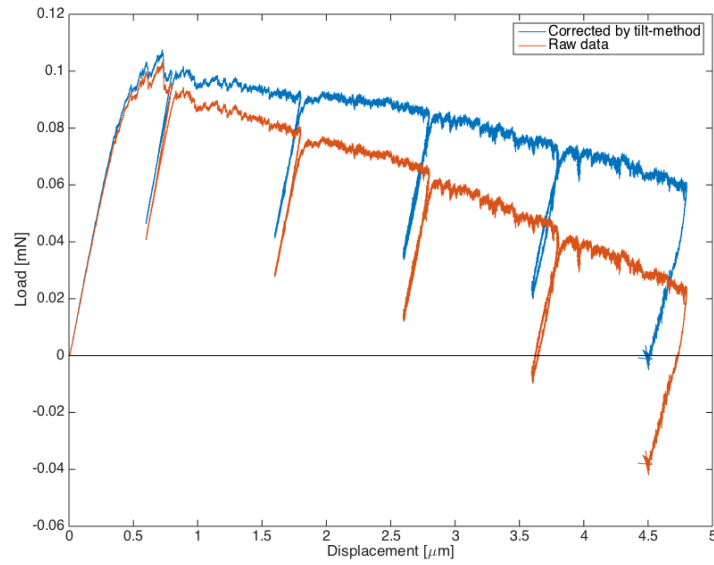


Figure 57: Illustration of how the raw data was tilt-corrected for drift.

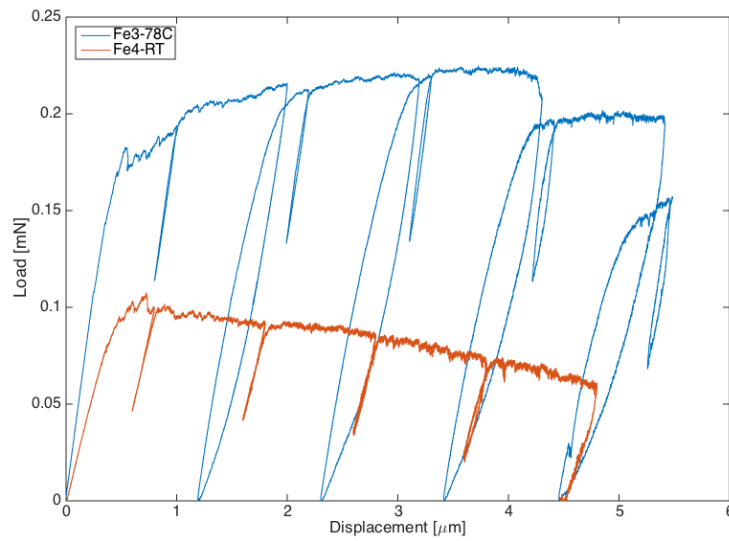


Figure 58: Load-displacement curves for the two pure iron cantilevers.

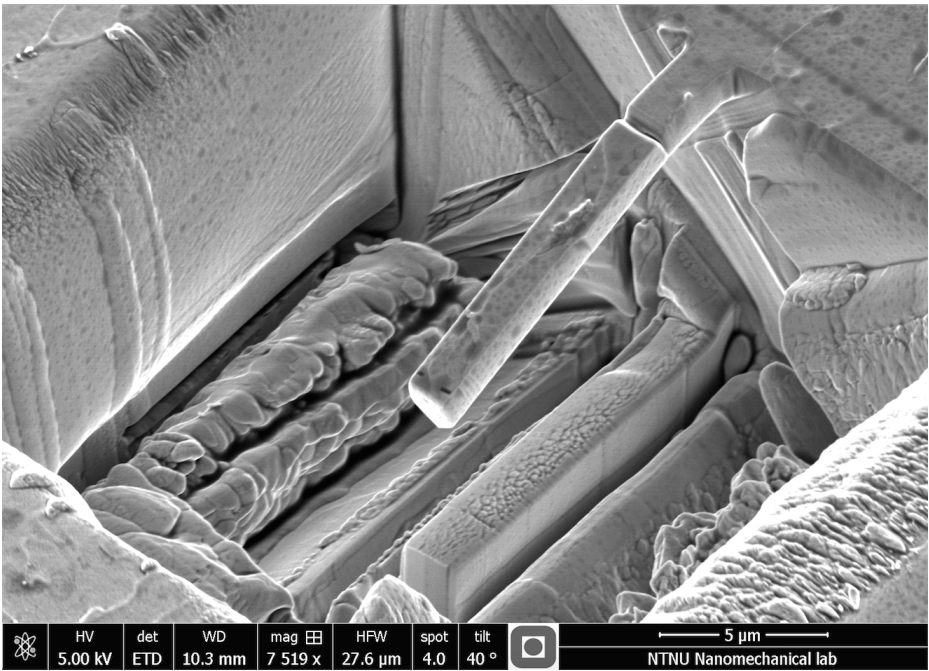


Figure 59: Plastically deformed cantilever.

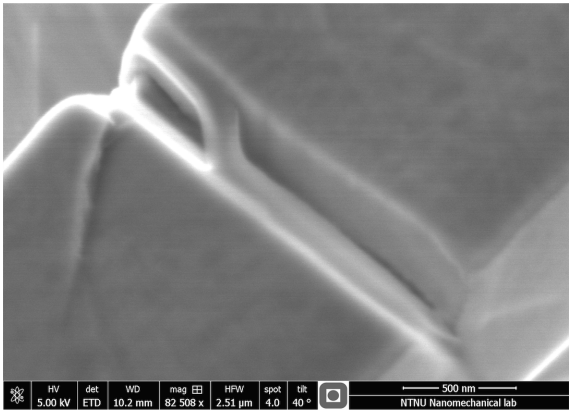


Figure 60: Cantilever Fe3 after loading.

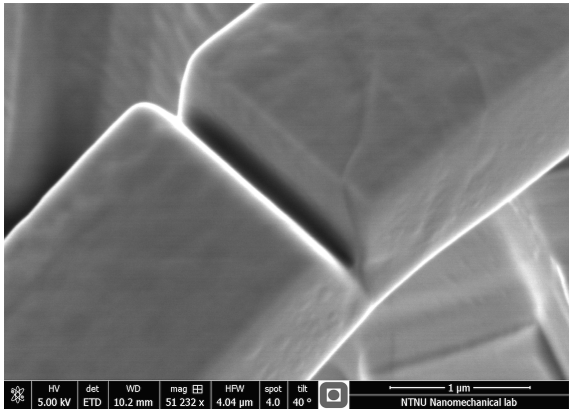


Figure 61: Cantilever Fe4 after loading.

4.5.2 Crack Growth

The crack growth was determined by the change in unloading stiffness of the load-displacement curves. The slope of the linear part of the small unloading sequences, was determined and used in the calculation of remaining cantilever ligament, according to Equation 12. Due to difficulties with determining the initial crack length accurately in a SEM, the initial crack length was set to be equal to the crack depth determined by the ligament from the first unloading. The crack growth was determined by the change in ligament from the first unloading step, assuming that little plastic deformation occurs before the first unloading step.

Figure 62 illustrates the calculated crack growth for cantilever Fe3. The graph was linearly fit in order to emphasize when the change in gradient of the crack growth had occurred. The linear fitting lines intersect between unloading step 2 and 3, indicating a change in type of fracture. This method of determination was proposed by S. Wurster [95], and could be visually verified by the simulation done by M. Jørum [49], further discussed in Section 4.6. The increasing gradient indicates that the crack propagation evolved from blunting of the crack to stable crack growth. This change in fracture behavior will deviate between micro and macro samples. Small samples have much less volume that can store elastic energy. As the cantilever is deformed, this stored energy will be released. When the amount of released energy is low, the crack growth will become stable. Large samples store much more elastic energy, inducing unstable crack growth as the energy is released. Figure 63 shows the calculated crack growth at each unloading step for both pure iron cantilevers.

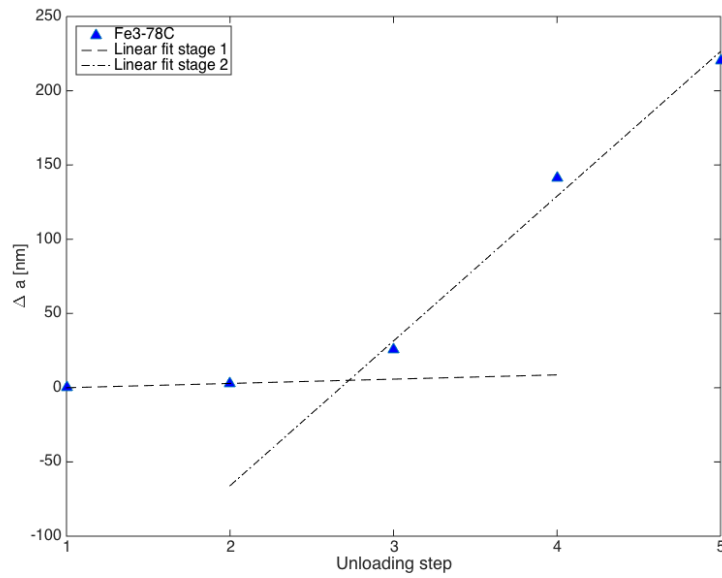


Figure 62: Calculated crack growth for cantilever Fe3 with linear fitting, indicating a change in the slope of the crack growth.

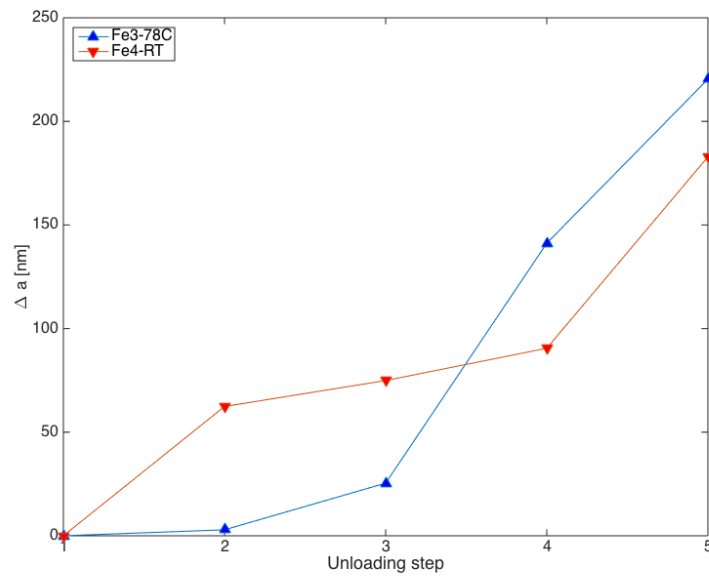


Figure 63: Calculated crack growth for cantilevers Fe3 and Fe4.

4.5.3 J-Integral

The J-integral is calculated using Equation 27. $J_{(i)}$ is calculated for each unloading step. The critical unloading step is determined from Figure 63, which is then used to evaluate the J-curve to obtain the critical J-value. This is the first step where stable crack growth took place. The critical unloading step for Fe3 and Fe4 was set to be unloading step 2 and 3, respectively.

The $J - \Delta a$ curves for both pure iron cantilevers are presented in Figure 64. The purpose of determining critical J-values is to calculate the critical stress intensity factor. It can be observed from Figure 64 that Fe3 shows significantly higher values for $J_{(i)}$ than Fe4. This can be recognized as a higher energy requirement in order to further propagate the crack, or that cantilever Fe3 displays a higher fracture toughness than Fe4. J-values calculated by the approach used by Di Maio will not be presented in this section, since the calculated results are remarkably similar to the approach proposed by Wurster.

4.5.4 Crack Tip Opening Displacement

With the experimental set-up in this thesis, direct measurement of the CTOD was difficult, due to the fixed sample position, working distance and quality of the live SEM images. It was therefore decided to calculate critical $CTOD_{Q,(i)}$ -values from $J_{(i)}$, using Equation 32. SEM images of the cantilevers before and after loading enabled measurements of CMOD. The measured values for CMOD were used to calculate the CTOD, by the Hinge model, after the final unloading step. The Hinge model is described in Section 2.5.2.

Figure 65 presents the calculated $CTOD - \Delta a$ curves for both pure iron cantilevers, along with the final CTOD-value calculated from the measured CMOD-values. The CTOD-values calculated from the measured CMOD, deviate from CTOD-values calculated from $J_{(i)}$, due to difficulties with measuring the exact CMOD. However, the deviation between the CTOD-values at the final step for cantilever Fe4, is only ~ 100 nm. This indicates that the calculated CTOD values from $J_{(i)}$ are reasonable, despite the assumptions and simplifications made.

$K_{Q,CTOD}$ could be calculated from the CTOD values. Since this calculation is based entirely on the calculation of the J-integral, the calculated values for $K_{Q,J}$ and $K_{Q,CTOD}$ would be equal.

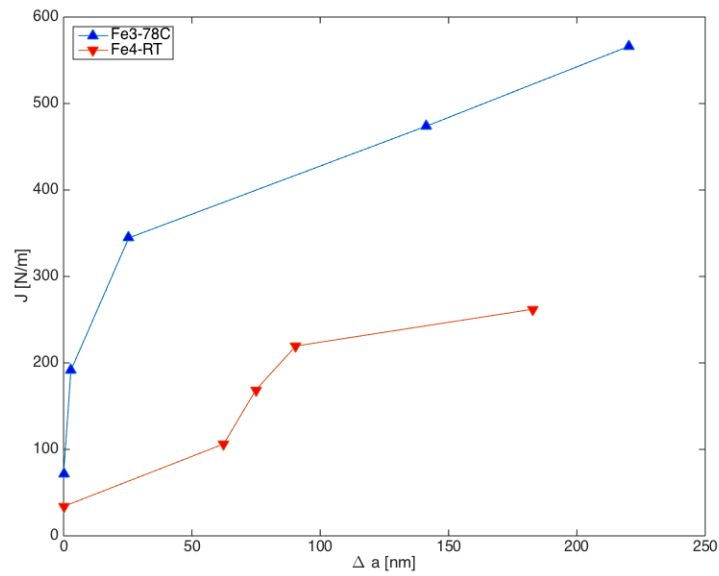


Figure 64: Calculated J- Δa curves for both pure iron cantilevers.

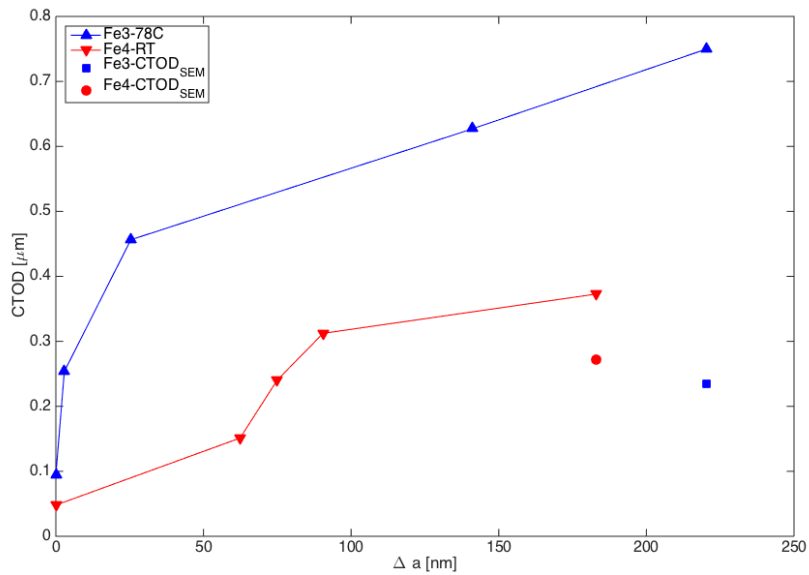


Figure 65: Calculated CTOD- Δa curves for both pure iron cantilevers, along with the final CTOD value calculated from the measured CMOD values.

4.5.5 Stress Intensity Factor

The preliminary stress intensity factor, K_Q , is frequently used as a fracture toughness parameter when all the requirements for K_{IC} are not met. Determination of the real critical stress intensity factors, K_{IC} , is not possible due to the small sample size; thus, K_Q values are given. The stress intensity factor describes the stress intensity required to propagate a crack. The critical K_Q -values are calculated by Equations 11, 15 and 28. Equation 11 is used to calculate $K_{Q,LEFM}$ based on the shape factor used by Wurster [95], while Equation 15 is calculates $K_{Q,LEFM}$ based on the approach proposed by Di Maio [64]. The $K_{Q,LEFM}$ -values are used in the calculation of the J-values, which are used to calculate $K_{Q,J}$.

Figure 66 presents the calculated critical values of K for both pure iron cantilevers. $K_{Q,LEFM}$ - and $K_{Q,J}$ -values calculated by the approach presented by Wurster and Di Maio are compared. The presented values of K are corresponding to the critical values of J , as discussed in Section 4.5.3. Figure 66 shows that the values of K calculated by the Di Maio approach are slightly higher than the ones calculated through the Wurster approach. The fundamental difference between the two methods is the shape factor used, and Di Maio's assumption of only small deformations. The calculations with the shape factor proposed by Wurster uses a square cross section, which is implemented on the cantilevers by Equation 13. This approach may also affect the difference in calculated critical K-values. Figure 66 also shows that cantilever Fe3 has higher calculated critical K-values. This is in line with the literature, due to the restricted movement of screw dislocations at lower temperatures. The calculated values of $K_{Q,LEFM}$ are not delivering correct fracture toughness values; they are merely representing a lower limit. The large difference between $K_{Q,LEFM}$ and $K_{Q,J}$ is probably caused by the size of the specimens used in this thesis. The calculated critical fracture toughness values serve as a good approximation to the deviation from elastic behavior, which indicate a massive emission of dislocations. The FIB-machined notch is far from atomistically sharp and the relatively blunt notch will increase the calculated K -values.

No brittle fracture occurred; it is believed that this is caused by the specimen size. The size of the plastic zone ahead of the crack tip could exceed the size of the cantilever, making brittle fracture impossible. A large plastic zone, relative to the cantilever ligament, will cause yielding instead of fracture, which again will make the calculated results somewhat inaccurate.

K. Greina loaded pure iron cantilevers in her master thesis [29], and A.L.L. Kvaal in his specialization project [53]. Greina and Kvaal used the same cryogenic set-up as in this thesis, but without cooling of the indenter tip. K. Greina loaded two cantilevers at room temperature, and six cantilevers at temperatures below -70°C . Greina and Kvaal calculated $K_{Q,LEFM}$ to be between $2.9 - 8.9 \text{ MPa}\sqrt{\text{m}}$ at room temperature. These values deviate by a factor of 2-4 from the calculated values in this thesis. The reason for the large deviation is that they had the same difficulties measuring the CTOD during loading, forcing the use of post-loading CTOD. This means that K_Q -values calculated in their theses are arbitrary K_Q -values at a certain displacement, i.e., not at the initiation

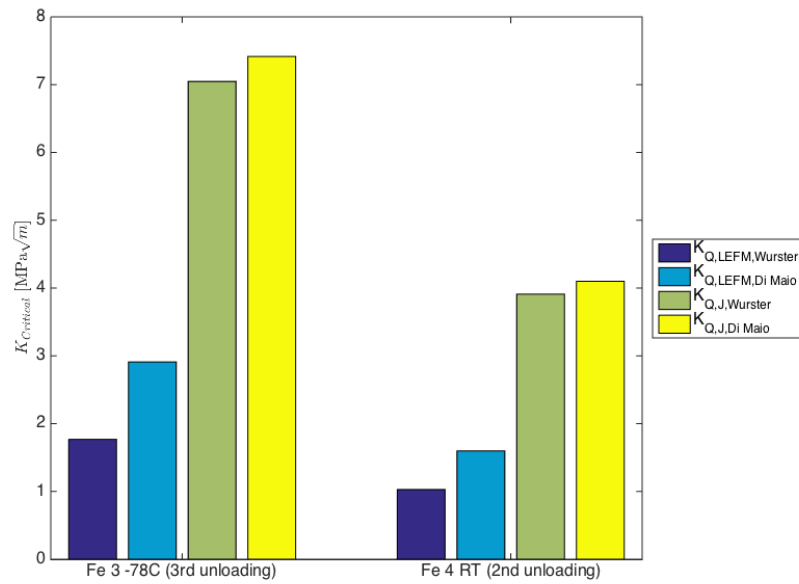


Figure 66: Calculated critical K-values for both pure iron cantilevers.

of stable crack propagation. Comparing these results adds no value or insight to the problem at hand. This was the motivation for the introduction of the unloading stiffness method.

4.6 Experiments and Atomistic Modeling

M. Jørum has been modeling pure iron cantilevers atomistically at room temperature [49], and B.D. Snartland and A.L.L. Kvaal have been loading pure iron cantilevers. This section is dedicated to identifying possible correlations between practical experiments and atomistic modeling. The cantilevers are pentagonal, calculations have been executed based on the same assumptions using the same methods. Detailed theory related to atomistic modeling and fracture mechanics is described in Jørum's master thesis [49], and theory related to material behaviour and fracture mechanics is described in Snartland's and Kvaal's master theses [88][54].

Figure 67 shows the calculated, or measured, crack growth for both pure iron cantilevers and the modeled cantilever. The simulated cantilever is related to the secondary y-axis, on the right hand-side. There is a clear correlation in crack behavior for the cantilevers. All cantilevers exhibit slow crack growth after the initial unloading steps, before accelerating at the later unloading steps. Note that the modeled cantilever does not unload, and the measuring steps are chosen according to simulation time steps.

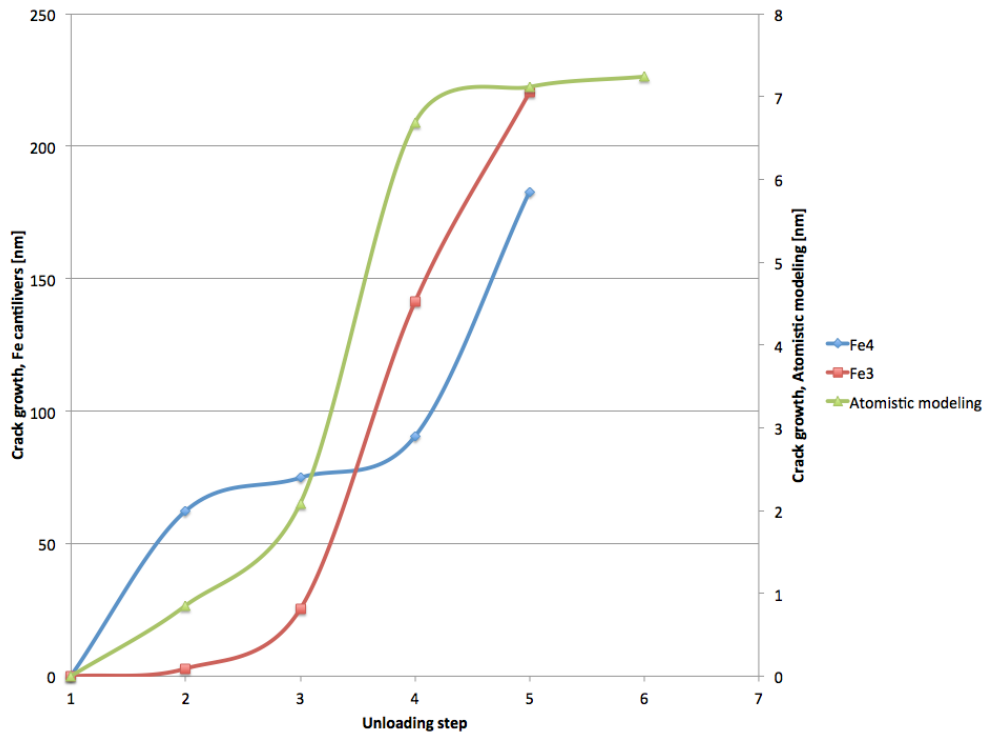


Figure 67: Calculated crack growth for pure iron cantilevers Fe3 and Fe4, and an atomistically modeled cantilever.

4 RESULTS AND DISCUSSION

Figure 68 shows J- Δa curves for the atomistically modeled cantilever and both pure iron cantilevers. Both pure iron cantilevers have higher J-values than the simulated cantilever, meaning that the modeled cantilever is less tough than the pure iron cantilevers. A possible explanation is the difference in loading rate, which is significantly larger for the atomistic model. The modeled notch is atomistically sharp, while the machined notches are blunt. A sharp tip requires much less energy to propagate a crack compared to a blunt tip.

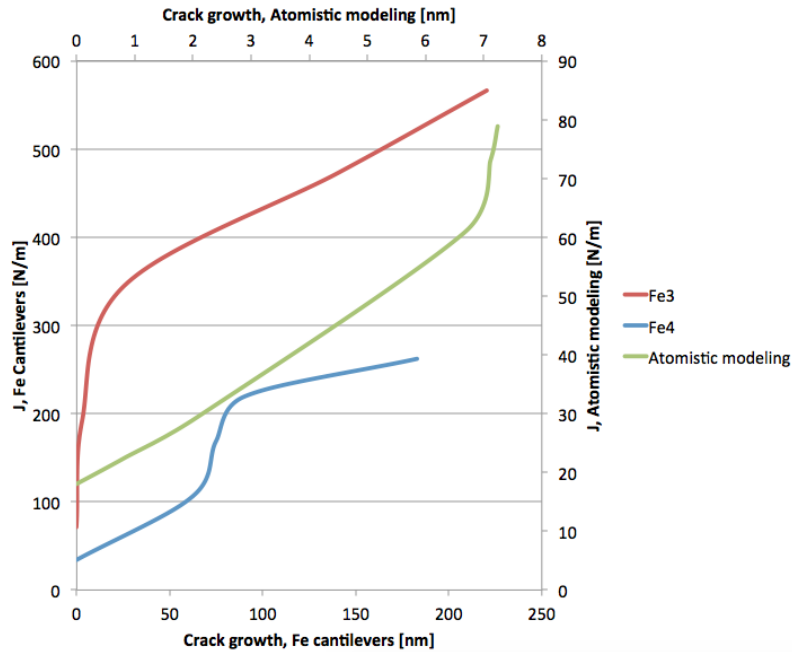


Figure 68: Calculated J- Δa curves for both pure iron cantilevers and an atomistically modeled cantilever.

Figure 69 shows the critical stress intensity factors for the different cantilevers. The K-values are lower for the modeled cantilever than the physical cantilevers. This was expected due to the differences in the calculated J-values, already, and is also attributed to the differences in loading rate and notch geometry.

The real cantilevers and the modeled cantilever displayed similar deformation behavior. However, notch geometry, loading rate, and specimen size, influence the quantitative data obtained. The loading rate is significantly different; the machined cantilevers are loaded in the order of $\frac{\mu\text{m}}{\text{min}}$, while the modeled beams are loaded in the order of $\frac{\text{m}}{\text{s}}$. The different notch geometries are strongly affecting the fracture properties of the cantilevers, which is in accordance with the literature [16][65]. The size is typically differing by 1 order of magnitude. Another aspect to consider is that the modeled material is defect-free, whereas the pure iron contains several types of defects; these affect the material properties and the fracture behavior.

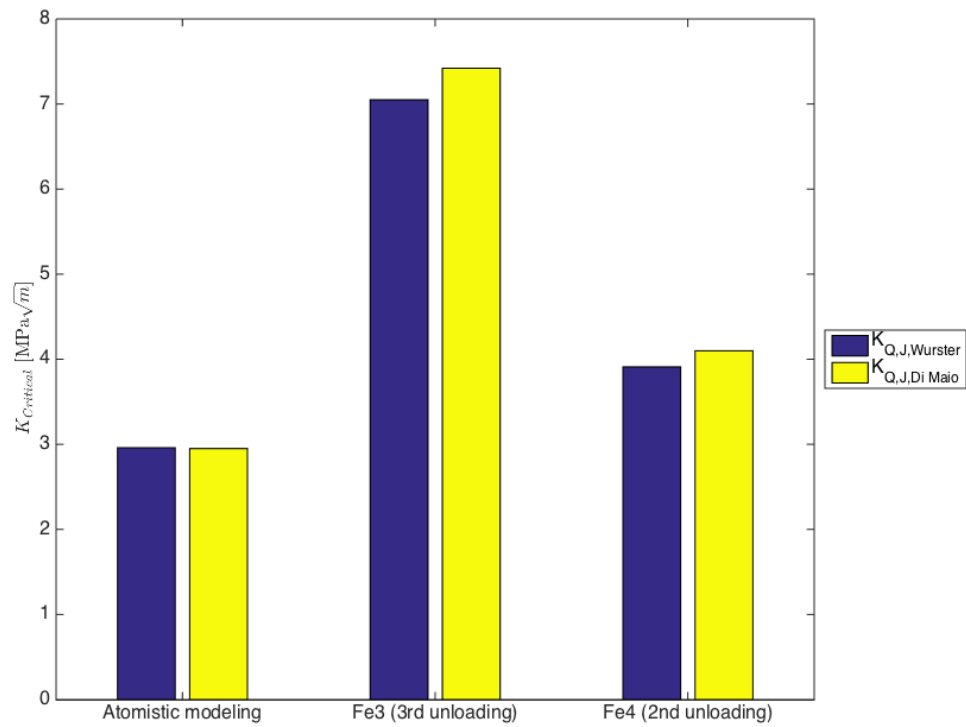


Figure 69: Calculated critical K-values for both pure iron cantilevers and an atomistically modeled cantilever.

4.7 CGHAZ Cantilevers

This section will present the results of CGHAZ cantilever experiments, and compare them with the pure iron cantilevers. Most phenomena and explanations of calculated results are already covered in Section 4.5. Recurring results and phenomena will therefore not be covered in this section. Cantilevers 1-1 and 1-2 were located within the same austenite grain, but at two different bainite packets. Cantilevers 2-3 and 2-4 were placed the same way. Any trends will not be considered due to a relatively low number of samples.

4.7.1 Cantilever Loading

Two cantilevers were loaded at room temperature, one was loaded at -76°C , and one was loaded at -77°C . Brittle fracture was not observed under any conditions. Figure 70 presents the load-displacement curves for all four CGHAZ cantilevers. All cantilevers were loaded repeatedly with the shortened displacement controlled loading function, presented in Figure 46, and combined to on long loading function. The final loading steps of cantilevers 1-2 and 2-3 are somewhat rugged. This effect is likely caused by indenter sliding, as the displacement is high, decreasing the contact angle between the cantilever and the indenter. The sliding may affect the reliability of the calculations at the final steps. Cantilevers 1-1 and 2-4 show tendencies to pop-in as plastic deformation is initiated, described in Section 4.5.1.

4.7.2 Crack Growth

All four CGHAZ cantilevers experienced crack growth. The calculated crack growth curves for all cantilevers are presented in Figure 71. Cantilever 1-2, which was loaded at -77°C experienced heavy crack growth. SEM measurements after loading revealed that the crack propagated approximately 470 nm, which is slightly higher than the calculated value of approximately 410 nm. The crack after loading is presented in Figure 72, and the same crack with measurements is presented in Figure 73. This indicates that the calculated results are somewhat reliable.

The other three cantilevers show less crack growth, even less than the pure iron cantilevers. The pure iron cantilevers have an average crack growth of approximately 200 nm, while cantilevers 1-1, 2-3 and 2-4 have an average of approximately 95 nm. The three mentioned cantilevers also exhibit steady crack growth compared to the pure iron cantilevers, and CGHAZ cantilever 1-2. This might be caused by differences in notch geometry, or lath boundaries inside the cantilevers halting the crack propagation.

Cantilevers 1-2 and 2-3 exhibit similar trends when comparing with Wurster [95]: slight crack growth which represents blunting, before stable crack growth is initiated. This trend is also present for the pure iron cantilevers. Cantilever 1-1 exhibits stable crack growth throughout the loading,

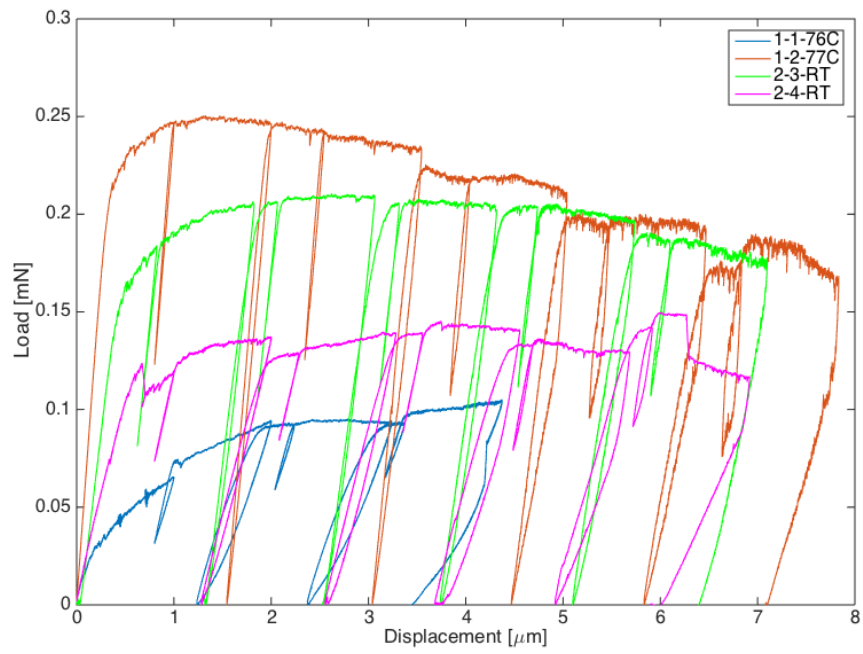


Figure 70: Load-displacement curves for all CGHAZ cantilevers.

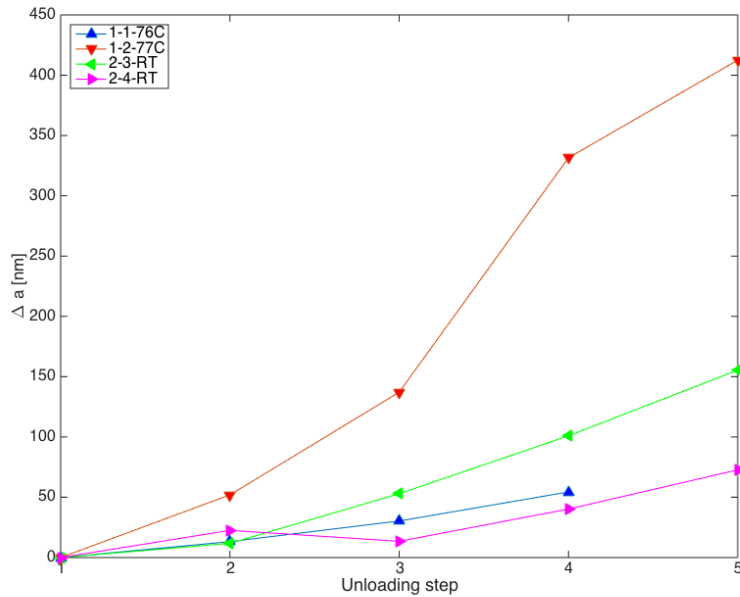


Figure 71: Calculated crack growth curves curves for all CGHAZ cantilevers.

indicating that no blunting occurred. The determined critical unloading steps for all cantilevers are presented in Table 11.

Another observation made, is that the calculated crack growth on unloading step 3 on cantilever 2-4 is negative. This is due to an increased measured unloading stiffness. Negative crack growth, which is not a particularly rare phenomenon, has no clear countermeasure. It is believed that it is caused by either friction, misalignment, balancing, zeroing of electronic equipment, physical blunting of the notch, or compressive residual stresses in the plastic zone [80], which may occur around the crack tip when obtaining the unloading stiffness. This will cause an increased measurement of the unloading stiffness, causing the calculated crack growth to be negative.

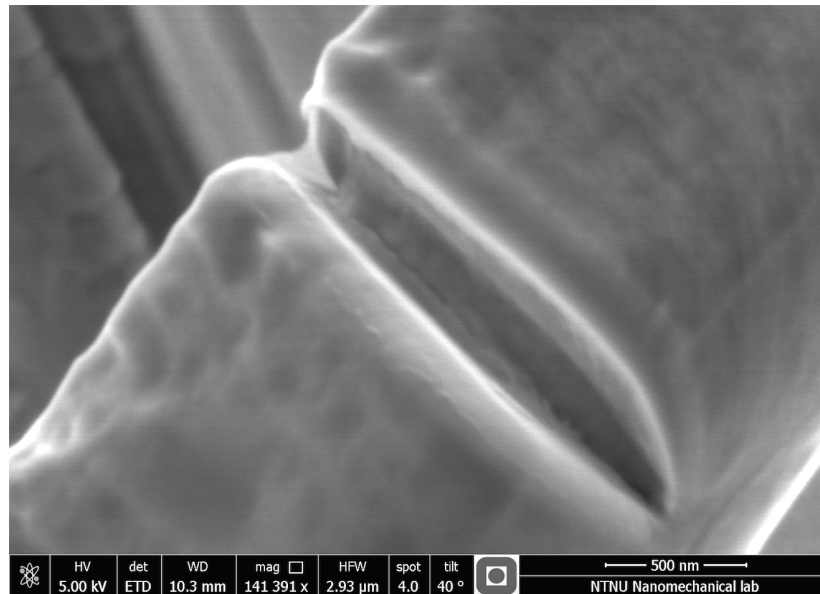


Figure 72: SEM image of the cantilever 1-2 crack after loading.

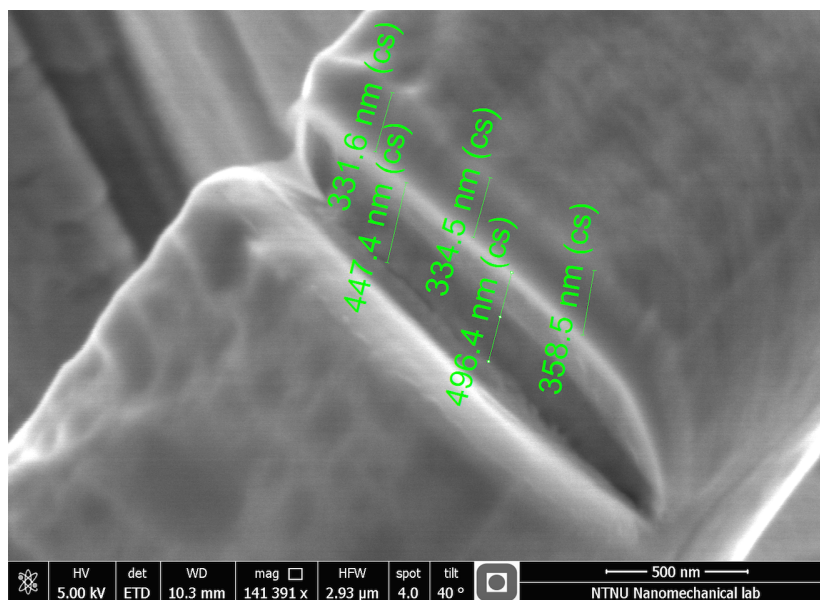


Figure 73: SEM image of the cantilever 1-2 crack, with measurements, after loading.

4.7.3 J-Integral

The J-integral was calculated for all four CGHAZ cantilevers, and critical J-values were determined. The evaluation of stable crack growth initiation was determined from Figure 71. The calculated J-values after each unloading step are presented in Figure 74. The calculated J-values are higher than the values calculated for pure iron. The J- Δa curves for the CGHAZ cantilevers show limited scattering in the initial region, which indicates similar initial deformation behaviour. The shape of the calculated J- Δa curves are comparable to the curves presented by Wurster. The J- Δa curve for cantilever 2-4 shows clear deviance due to the calculated negative crack growth discussed in Section 4.7.2. The determined critical unloading steps for each CGHAZ cantilever, and the critical J-values, are presented in Table 11.

Table 11: Critical unloading step for all four CGHAZ cantilevers.

	1-1, -76 °C	1-2, -77 °C	2-3, RT	2-4, RT
Critical unloading step	2	2	3	2
Critical J-values [N/m]	164.7	357.8	378.2	256.7

4.7.4 Crack Tip Opening Displacement

Critical $CTOD_{Q,(i)}$ -values were calculated for all CGHAZ cantilevers, using $J_{(i)}$. CTOD for the last unloading step was also calculated from CMOD-values measured in a SEM. The CTOD- Δa curves for all CGHAZ cantilevers are presented in Figure 75. It is clear that the steel cantilevers show greater CTOD than the pure iron cantilevers. The CGHAZ cantilevers show a calculated average CTOD of approximately 1 μm , while the pure iron cantilevers show approximately 0.6 μm . The cause for this is probably differences in notch geometry, due to variations in milling rates during notch machining. The SEM measured CTOD values are deviating from the calculated values. There are several assumptions made in the calculations, and a hard-to-define crack mouth in the SEM hampers the accuracy of the measured CMOD. However, there is a clear correlation between the arrangement of calculated CTOD from $J_{(end)}$ and the measurements. This indicates that the model is ultimately working, even though deviation between the two methods is present. Figure 76 shows the measurement of the CMOD after the final unloading step on cantilever 1-1.

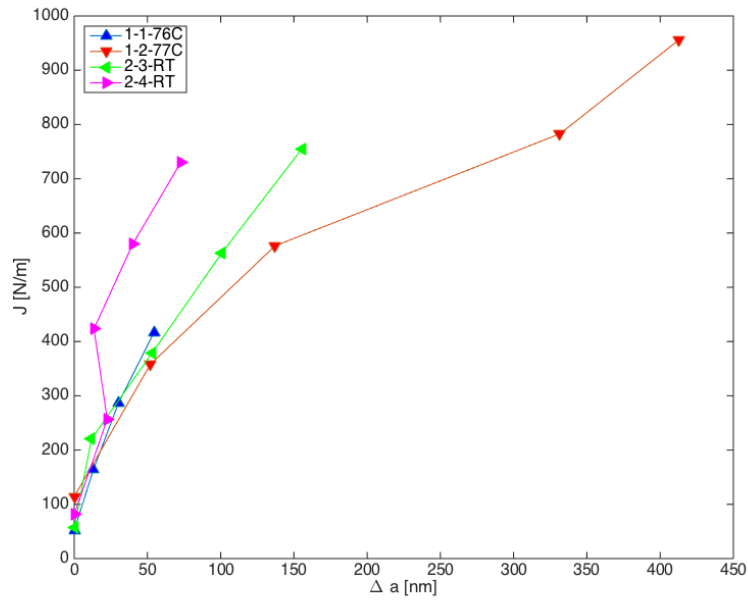


Figure 74: J- Δa curves for all CGHAZ cantilevers.

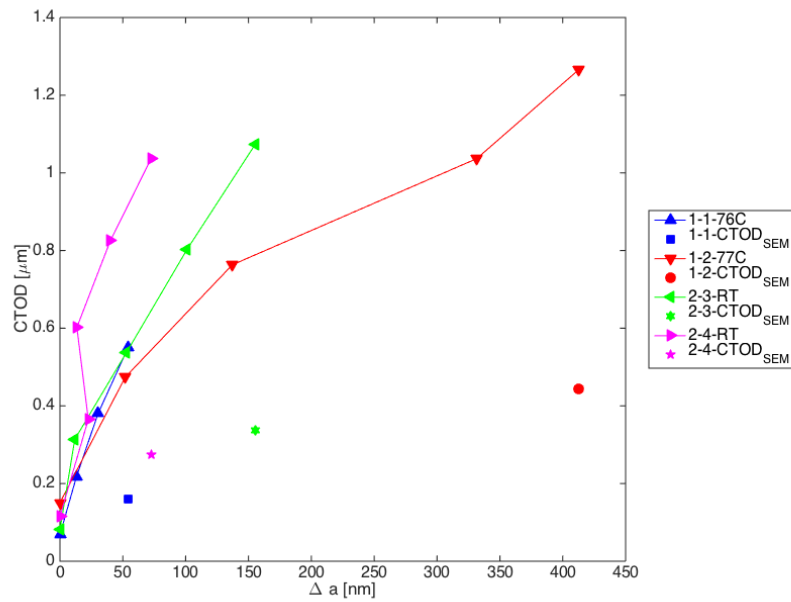


Figure 75: CTOD- Δa curves for all CGHAZ cantilevers.

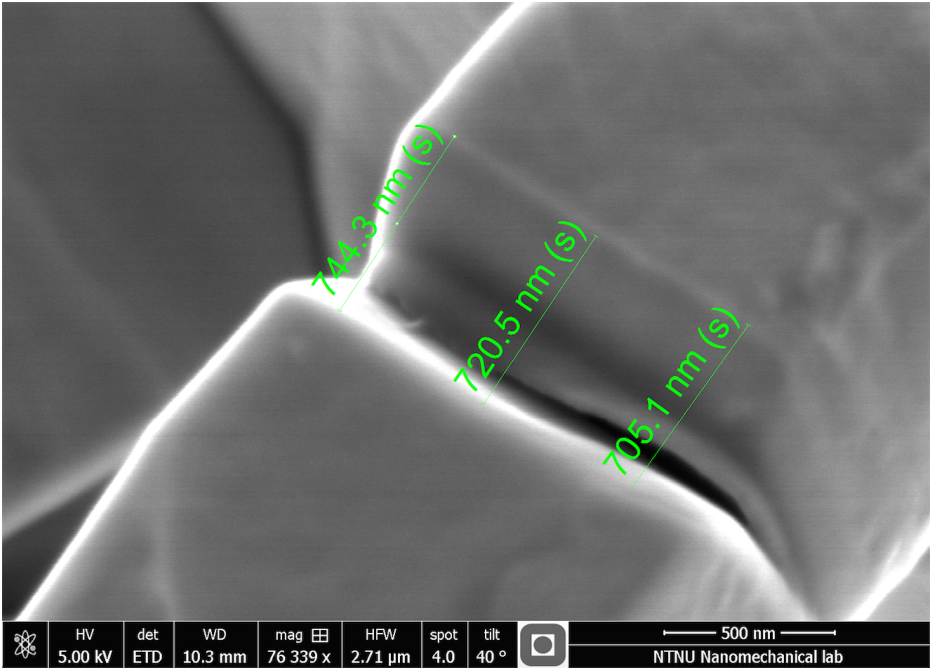


Figure 76: CMOD measurement after the final unloading step on cantilever 1-1.

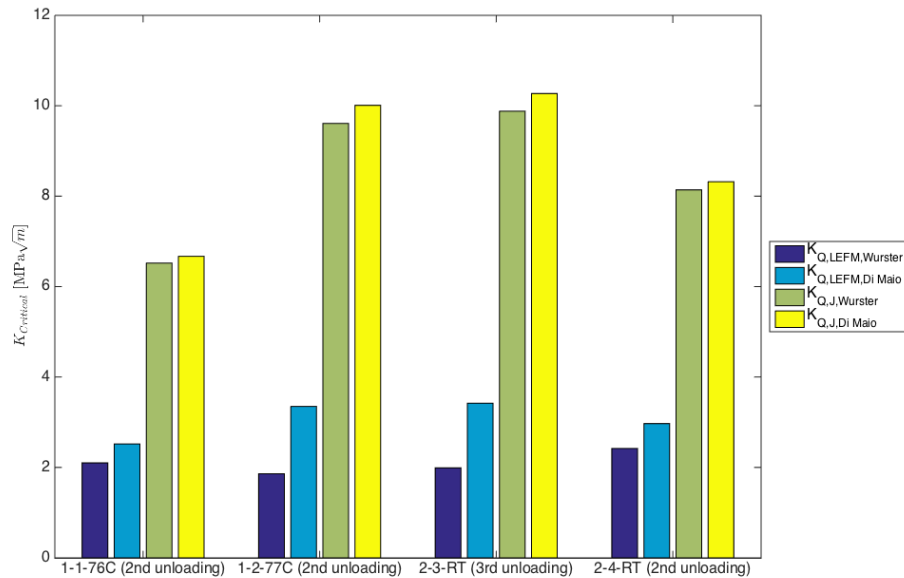


Figure 77: Critical K-values for all CGHAZ cantilevers.

4.7.5 Stress Intensity Factor

The preliminary stress intensity factors were calculated for all CGHAZ cantilevers, using the same method described in Section 4.5.5. Figure 77 shows the calculated critical K-values for all four cantilevers. The K-values are relatively even for the different cantilevers, and at different temperatures. The literature states that the cantilevers loaded at lower temperatures should exercise higher resistance to crack propagation. The relatively low number of cantilevers does not enable statistical grounds to consider if the K-values actually are deviating from the literature. The critical $K_{Q,J}$ values range from 8.14 MPa√m to 9.88 MPa√m at room temperature, and from 6.52 MPa√m to 9.61 MPa√m at reduced temperatures. The critical stress intensity factors for the CGHAZ cantilevers yield an average value of approximately 8.6 MPa√m, while the pure iron samples average on approximately 5.5 MPa√m, over both temperature regimes. This indicates that the steel cantilevers exercise a higher resistance to crack growth than the pure iron cantilevers.

4.8 CGHAZ Pillars

Four CGHAZ pillars were compressed at RT and at -78°C . The pillars were machined from four different bainite packets, all within two austenite grains. The stress-strain curves obtained through the compression tests rendered the yield strength, σ_y , used in the cantilever calculations. Descriptions and calculations are presented in Section 4.4. Figure 78 shows the calculated stress-strain curves for all four CGHAZ pillars. The calculations necessary in order to convert load-displacement curves to stress-strain curves are presented in Section 2.7. All four pillars were successfully compressed, yielding at 45° . Figures 79, 80, 81 and 82 show images of the pillars after compression. All four pillars yielded at relatively equal stresses, but with a noticeable difference in the modulus of elasticity between the pillars compressed at room temperature and -78°C . This is, however, in consistent with the literature.

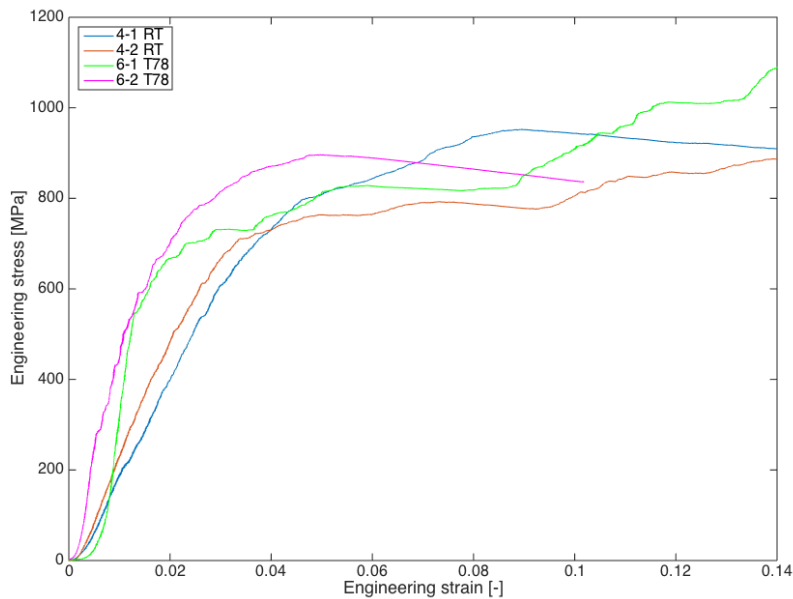


Figure 78: Stress-strain curves for CGHAZ pillars.

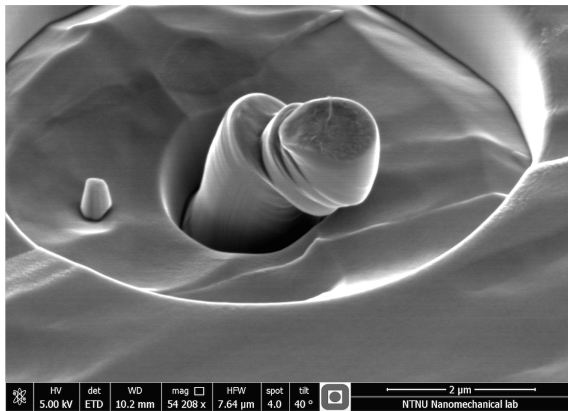


Figure 79: Pillar 4-1 after compression.

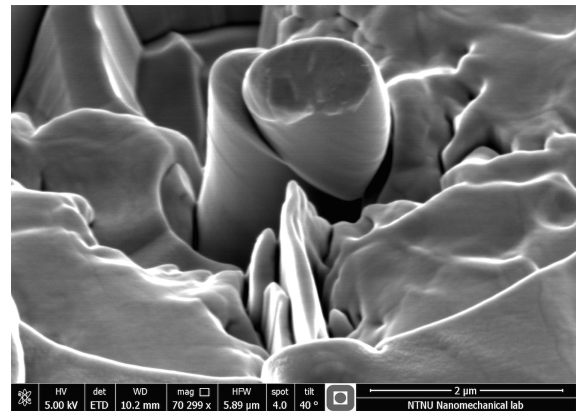


Figure 80: Pillar 4-2 after compression.

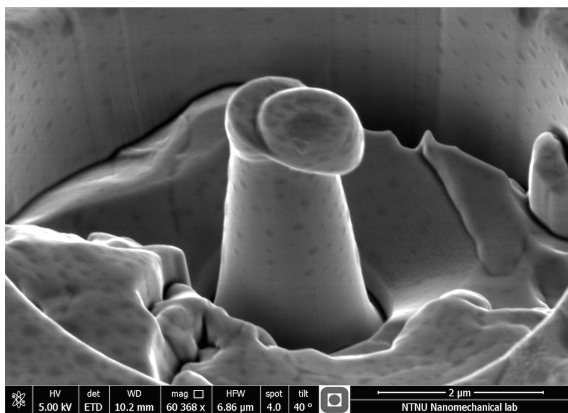


Figure 81: Pillar 6-1 after compression.

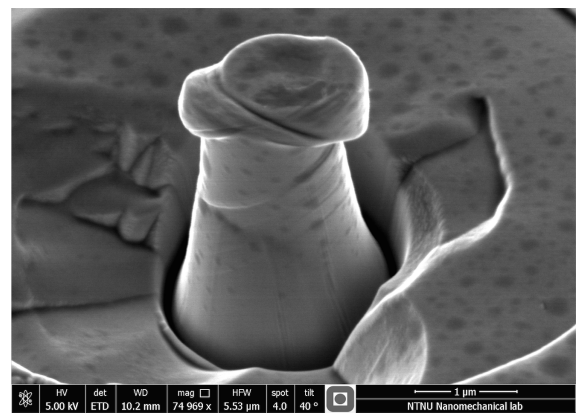


Figure 82: Pillar 6-2 after compression.

4.9 Pure iron, CGHAZ and ICCGHAZ cantilevers

In this section, all cantilevers associated with this thesis are plotted for comparison and evaluation. The CTOD- Δa curves calculated through the J-integral, based on unloading stiffness, are plotted in Figure 83. The cantilevers with the most severe negative crack growth behavior are excluded for the sake of discussing trends between the two different weld simulations. Iron is used to provide reference values. The preliminary critical values, $K_{Q,Wurster}$, are compared in Figure 84. Comparing the trends of the CGHAZ cantilevers in red with the ICCGHAZ cantilevers in blue:

- The ICCGHAZ cantilevers show a flatter curve than the CGHAZ, indicating less resistance to further crack growth once crack propagation has initiated, i.e. a lower fracture toughness.
- As the CGHAZ cantilevers on average display higher CTOD-values, more energy is used to blunt the crack tip per produced area, Δa .
- The CGHAZ cantilevers show on average a slightly lower K_{crit} -value, indicating that this structure might be more prone to stable crack growth initiation.

From these statements one can deduce that while ICCGHAZ shows less resistance to further crack growth, it does not seem as a more favorable initiation site. As presented in Section 4.1.1, the screening by SINTEF found low toughness values for ICCGHAZ, which is not in agreement with the trends for fracture toughness in Figure 83. With respect to the ICCGHAZ, these experiments only attempted to investigate the debonding mechanism and brittle cracking of the ICCGHAZ particles. These mechanisms are discussed in Section 2.1.4, and they lay a foundation for the MBM, presented in Section 2.3.8. These result may suggest that the third mechanism, which is related to stress fields generated by transformation induced residual stresses may be the main contributor to reduction of fracture toughness.

There are very few test specimens in parallel which makes the sources of error hard to anticipate. The yield strength is determined in Section 4.4 and is crucial for the calculation from J-integral to CTOD, according to Equation 32. The fact that a higher yield strength was determined for the ICCGHAZ results in a lower CTOD value for ICCGHAZ than CGHAZ.

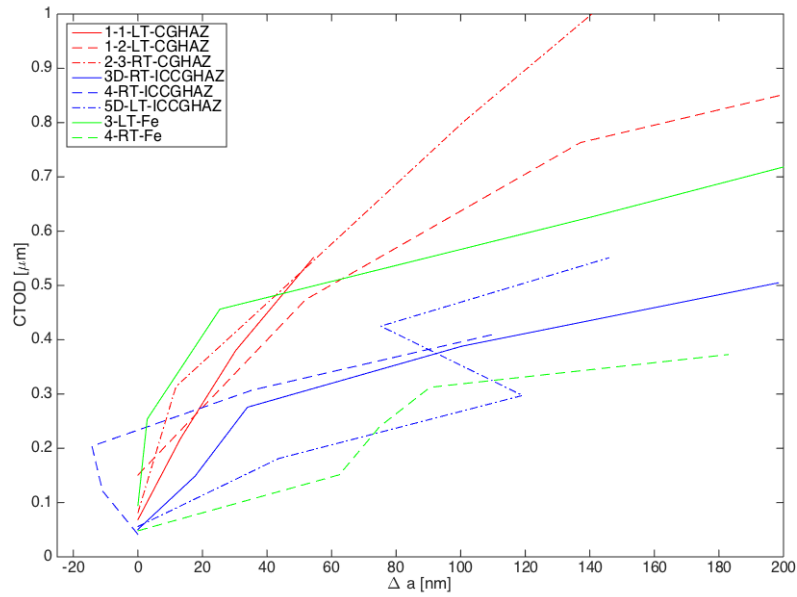


Figure 83: CTOD calculated from J-integral for all cantilevers associated with this thesis.

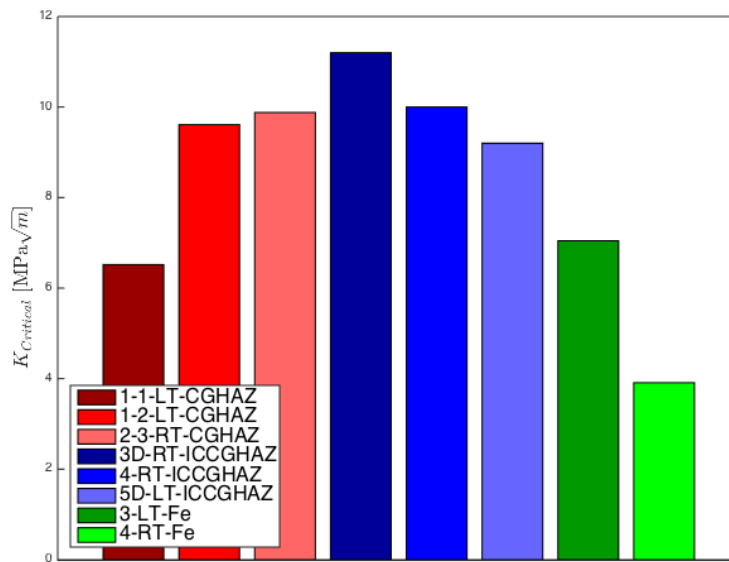


Figure 84: CTOD calculated from J-integral for all cantilevers associated with this thesis.

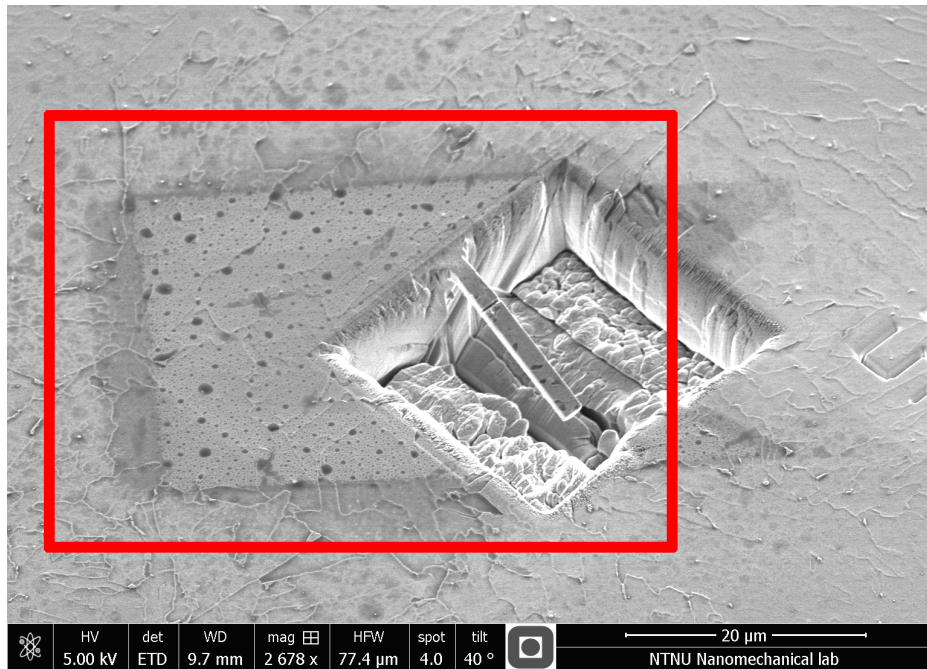


Figure 85: Illustration of suspected oxidation reaction between Fe-Ga surface alloy and air.

4.10 Gallium implantation

As described in Section 2.8, the FIB can implant a structurally significant amount of Ga atoms into the specimen while machining cantilevers and pillars. Measuring this amount is beyond the scope of this thesis, and predicting the effect it has on the fracture mechanics is difficult and requires extensive research on the field. The measurements of the modulus of elasticity, outlined in Section 4.3, yield relatively good results that comply with values reported in the literature, which indicates that implantation of Gallium atoms does not affect the bulk material, but merely just the surface.

There is a clear visual effect of the Fe-Ga alloy produced on the surface, as there is some kind of oxidation process upon reaction with air that leaves marks that are much more distinct in areas subject to extensive milling and irradiation at higher currents. This effect is intriguing because in the literature Fe-Ga alloys are reported to have decent corrosion resistance [47]. The effect is documented in Figure 85.

5 Conclusion

Fracture experiments using notched micro-sized cantilevers have been performed at different temperatures. The samples were machined, using FIB, from pure iron and weld simulated CGHAZ microstructure. Brittle, catastrophic fracture never occurred but instead stable crack growth was observed. No clear difference between the cantilevers loaded at room temperatures and approximately $-80\text{ }^{\circ}\text{C}$ was observed. The FIB-notched cantilevers exercised two different stages of crack propagation. The first stage consisted of crack blunting, with limited crack propagation. The second stage consisted of stable crack growth. The stable manner of the crack propagation can be explained by a lack of volume able to accumulate elastic energy, causing lower release rates of energy during deformation. The cantilevers yield due to a large plastic zone in front of the crack tip, causing LEFM to render incorrect results. However, LEFM represents the lower limit of the critical fracture toughness values. The critical $K_{Q,J}$ -values represent the upper limit of the critical fracture toughness values. CTOD-values were calculated using a hinge model. Pure iron cantilevers were compared to atomistically modeled cantilevers. Cantilevers machined from pure iron and weld simulated CGHAZ and ICCGAZ microstructures were also compared, revealing variations in fracture mechanical behaviour.

Compression experiments on micro-sized pillars have also been performed. The pillars were machined from microstructures matching those of the cantilevers. The pillars compressed at low temperature exhibited a higher modulus of elasticity than the pillars compressed at room temperature. The calculated stress-strain curves were used to determine the yield strength, used in the cantilever calculations.

The variations in microstructure hardness were mapped using a nanoindenter. The experiment revealed relatively large variations in hardness, indicating local brittle zones. The average modulus of elasticity obtained through the nanoindentation tests was used in the cantilever calculations.

All experiments and microstructural observations contributed to the characterization of the weld simulated microstructure, and its nanomechanical properties.

6 Further Work

The nanoindentation experiment proved to be an interesting tool for microstructure characterization. The method will improve with increasing number of indentations; covering a larger area would yield a more reliable picture of the hardness variations. AFM measurements of the indenter craters would increase the accuracy of the area function used in calculations of the hardness and the reduced modulus of elasticity. Regular calibration is relatively accurate, however, calibration using data from an AFM would make the calculations more precise. This is due to the deformation aspects described in Section 2.6.

The increasing negative value during the cantilever experiments was tested. A more thorough experiment logging the average loading behaviour during displacement controlled testing would increase the understanding of the phenomenon. A better understanding would be useful for tuning the loading function in order to minimize the negative drift. A more specialized tilting of the load-displacement curves would also increase the accuracy of the cantilever calculations. This requires more information of the load behaviour of the indenter, but could make the tilting of the load-displacement curves more realistic. This would again make the calculated K-values more reliable.

Correction for the negative crack growth experienced in the experiment would further increase the accuracy of the calculations. The unloading steps with a calculated negative crack growth strongly affect the following calculations, rendering them less reliable. Compensating for the wrong increased stiffness requires extensive work, but would increase the quality of the calculations.

Machining and testing more samples would strengthen the experiment, due to a better statistical ground. In order to evaluate trends, and spot differences between the different grains and temperatures, an increased number of samples is necessary. However, sample machining is a costly, and time consuming process. Installing a heating unit inside the SEM, allowing full temperature control would enable testing at temperatures between RT and -80°C . This would also increase overall understanding of the governing effects.

7 Acknowledgements

I would like to express gratitude to my supervisor, Professor Christian Thaulow. He has been helpful throughout the entire fifth year of my studies, giving advice and consultation, challenging me, and pushing me to thrive forward. His enthusiasm and merry attitude have strongly motivated me.

I would also like to thank Post Doc Bjørn Rune Sørås Rogne for all his help. His consultation and fruitful discussions helped expanding my theoretical understanding of the fundamental governing theories.

PhD candidate Anette Brocks Hagen has been a delightful partner in the development of the upgraded cryogenic system, and theoretical discussions.

A special thanks goes to Post Doc Stefan Wurster at the Erich Schmid Institute of Materials Science of the Austrian Academy of Sciences. He has offered extensive consultation regarding the experimental analysis and calculations in his paper, which served as the basis for the executed experimental work in this thesis.

A thanks goes to Tone Anzjøn at SINTEF for dedicating her time to help with the challenging LePera etching method. Her experience with sample preparation was astonishing.

Odd Magne Akselsen at SINTEF, and head of the Arctic Materials II project deserves a thanks for his consultation regarding microstructure characterization and cantilever placement.

I wish to thank PhD candidate Tarlan Hajilou for her help in performing the nanoindentations, and calibration of the indenter tip.

Marie Jørum and Cathrine Hartwig deserves a thanks for their cooperation and sharing of their results during our parallel work with our theses.

I would finally like to thank Will Matus and Ingrid Holte for offering orthographic guidance. Their strong skills in the English language helped a lot, and increased the readability of the final draft of the thesis.

References

- [1] J.J. Adams et al. Elastic constants of monocrystal iron from 3 to 500 K. *Journal of Applied Physics*, 100(1):113530–113537, 2006.
- [2] S.R. Agnew and T. Leonhardt. The low-temperature mechanical behaviour of molybdenum-rhenium. *Journal of Materials*, 55(10):25–29, 2003.
- [3] T.L. Anderson. *Fracture Mechanics: Fundamentals and Application*. CRC Press, 2005.
- [4] J.L.M. Andia et al. Microstructural and mechanical properties of the intercritically reheated coarse grained heat affected zone (ICCGHAZ) of an API 5L x80 pipeline steel. *Materials Science Forum*, 783-786(1):657–662, 2014.
- [5] M.P. Ariza et al. Double kink mechanisms for discrete dislocations in BCC crystals. *International Journal of Fracture*, 174(1):29–40, 2012.
- [6] D.E.J. Armstrong et al. Micro-mechanical measurements of fracture toughness of bismuth embrittled copper grain boundaries. *Philosophical Magazine Letters*, 91(6):394–400, 2011.
- [7] D.E.J. Armstrong, M.E. Rogers, and S.G. Roberts. Micromechanical testing of stress corrosion cracking of individual grain boundaries. *Scripta Materialia*, 61(1):741–743, 2009.
- [8] J.A. Begley and J.D. Landes. The J-integral as a fracture criterion. *Fracture Toughness, Proceedings of the 1971 National Symposium on Fracture Mechanics, Part II, ASTM STP 514*, 1(1):1–20, 1972.
- [9] F.M. Beremin. A local criterion for cleavage fracture of a nuclear pressure vessel steel. *Metallurgical transactions A*, 14(A):2277–2287, 1983.
- [10] G. Bernauer et al. Modifications of the beremin model for cleavage fracture in the transition region of a ferritic steel. *Engineering Fracture Mechanics*, 64(1):305–325, 1999.
- [11] H.K.D.H. Bhadeshia and R.W.K. Honeycombe. *Steels, microstructure and properties*. Butterworth-Heinemann, 2006.
- [12] D. Calliard. On the stress discrepancy at low temp pure iron. *Acta Materialia*, 46(5):267–275, 2014.
- [13] W.D. Callister and D.G. Rethwisch. *Materials Science and Engineering*. Wiley, 2011.
- [14] Y. Cao et al. Inferring the temperature dependence of Beremin cleavage model parameters from the Master Curve. *Nuclear Engineering and Design*, 241(1):39–45, 2011.

REFERENCES

- [15] Defense Metals Information Center. The engineering properties of tungsten and tungsten alloys. Battelle Memorial Institute, 1963.
- [16] F.C Ciornei et al. The effect of notch geometry upon shear stress state in a beam. *Mechanical Testing and Diagnosis*, 2(2):68–76, 2012.
- [17] A.H. Cottrell. The formation of immobile dislocations during slip. *Philosophical magazine*, 43(341):645–647, 1952.
- [18] A.H. Cottrell. Theory of brittle fracture in steel and similar metals. *Trans. Met. Soc. AIME*, 212(1):319–326, 1958.
- [19] A.H. Cottrell and B.A. Bilby. Dislocation theory of yielding and strain ageing of iron. *Proc. Phys. Soc.*, 62(1):49–62, 1948.
- [20] D.A. Curry. Cleavage micromechanisms of crack extension in steels. *Metals Science*, 14(8-9):319–326, 1980.
- [21] C.L. Davis and J.E. King. Cleavage initiation in the intercritically reheated coarse-grained heat-affected zone: Part I. fractographic evidence. *Metallurgical and materials transactions A*, 25A(1):563–573, 1994.
- [22] C.L. Davis and J.E. King. Cleavage initiation in the intercritically reheated coarse-grained heat affected zone: Part II. failure criteria and statistical effects. *Metallurgical and materials transactions A*, 27A(1):3019–3029, 1996.
- [23] G.E. Dieter. *Mechanical metallurgy*. McGraw Hill, 1988.
- [24] M.S. Duesbery. On kinked screw dislocations in the BCC lattice - II. kink energies and double kinks. *Acta Metall.*, 31(10):1759–1770, 1982.
- [25] S. Dzaszyk et al. On the characterization of recrystallized fraction using electron backscatter diffraction: A direct comparison to local hardness in an IF steel using nanoindentation. *Materials Science and Engineering A*, 527(1):7854–7864, 2010.
- [26] J. Frenkel. Zur theorie der elastizitätsgrenze und der festigkeit kristallinischer körper. *Zeitschrift für Physik*, 37(7-8):572–609, 1926.
- [27] H. Gao and Y. Huang. Geometrically necessary dislocation and size-dependent plasticity. *Scripta Materiala*, 48(1):113–118, 2002.
- [28] B. Girault et al. Strength effects in micropillars of a dispersion strengthened superalloy**. *Advanced Engineering Materials*, 12(5):385–388, 2010.

-
- [29] K. Greina. In-situ fracture mechanical testing of microsized cantilevers. Master thesis, Norwegian University of Science and Technology.
- [30] Ø. Grong. *Sveisemetallurgi*. NTH Forlag, 1990.
- [31] R. Gröger and V. Vitek. Stress dependence of the Peierls barrier of $1/2\langle 111 \rangle$ screw dislocations in BCC metal. *Acta Materiala*, 61(1):6362–6371, 2013.
- [32] A.B. Hagen. In-situ compression testing of nanosized pillars. Master thesis, Norwegian University of Science and Technology.
- [33] S.E. Han et al. Critical-temperature/Peierls stress dependant size effects in body centered cubic nanopillars. *Applied Physical Letters*, 102(1):041910–1 – 04910–5, 2013.
- [34] P.L. Harrison and R.A. Farrar. Application of continuous cooling transformation diagrams for welding of steels. *International Materials Reviews*, 34(1):35–53, 1989.
- [35] C.G. Hartwig. Acoustic emission from arctic steels and fractographic investigations. Master thesis, Norwegian University of Science and Technology.
- [36] V.G. Haugen. Nanomechanical testing of steel. Master thesis, Norwegian University of Science and Technology.
- [37] V.G. Haugen et al. Local mechanical properties of intercritically reheated coarse grained heat affected zone in low alloy steel. *Materials and Design*, 59(1):135–140, 2014.
- [38] L.E. Svensson H.K.D.H. Bhadeshia and B. Grefott. A model for the development of microstructure in low-alloy steel (Fe-Mn-Si-C) weld deposits. *Acta metall.*, 33(7):1271–1283, 1984.
- [39] B. Holmedal. Mechanical properties of metals. University Lecture, 2013.
- [40] D. Hull and D.J. Bacon. *Introduction to Dislocations*. Elsevier, 2011.
- [41] J.W. Hutchinson. Singular behavior at the end of a tensile crack tip in a power-law hardening material. *Journal of the Mechanics and Physics of Solids*, 16(1):13–31, 1968.
- [42] British Standards Institution. *Methods for Crack Opening Displacement (COD) Testing*. DD 19:1972, London, 1972.
- [43] ASTM International. *ASTM Standard E 813-89* (withdrawn 1997). West Conshohocken, PA, 1989.
-

REFERENCES

- [44] ASTM International. *ASTM Standard E 1820-99a*. West Conshohocken, PA, 2001.
- [45] ASTM International. *ASTM Standard E399-09*. West Conshohocken, PA, 2003.
- [46] G.R. Irwin. Onset of fast crack propagation in high strength steel and aluminium alloys. *Sagamore Research Conference Proceedings*, 2(1):289–305, 1956.
- [47] T.V. Jayaraman et al. Corrosion studies of single crystals of iron–gallium alloys in aqueous environments. *Corrosion Science*, 147(1):4015–4027, 2007.
- [48] W.G. Johnston and J.J. Gilman. Dislocation velocities, dislocation densities, and plastic flow in lithium fluoride crystals. *Journal of Applied Physics*, 30(2):129–144, 1959.
- [49] M. Jørum. Atomistic modeling of fracture mechanics testing. Master thesis, Norwegian University of Science and Technology.
- [50] D. Keiner et al. In situ nanocompression testing of irradiated copper. *Nature Materials*, 10(1):608–613, 2011.
- [51] D. Kiener, C. Motz, et al. FIB damage of Cu and possible consequences for miniaturized mechanical tests. *Materials Science and Engineering: A*, 459(1-2):262–272, 2007.
- [52] L.P. Kubin. *Dislocations, Mesoscale and Crystal Defects*. Wiley, 2012.
- [53] A.L.L. Kvaal. Low temperature nanomechanical testing of microsized cantilevers. Specialization project, Norwegian University of Science and Technology.
- [54] A.L.L. Kvaal. Nanomechanical testing of ICCGHAZ of arctic steel. Master thesis, Norwegian University of Science and Technology.
- [55] A. Lambert-Perlade et al. Mechanisms and modeling of cleavage fracture in simulated heat-affected zone microstructures of a high-strength low alloy steel. *Metallurgical and Materials Transactions A*, 35(A):1039–1053, 2004.
- [56] J.D. Landes and J.A. Begley. The effect of specimen geometry on J_{Ic} . *Fracture Toughness, Proceedings of the 1971 National Symposium on Fracture Mechanics, Part II, ASTM STP 514*, 1(1):24–39, 1972.
- [57] S. Lee. Cold-temperature deformation of nano-sized tungsten and niobium as revealed by in-situ nanomechanical experiments. *Science China*, 57(4):652–662, 2014.
- [58] F.S. Lepera. Improved etching technique for the determination of percent martensite in high-strength dual-phase steels. *Metallography*, 12(3):263–268, 1979.

-
- [59] J. Li et al. Energy landscape of deformation twinning in BCC and FCC metals. *Physical Review B*, 71(22):224102–1 – 224102–11, 2005.
- [60] Y. Li and T.N. Baker. Effect of morphology of martensite–austenite phase on fracture of weld heat affected zone in vanadium and niobium microalloyed steels. *Materials Science and Technology*, 26(9):1029–1040, 2010.
- [61] Y. Li et al. The effect of vanadium and niobium on the properties and microstructure of the intercritically reheated coarse grained heat affected zone in low carbon microalloyed steels. *ISIJ International*, 41(1):46–55, 2001.
- [62] N. Louat. The Peierls-Nabarro force and the deformation of iron and steel. *Aeronautical Research Laboratories*, 1959.
- [63] A. Lupinacci et al. Cryogenic in-situ microcompression testin of Sn. *Acta Materiala*, 78(1):56–64, 2014.
- [64] D. Di Maio and S.G. Roberts. Measuring fracture toughness of coatings using focused-ion-beam-machined microbeams. *J. Mater. Res.*, 20(2):299–302, 2005.
- [65] K. Matoy et al. A comparative micro-cantilever study of the mechanical behavior of silicon based passivation films. *Thin Solid Films*, 518(1):247–256, 2009.
- [66] P. Mohseni et al. Investigation of mechanism of cleavage fracture initiation in intercritically coarse grained heat affected zone of HSLA steel. *Materials Science and Technology*, 28(11):1261–1268, 2012.
- [67] P. Mohseni et al. Cleavage fracture initiation at M-A constituents in intercritically coarse-grained heat-affected zone of a HSLA steel. *Metallurgical and Materials Transactions A*, 45A(1):384–394, 2014.
- [68] C. Motz et al. Mechanical properties of micro-sized copper bending beams machined by the focused ion beam technique. *Acta Materiala*, 53(1):4269–4279, 2005.
- [69] Y. Murakami. *Stress Intensity Factors Handbook*. Pergamon Press, 1987.
- [70] V.I. Novelli. The unloading stiffness of reinforced concrete members. Master thesis, Istituto Universitario di Studi Superiori di Pavia.
- [71] W.C. Oliver and G.M. Pharr. An improved technique for determining hardness and elastic modulus using load and displacement sensing indentation experiments. *Journal of materials research*, 7(6):1564–1583, 1992.
-

REFERENCES

- [72] S.R. Pergande et al. Use of nano-indentation and nano-scratch techniques to investigate near surface material properties associated with scuffing of engineering surfaces. *ACRC Project No. 127*, 2001.
- [73] N.J. Petch. The ductile-brittle transition in fracture of α -iron: I. *Philosophical Magazine*, 3(34):1089–1097, 1958.
- [74] J.R. Rice. A path independent integral and the approximate analysis of strain concentration by notches and cracks. *Journal of Applied Mechanics*, 35(1):379–386, 1968.
- [75] J.R. Rice and G.F. Rosengren. Plane strain deformation near a crack tip in a power-law hardening material. *Journal of the Mechanics and Physics of Solids*, 16(1):1–12, 1968.
- [76] J.N. Robinson. An experimental investigation of the effect of specimen type on the crack tip opening displacement and J-integral fracture criteria. *International Journal of Fracture*, 12(5):723–737, 1976.
- [77] B.R.S. Rogne. Nanomechanical testing of iron and steel. Phd thesis, Norwegian University of Science and Technology.
- [78] I. Ryu et al. Cold-temperature deformation of nano-sized tungsten and niobium as revealed by in-situ nano-mechanical experiments. *Sci China Tech Sci*, 57(4):652–662, 2014.
- [79] A.S. Schneider et al. Influence of orientation on the size effect in BCC pillars with different critical temperatures. *Materials Science and Engineering A*, 528(A):1540–1547, 2011.
- [80] C.S Seok. Correction methods of an apparent negative crack growth phenomenon. *International Journal of Fracture*, 102(1):259–269, 2000.
- [81] C.F. Shih. Relationships between the J-integral and the crack opening displacement for stationary and extending cracks. *J. Mech. Phys. Solids*, 29(4):305–326, 1981.
- [82] I. Shin. Possible origin of the discrepancy in Peierls stresses of FCC materials: First-principle simulations of dislocation mobility in aluminium. *Physical Review B*, 88(6):064106(10), 2013.
- [83] SINTEF. Evaluation of 420 MPa steel welds. Report, SINTEF Materials and Chemistry.
- [84] E. Smith. The formation of a cleavage crack in a crystalline solid - I. *Acta Metallurgica*, 14(1):985–989, 1966.
- [85] E. Smith. The formation of a cleavage crack in a crystalline solid - II. *Acta Metallurgica*, 14(1):991–996, 1966.

-
- [86] E. Smith. Physical basis of yield and fracture. *Proc. Conf.*, 36, 1966.
- [87] B.D. Snartland. Low temperature nanomechanical testing of pillars. Specialization project, Norwegian University of Science and Technology.
- [88] B.D. Snartland. Nanomechanical testing of CGHAZ of arctic steel. Master thesis, Norwegian University of Science and Technology.
- [89] J.K. Solberg. *Teknologiske metaller og legeringer*. NTNU Forlag, 2011.
- [90] J.E. Srawley and B. Gross. *Side cracked plates subject to combined direct and bending forces*. Ninth Symposium on Fracture Mechanics by ASTM, Pittsburgh, PA, 1975.
- [91] G.W. Stachowiak and A.W. Batchelor. *Engineering Tribology*. Butterworth-Heinemann, 2014.
- [92] G.I. Taylor. The mechanisms of plastic deformation of crystals. part I. Theoretical. *Proceedings of the Royal Society of London*, A145(855):362–387, 1934.
- [93] C.A. Volkert and A.M. Minor. Focused ion beam microscopy and micromachining. *MRS Bulletin*, 32(5):389–399, 2007.
- [94] W.Y. Wang et al. Effect of temperature on strength and elastic modulus of high-strength steel. *Journal of Materials in Civil Engineering*, 25(2):174–182, 2013.
- [95] S. Wurster et al. Characterization of the fracture toughness of micro-sized tungsten single crystal notched specimens. *Philosophical Magazine*, 92(14):1803–1825, 2012.
- [96] S. Wurster, C. Motz, and R. Pippan. Notched-cantilever testing on the micrometer scale - effects of constraints on plasticity and fracture behaviour. *Proceedings of the 18th European Conference on Fracture*, 2010.
- [97] X. Zhao et al. Mechanical properties of SiC coatings on spherical particles measured using the micro-beam method. *Scripta Materialia*, 59(1):39–42, 2008.
- [98] L. Zhu et al. Measurement of residual stress in quenched 1045 steel by the nanoindentation method. *Materials characterization*, 61(1):1359–1362, 2010.
- [99] E. Østby, C. Thaulow, and O. M. Akselsen. Characterization of the fracture toughness of micro-sized tungsten single crystal notched specimens. *Proceedings of the Twenty-first (2011) International Offshore and Polar Engineering Conference*, 1(1):443–448, 2011.
-

REFERENCES

A Sample dimensions

Table 12: Dimensions for all CGHAZ and ICCGHAZ pillars.

Material	Pillar	Height [μm]	Diameter [μm]
CGHAZ	4-1	3.46	1.02
CGHAZ	4-2	3.24	1.05
CGHAZ	6-1	3.05	1.07
CGHAZ	6-2	4.26	1.13
ICCGHAZ	7-MA	3.23	1.07
ICCGHAZ	8	3.33	1.02
ICCGHAZ	10-MA	3.6	1.03
ICCGHAZ	11	3	0.83

Table 13: Dimensions for all pure iron, CGHAZ and ICCGHAZ cantilevers.

Material	Cantilever	Bending length, L [μm]	Width, w [μm]	Side height, b [μm]
Pure iron	Fe3	8	2.29	1.1
Pure iron	Fe4	8	2.06	1.1
CGHAZ	1-1	8	1.5	1.34
CGHAZ	1-2	8	2	1.02
CGHAZ	2-3	8	2.02	0.95
CGHAZ	2-4	8	1.6	1.36
ICCGHAZ	2	8	2	1.24
ICCGHAZ	3D	8	2.22	0.9
ICCGHAZ	4	8	2.12	1.22
ICCGHAZ	5D	8	1.85	1.12

B Risk Assessment



ID	151	Status	Dato
Risikoområde	Risikovurdering: Helse, miljø og sikkerhet (HMS)	Opprettet	03.02.2015
Opprettet av	Brage Dahl Snartland	Vurdering startet	03.02.2015
Ansvarlig	Brage Dahl Snartland	Tiltak besluttet	
		Avsluttet	

Risikovurdering for Brage Dahl Snartlands Masteroppgave

Gyldig i perioden:

1/12/2015 - 8/1/2015

Mål / hensikt

Senke sannsynligheten for uønskede hendelser under arbeid med prosjektoppgaven.

Bakgrunn

Rutinemessig arbeid i forbindelse med masteroppgave.

Beskrivelse og avgrensninger

Det skal kun arbeides på NanoLab, nanomekanisk lab hos IPM, eller metallurgilaboratoriet hos IPM.

Forutsetninger, antakelser og forenklinger

[Ingen registreringer]

Vedlegg

[Ingen registreringer]

Referanser

[Ingen registreringer]



Oppsummering, resultat og endelig vurdering

I oppsummeringen presenteres en oversikt over farer og uønskede hendelser, samt resultat for det enkelte konsekvensområdet.

Farekilde: **Bruk av Focused Ion Beam (FIB)**

Uønsket hendelse: **Spenning og Stråling**

Konsekvensområde: Helse

Risiko før tiltak: Risiko etter tiltak:

Uønsket hendelse: **Skade på utstyr**

Konsekvensområde: Materielle verdier

Risiko før tiltak: Risiko etter tiltak:

Farekilde: **Bruk av Scanning Electron Microscope**

Uønsket hendelse: **Spenning og stråling**

Konsekvensområde: Helse

Risiko før tiltak: Risiko etter tiltak:

Uønsket hendelse: **Skade på utstyr**

Konsekvensområde: Materielle verdier

Risiko før tiltak: Risiko etter tiltak:

Farekilde: **Håndtering av flytende nitrogen**

Uønsket hendelse: **Frostskader ved uhell**

Konsekvensområde: Helse

Risiko før tiltak: Risiko etter tiltak:

Uønsket hendelse: **Kveining**

Konsekvensområde: Helse

Risiko før tiltak: Risiko etter tiltak:

Farekilde: **Bruk av slipebord**

Uønsket hendelse: **Skade på utstyr**

Konsekvensområde: Materielle verdier

Risiko før tiltak: Risiko etter tiltak:

Uønsket hendelse: **Roterende slipebord**

Konsekvensområde: Helse

Risiko før tiltak: Risiko etter tiltak:

Endelig vurdering



Oversikt involverte enheter og personell

En risikovurdering kan gjelde for en, eller flere enheter i organisasjonen. Denne oversikten presenterer involverte enheter og personell for gjeldende risikovurdering.

Enhet /-er risikovurderingen omfatter

- Norges teknisk-naturvitenskapelige universitet
- NTNU
- Fakultet for ingeniørvitenskap og teknologi
- Institutt for produktutvikling og materialer

Deltakere

Aksel Louis Legouy Kvaal
Anette Brocks Hagen
Bjørn Rune Rogne

Lesere

[Ingen registreringer]

Andre involverte/interessenter

[Ingen registreringer]

Følgende akseptkriterier er besluttet for risikoområdet Risikovurdering: Helse, miljø og sikkerhet (HMS):

Helse



Materielle verdier



Omdømme



Ytre miljø



**Oversikt over eksisterende, relevante tiltak som er hensyntatt i risikovurderingen**

I tabellen under presenteres eksisterende tiltak som er hensyntatt ved vurdering av sannsynlighet og konsekvens for aktuelle uønskede hendelser.

Farekilde	Uønsket hendelse	Tiltak hensyntatt ved vurdering
Bruk av Focused Ion Beam (FIB)	Spenning og Stråling	Opplæring
	Spenning og Stråling	Opplæring FIB og SEM
	Spenning og Stråling	HMS-kurs
	Spenning og Stråling	Bruk av verneutstyr
	Skade på utstyr	Opplæring FIB og SEM
	Skade på utstyr	HMS-kurs
	Skade på utstyr	Bruk av verneutstyr
Bruk av Scanning Electron Microskope	Spenning og stråling	Opplæring FIB og SEM
	Spenning og stråling	HMS-kurs
	Spenning og stråling	Bruk av verneutstyr
	Skade på utstyr	Opplæring FIB og SEM
	Skade på utstyr	HMS-kurs
	Skade på utstyr	Bruk av verneutstyr
Håndtering av flytende nitrogen	Frostskader ved uhell	Opplæring
	Frostskader ved uhell	HMS-kurs
	Frostskader ved uhell	Bruk av verneutstyr
	Kvelning	Opplæring
	Kvelning	HMS-kurs
	Kvelning	Bruk av verneutstyr
Vasking av utstyr i etanol		
Bruk av slipebord	Skade på utstyr	Opplæring
	Skade på utstyr	HMS-kurs
	Skade på utstyr	Bruk av verneutstyr
	Roterende slipebord	Opplæring
	Roterende slipebord	HMS-kurs
	Roterende slipebord	Bruk av verneutstyr

Eksisterende og relevante tiltak med beskrivelse:**Opplæring**

Rentromskurs

Opplæring FIB og SEM

Kurs i sikker bruk av FIB og SEM



HMS-kurs

[Ingen registreringer]

Bruk av verneutstyr

[Ingen registreringer]

Risikoanalyse med vurdering av sannsynlighet og konsekvens

I denne delen av rapporten presenteres detaljer dokumentasjon av de farer, uønskede hendelser og årsaker som er vurdert. Innledningsvis oppsummeres farer med tilhørende uønskede hendelser som er tatt med i vurderingen.

Følgende farer og uønskede hendelser er vurdert i denne risikovurderingen:

- **Bruk av Focused Ion Beam (FIB)**
 - Spenning og Stråling
 - Skade på utstyr
- **Bruk av Scanning Electron Microskope**
 - Spenning og stråling
 - Skade på utstyr
- **Håndtering av flytende nitrogen**
 - Frostskafer ved uhell
 - Kvelning
- **Bruk av slipebord**
 - Skade på utstyr
 - Roterende slipebord

Oversikt over besluttede risikoreduserende tiltak med beskrivelse:



Bruk av Focused Ion Beam (FIB) (farekilde)

Bruk av Focused Ion Beam (FIB)/Spenning og Stråling (uønsket hendelse)

Samlet sannsynlighet vurdert for hendelsen: Svært lite sannsynlig (1)

Kommentar til vurdering av sannsynlighet:

[Ingen registreringer]

Vurdering av risiko for følgende konsekvensområde: Helse

Vurdert sannsynlighet (felles for hendelsen): Svært lite sannsynlig (1)

Vurdert konsekvens: Svært stor (4)

Kommentar til vurdering av konsekvens:

Fare for dødelig støt



Bruk av Focused Ion Beam (FIB)/Skade på utstyr (uønsket hendelse)

Samlet sannsynlighet vurdert for hendelsen: Lite sannsynlig (2)

Kommentar til vurdering av sannsynlighet:

Jobber forsiktig når utstyr monteres og brukes inne i kammeret.

Vurdering av risiko for følgende konsekvensområde: Materielle verdier

Vurdert sannsynlighet (felles for hendelsen): Lite sannsynlig (2)

Vurdert konsekvens: Stor (3)

Kommentar til vurdering av konsekvens:

Dyrt utstyr





Bruk av Scanning Electron Microskope (farekilde)

Bruk av Scanning Electron Microskope/Spenning og stråling (uønsket hendelse)

Samlet sannsynlighet vurdert for hendelsen: Svært lite sannsynlig (1)

Kommentar til vurdering av sannsynlighet:

[Ingen registreringer]

Vurdering av risiko for følgende konsekvensområde: Helse

Vurdert sannsynlighet (felles for hendelsen): Svært lite sannsynlig (1)

Vurdert konsekvens: Stor (3)

Kommentar til vurdering av konsekvens:

[Ingen registreringer]



Bruk av Scanning Electron Microskope/Skade på utstyr (uønsket hendelse)

Samlet sannsynlighet vurdert for hendelsen: Lite sannsynlig (2)

Kommentar til vurdering av sannsynlighet:

[Ingen registreringer]

Vurdering av risiko for følgende konsekvensområde: Materielle verdier

Vurdert sannsynlighet (felles for hendelsen): Lite sannsynlig (2)

Vurdert konsekvens: Stor (3)

Kommentar til vurdering av konsekvens:

Dyrt utstyr





Håndtering av flytende nitrogen (farekilde)

Håndtering av flytende nitrogen/Frostskader ved uhell (uønsket hendelse)

Samlet sannsynlighet vurdert for hendelsen: Lite sannsynlig (2)

Kommentar til vurdering av sannsynlighet:

[Ingen registreringer]

Vurdering av risiko for følgende konsekvensområde: Helse

Vurdert sannsynlighet (felles for hendelsen): Lite sannsynlig (2)

Vurdert konsekvens: Middels (2)

Kommentar til vurdering av konsekvens:

[Ingen registreringer]



Håndtering av flytende nitrogen/Kvelning (uønsket hendelse)

Samlet sannsynlighet vurdert for hendelsen: Svært lite sannsynlig (1)

Kommentar til vurdering av sannsynlighet:

[Ingen registreringer]

Vurdering av risiko for følgende konsekvensområde: Helse

Vurdert sannsynlighet (felles for hendelsen): Svært lite sannsynlig (1)

Vurdert konsekvens: Svært stor (4)

Kommentar til vurdering av konsekvens:

Farlig





Bruk av slipebord (farekilde)

Bruk av slipebord/Skade på utstyr (uønsket hendelse)

Samlet sannsynlighet vurdert for hendelsen: Lite sannsynlig (2)

Kommentar til vurdering av sannsynlighet:

[Ingen registreringer]

Vurdering av risiko for følgende konsekvensområde: Materielle verdier

Vurdert sannsynlighet (felles for hendelsen): Lite sannsynlig (2)

Vurdert konsekvens: Middels (2)

Kommentar til vurdering av konsekvens:

Relativt billig utstyr



Bruk av slipebord/Roterende slipebord (uønsket hendelse)

Samlet sannsynlighet vurdert for hendelsen: Sannsynlig (3)

Kommentar til vurdering av sannsynlighet:

[Ingen registreringer]

Vurdering av risiko for følgende konsekvensområde: Helse

Vurdert sannsynlighet (felles for hendelsen): Sannsynlig (3)

Vurdert konsekvens: Liten (1)

Kommentar til vurdering av konsekvens:

[Ingen registreringer]





Oversikt over besluttede risikoreducerende tiltak:

Under presenteres en oversikt over risikoreducerende tiltak som skal bidra til å reduseres sannsynlighet og/eller konsekvens for uønskede hendelser.

Oversikt over besluttede risikoreducerende tiltak med beskrivelse:



C A3-Posters



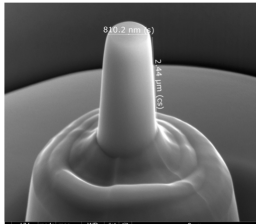
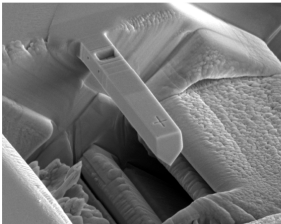

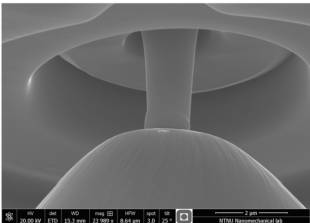
<p>Masters degree IPM Spring 2015</p> <p>Nanomechanical Testing of CGHAZ of Arctic Steel</p> <p>by Brage Dahl Snartland</p>  <p>Supervisor: Christian Thaulow</p>  <p>Det skapende universitet</p>	<p>The Arctic activity is on the rise. High quality materials are necessary to explore these areas. A harsh climate, and extreme temperatures forces an increased understanding of low temperature material deformation. Rapid advancement within nanotechnology enable detailed material characterization by utilizing nanomechanical testing methods.</p>   <p>Pillars and cantilevers will be machined from weld simulated steel.</p>   <p>Weld simulated arctic steel will be cut, and the relevant microstructure will be prepared for milling of micro samples.</p> <p>The pillars and cantilevers will be deformed at arctic temperatures.</p>
---	--

Figure 86: The A3-Poster presented at the start of the semester.

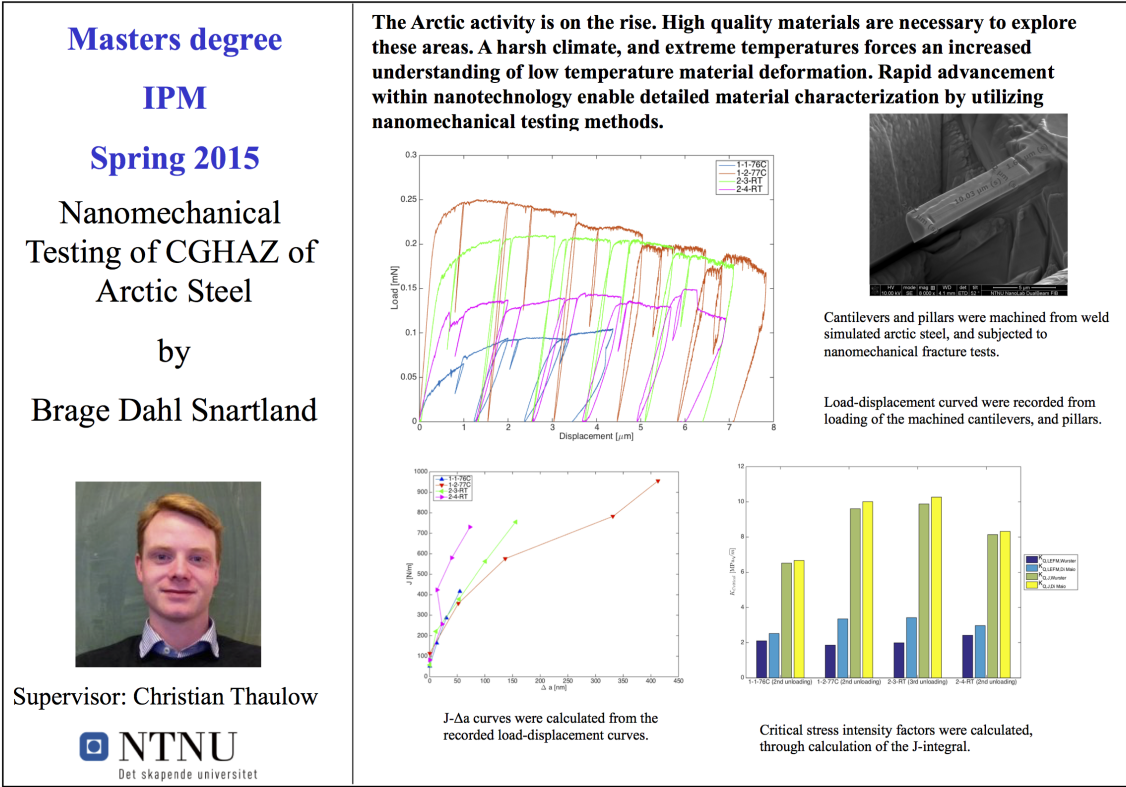
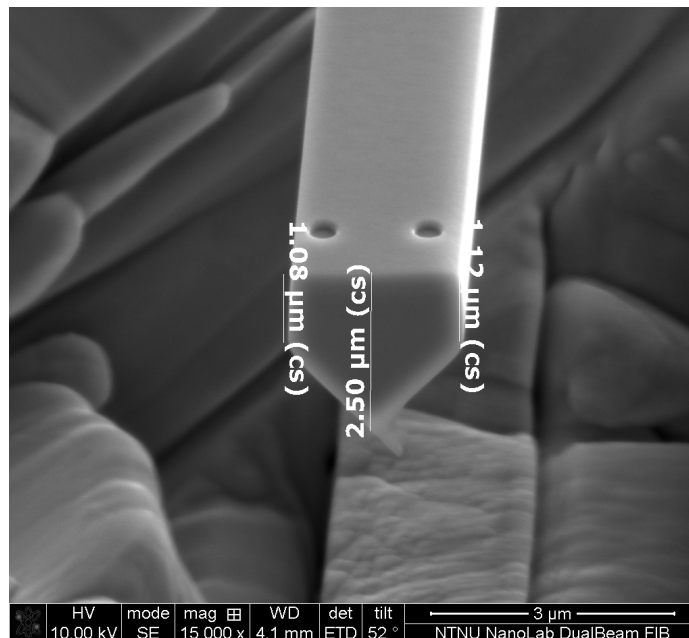
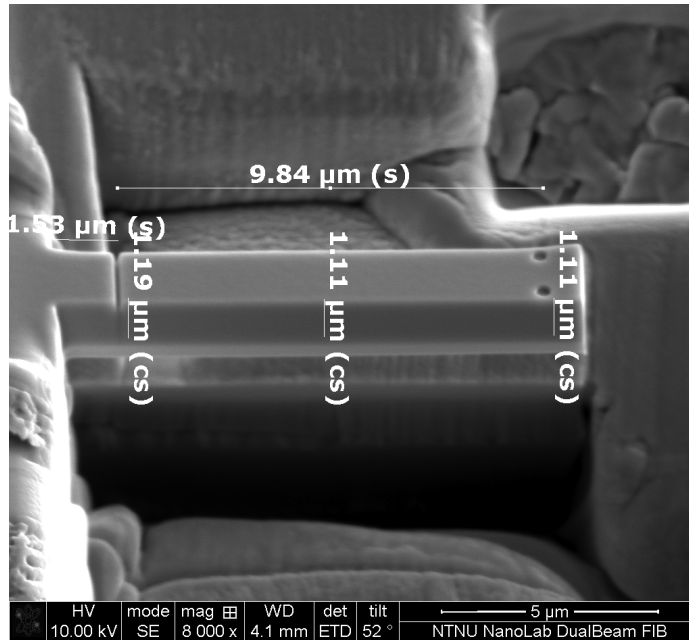
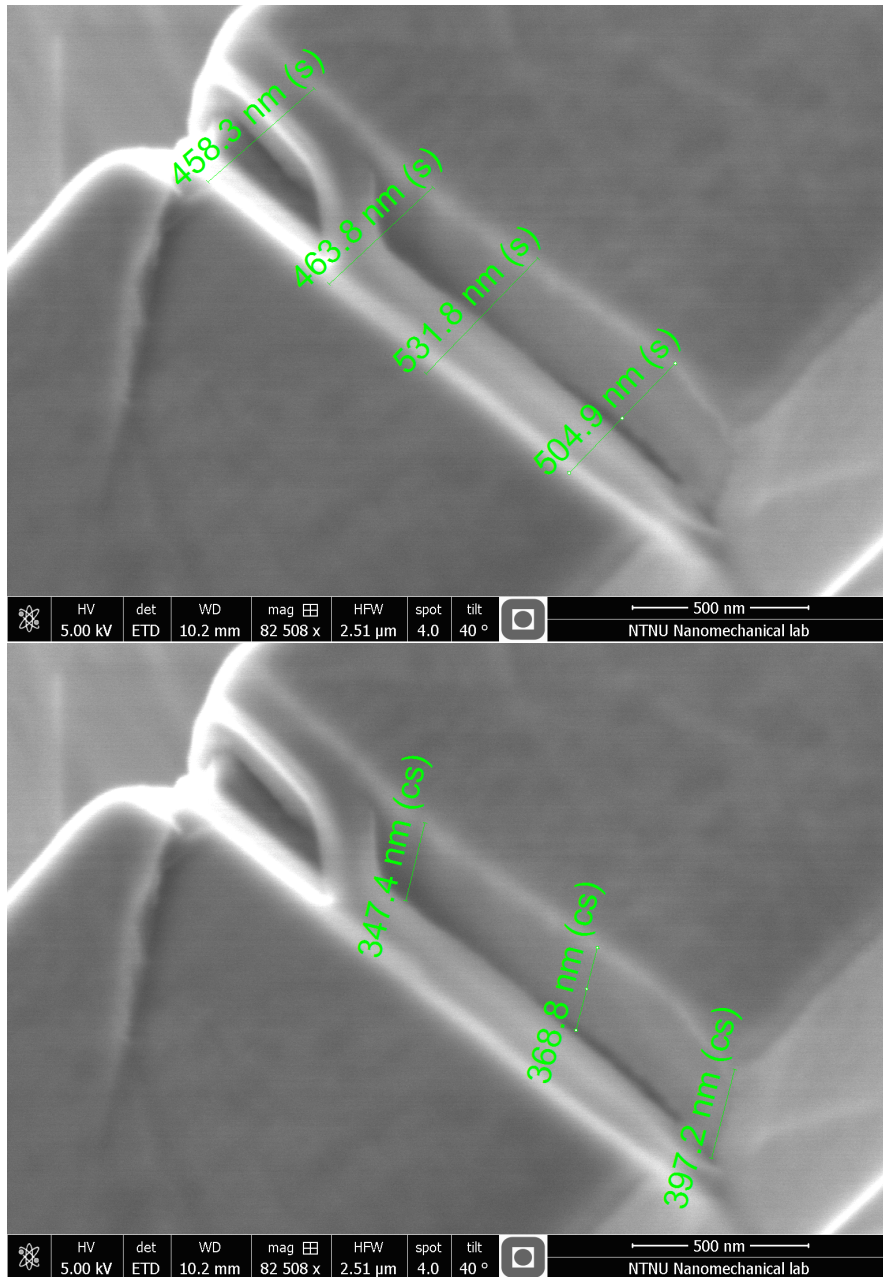


Figure 87: The A3-Poster presented at the end of the semester

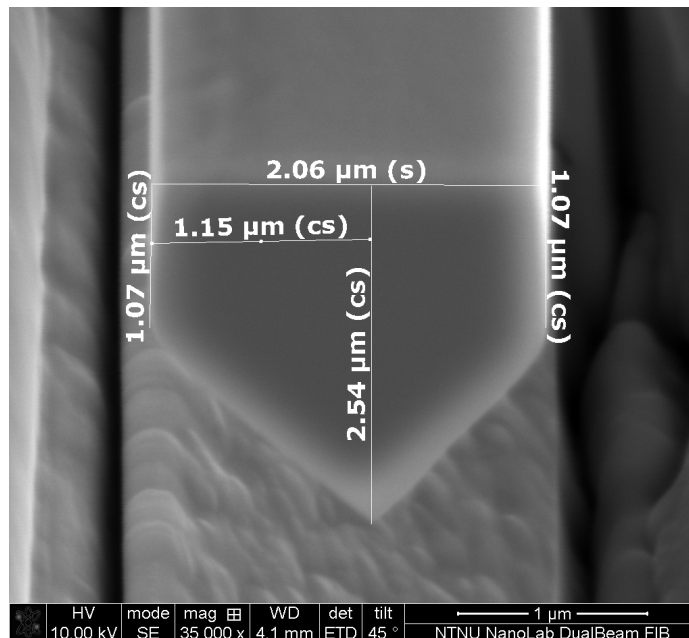
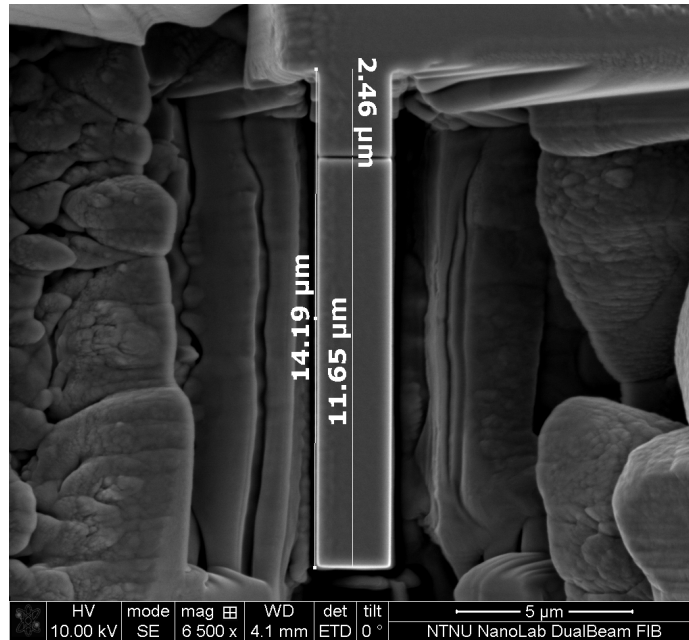
D SEM Images of Cantilevers and Pillars

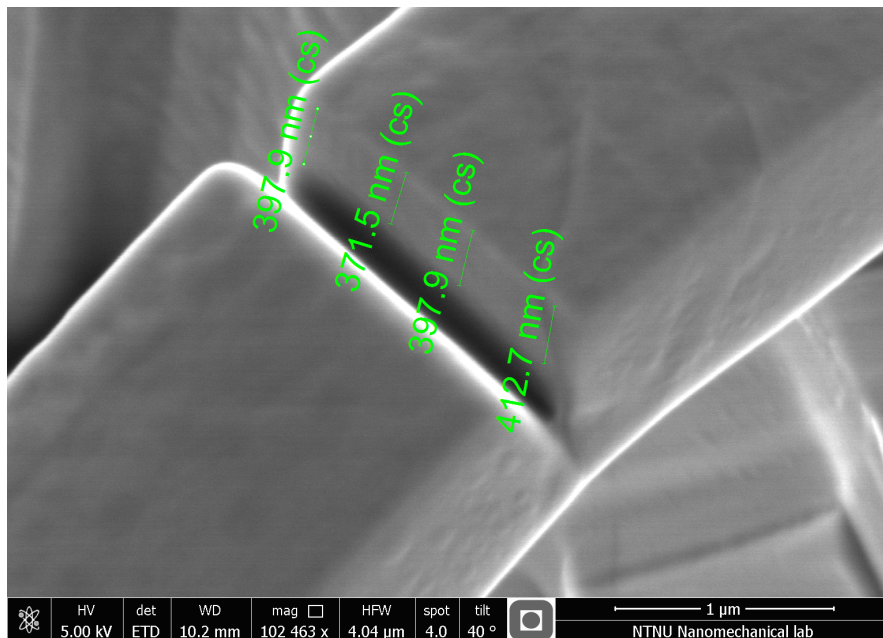
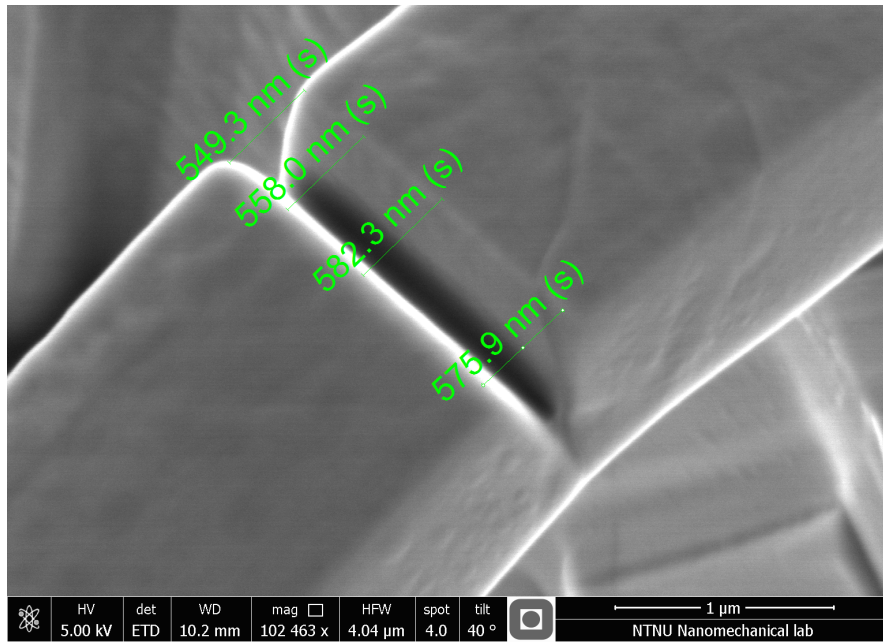
D.1 Cantilever Fe3



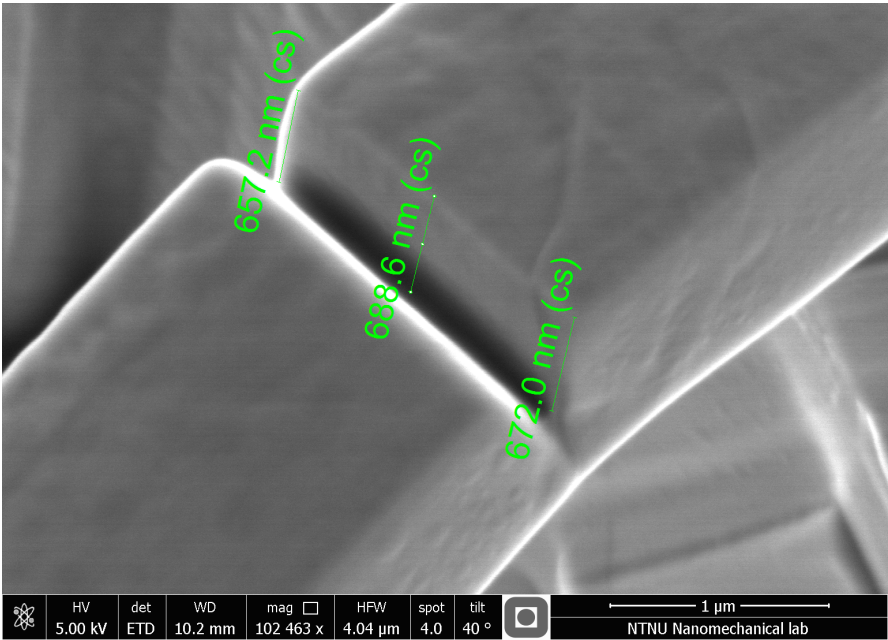


D.2 Cantilever Fe4

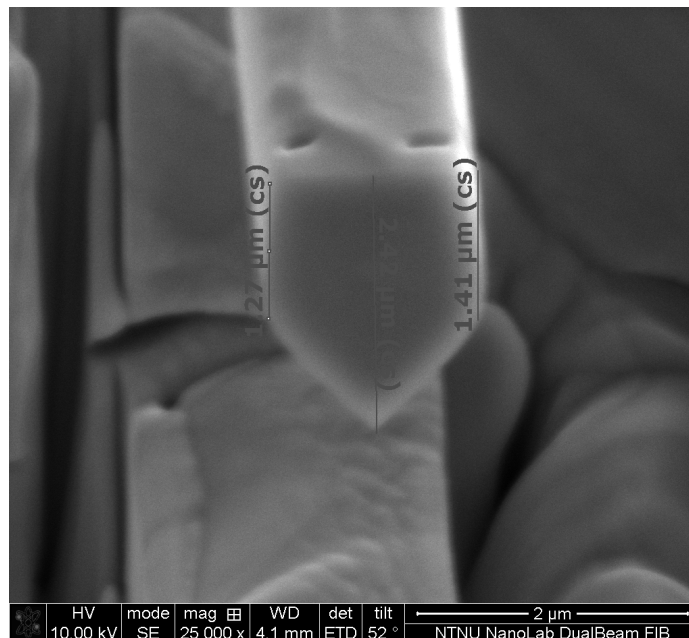
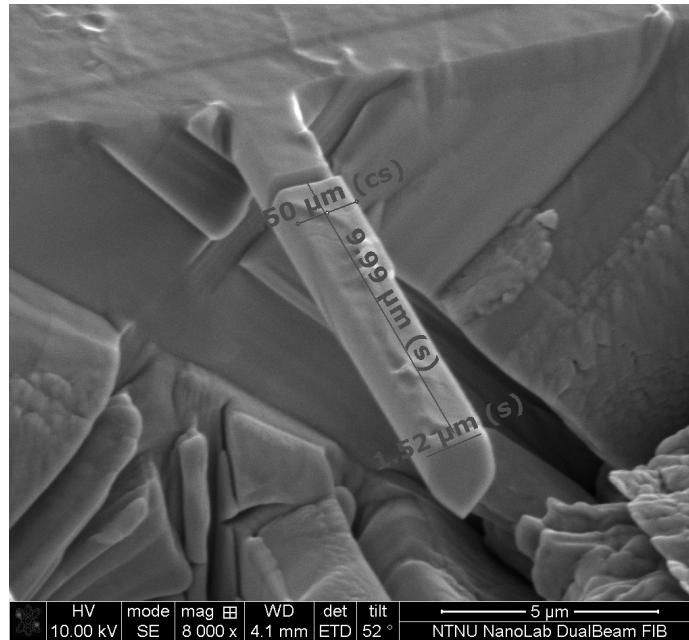




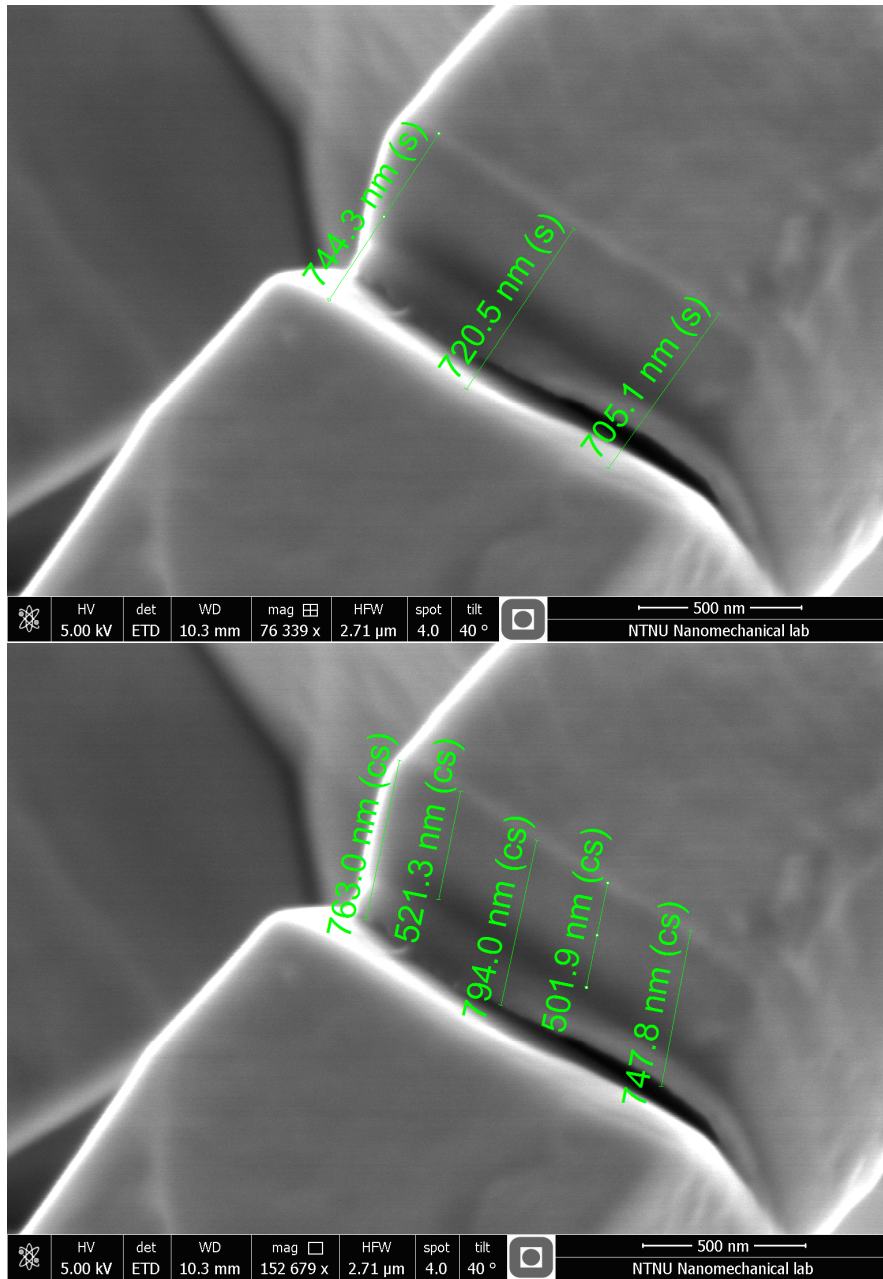
D SEM IMAGES OF CANTILEVERS AND PILLARS



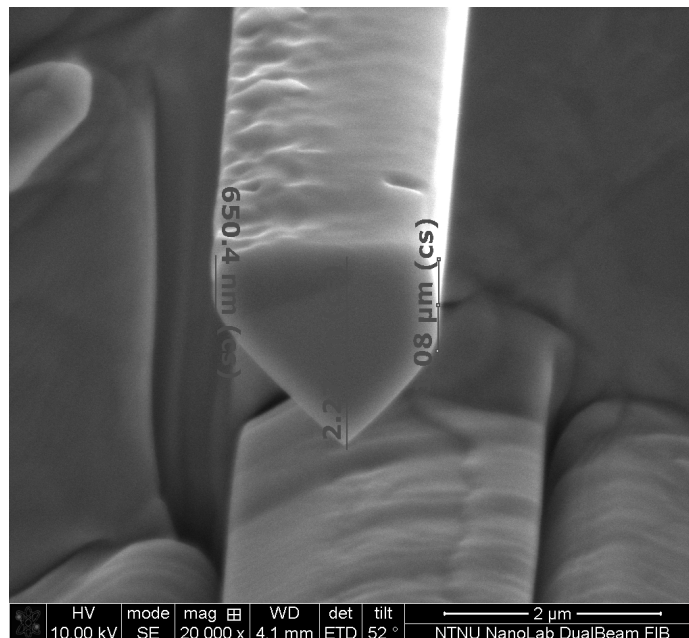
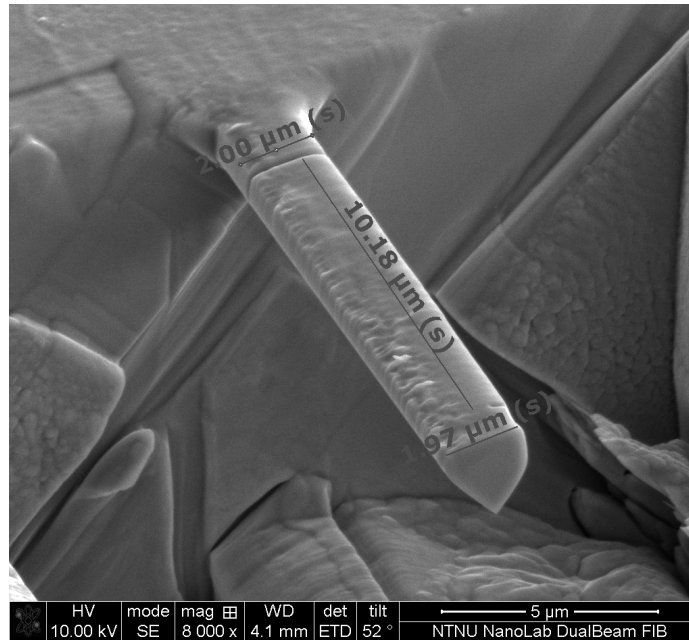
D.3 Cantilever 1-1 CGHAZ



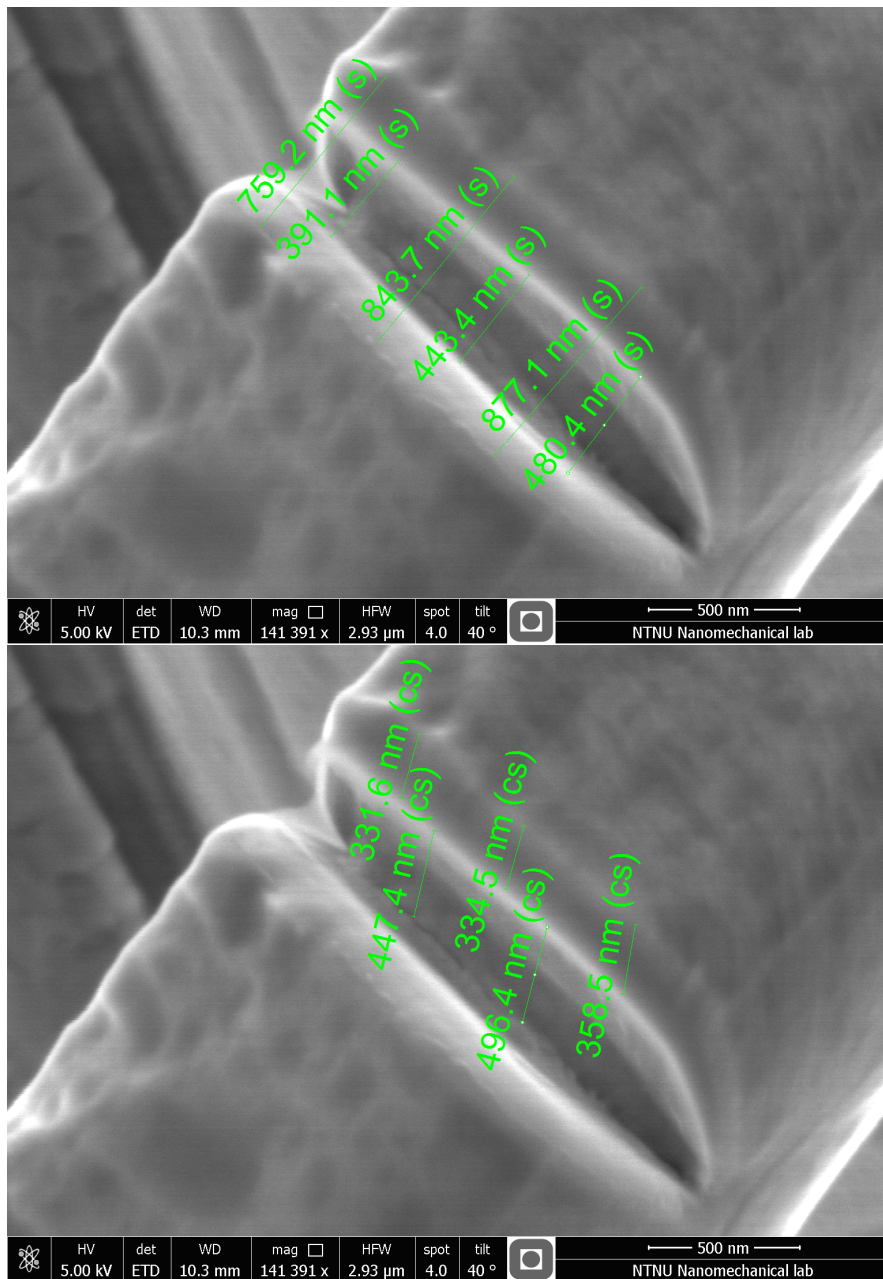
D SEM IMAGES OF CANTILEVERS AND PILLARS



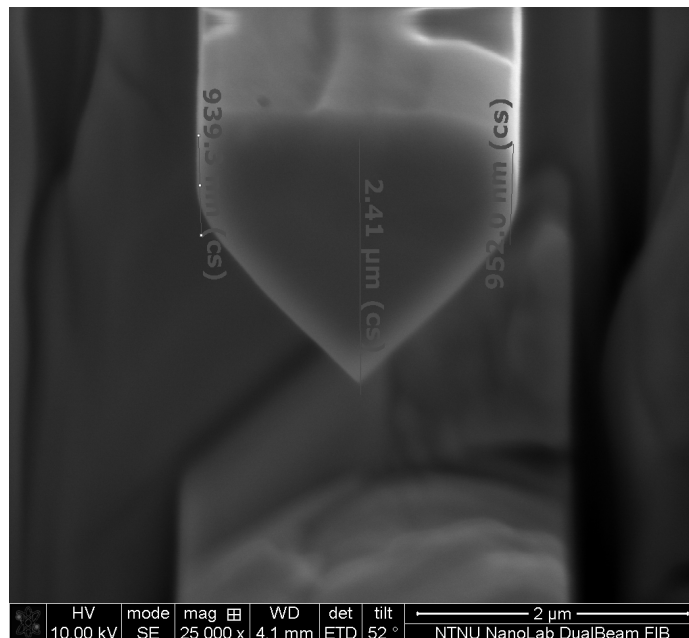
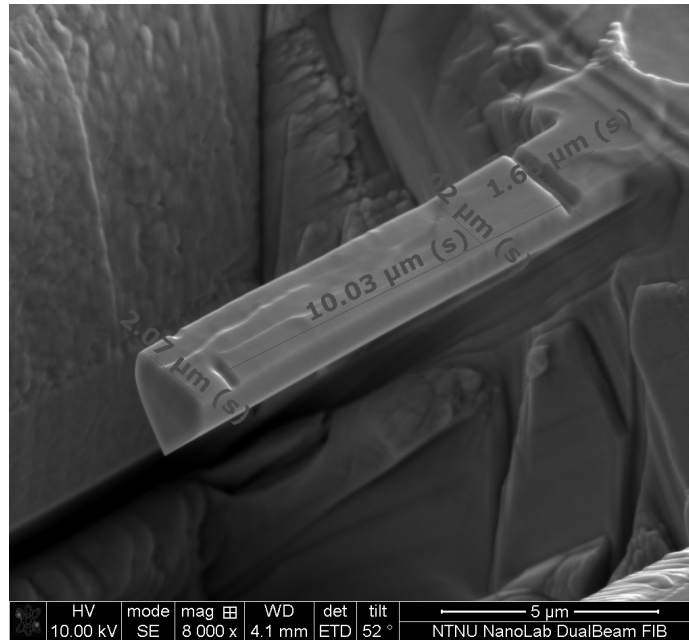
D.4 Cantilever 1-2 CGHAZ



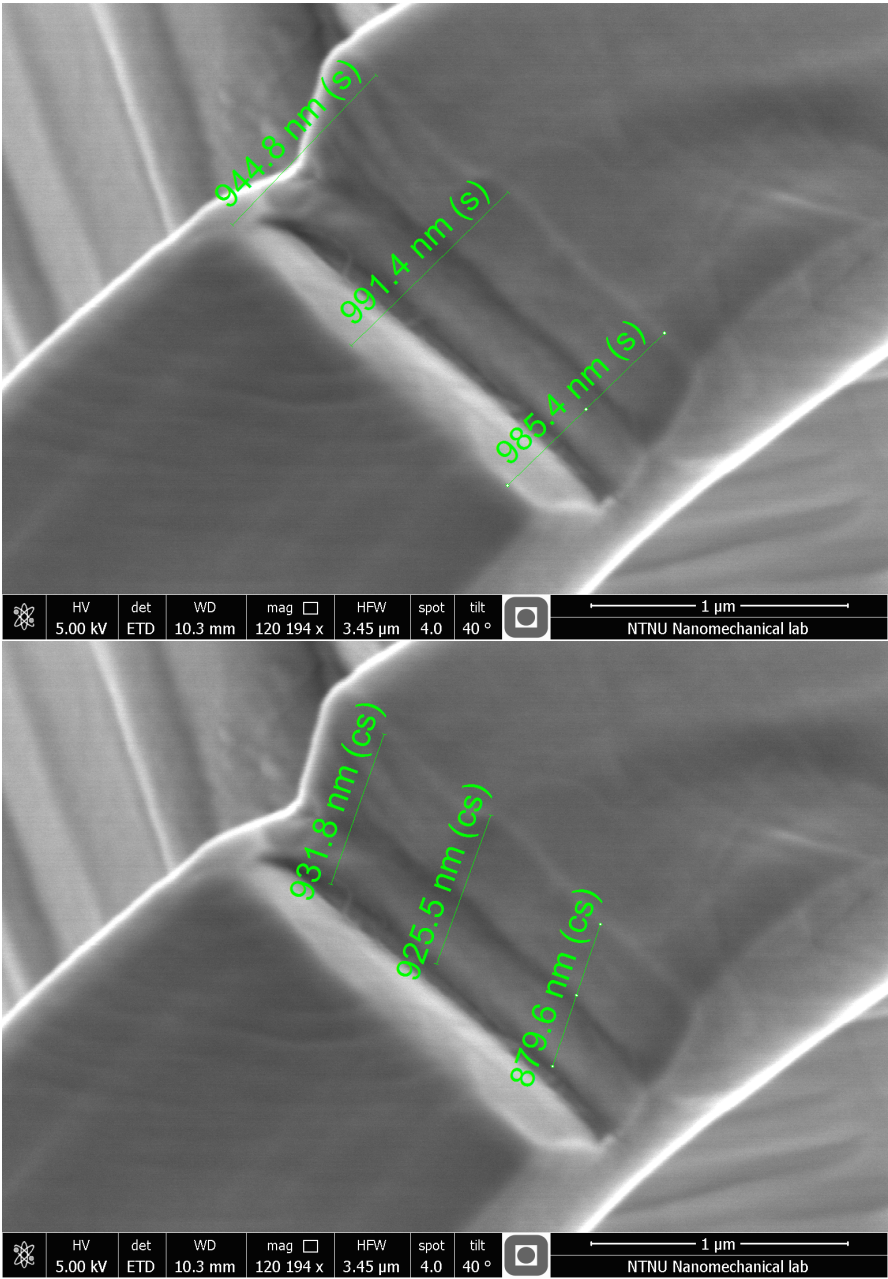
D SEM IMAGES OF CANTILEVERS AND PILLARS



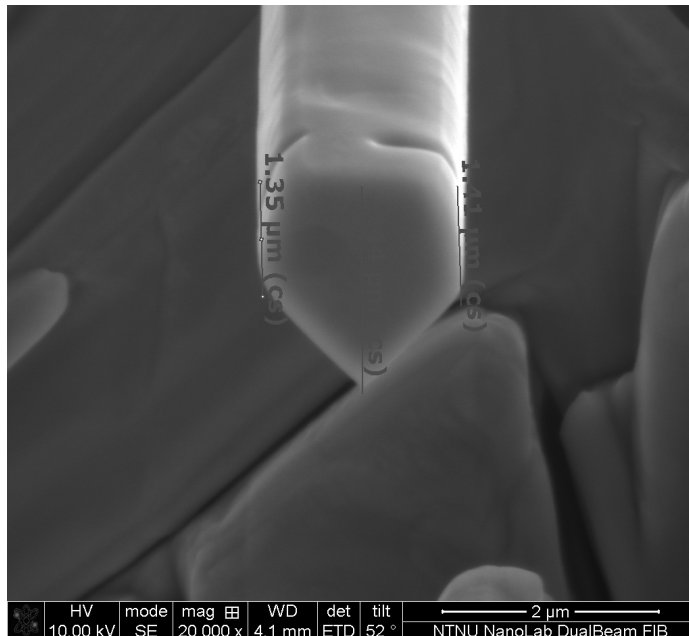
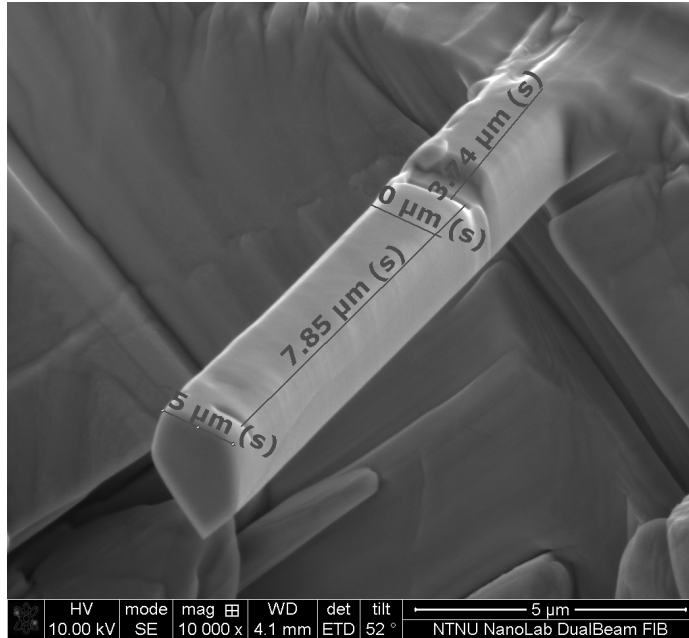
D.5 Cantilever 2-3 CGHAZ



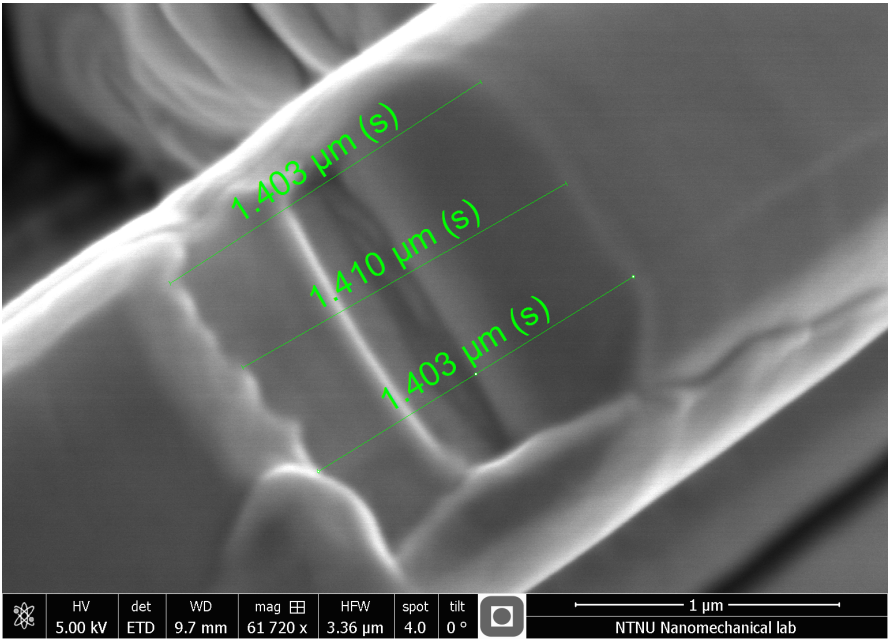
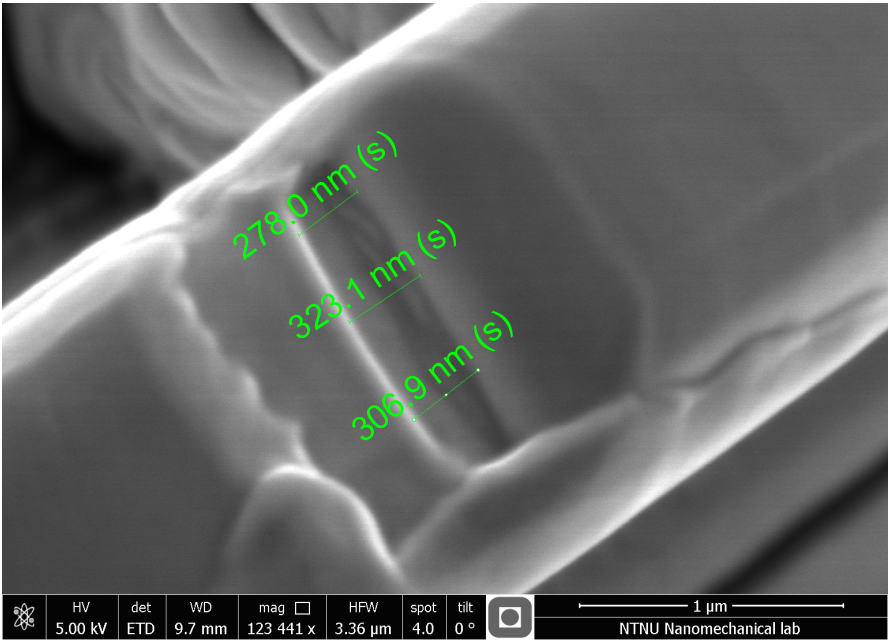
D SEM IMAGES OF CANTILEVERS AND PILLARS

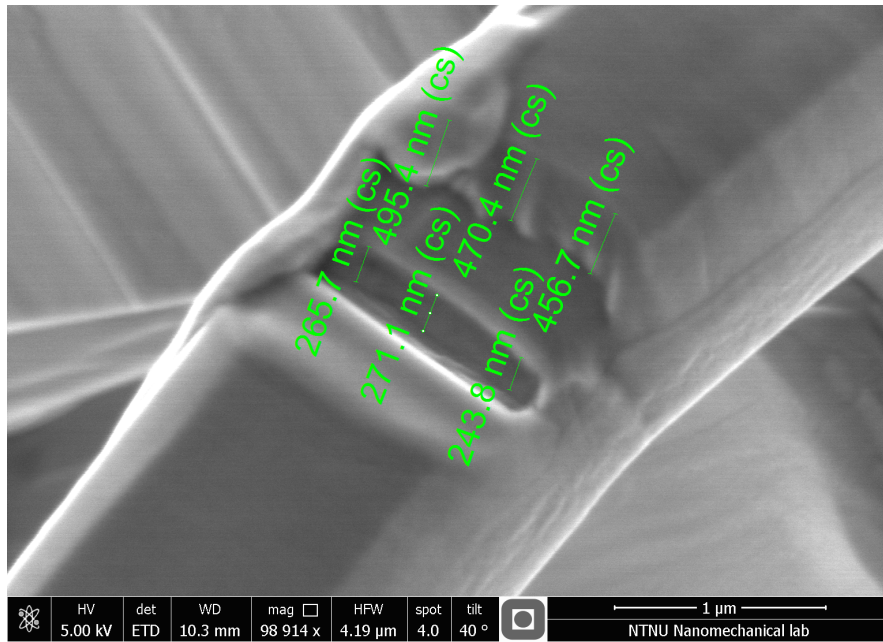


D.6 Cantilever 2-4 CGHAZ

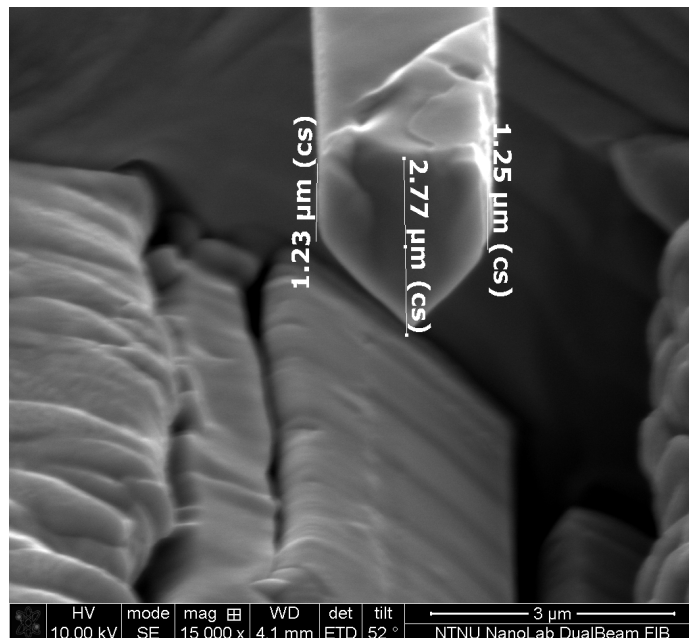
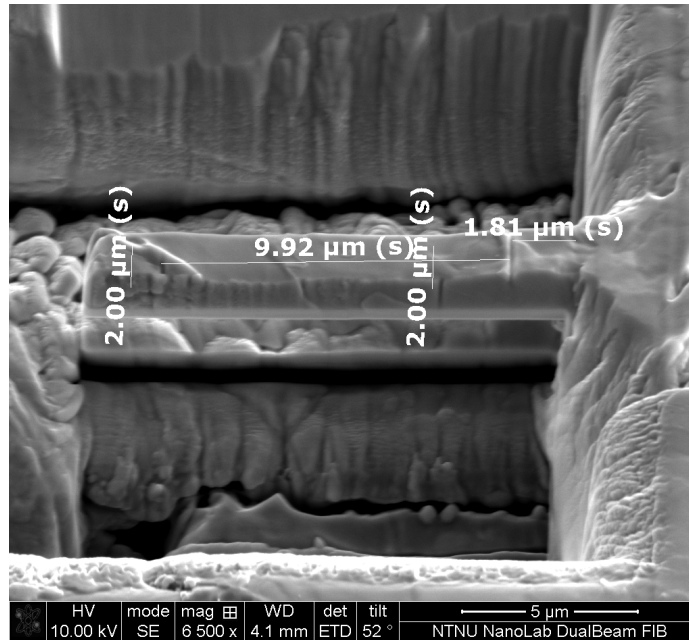


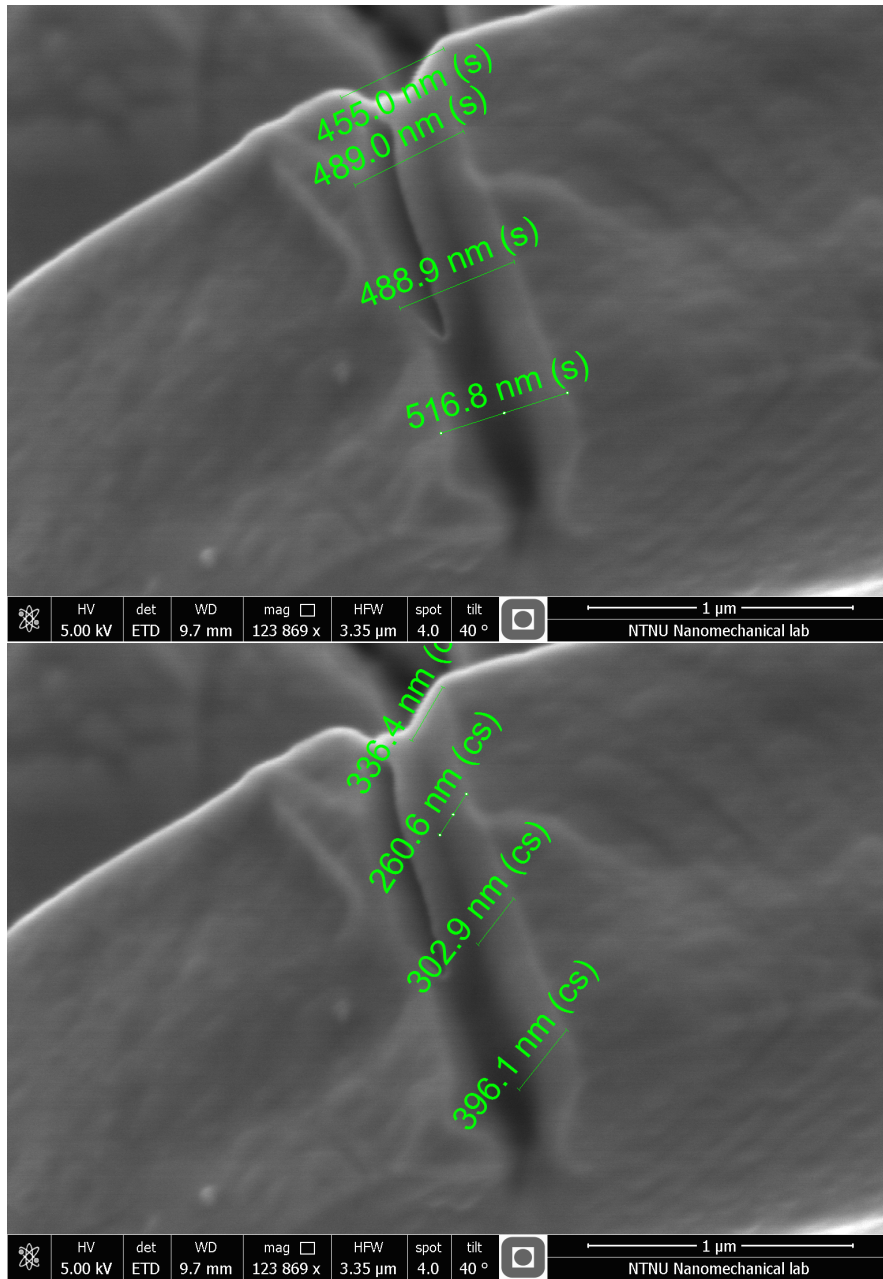
D SEM IMAGES OF CANTILEVERS AND PILLARS



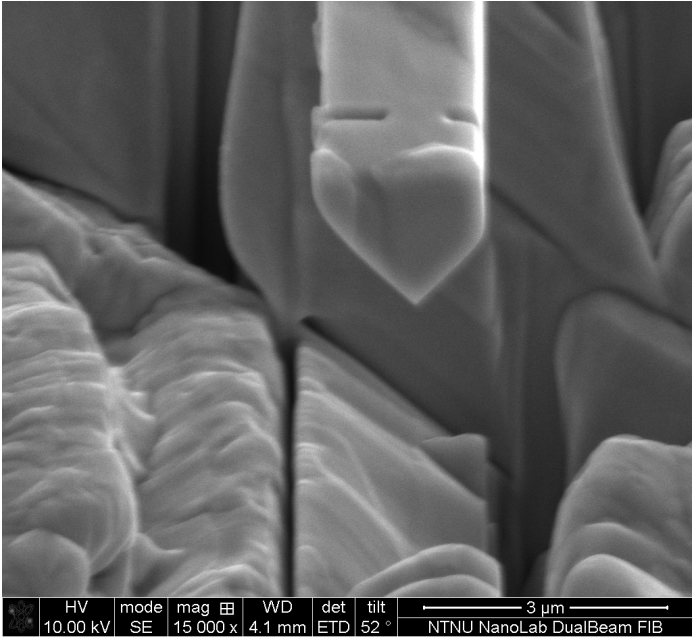
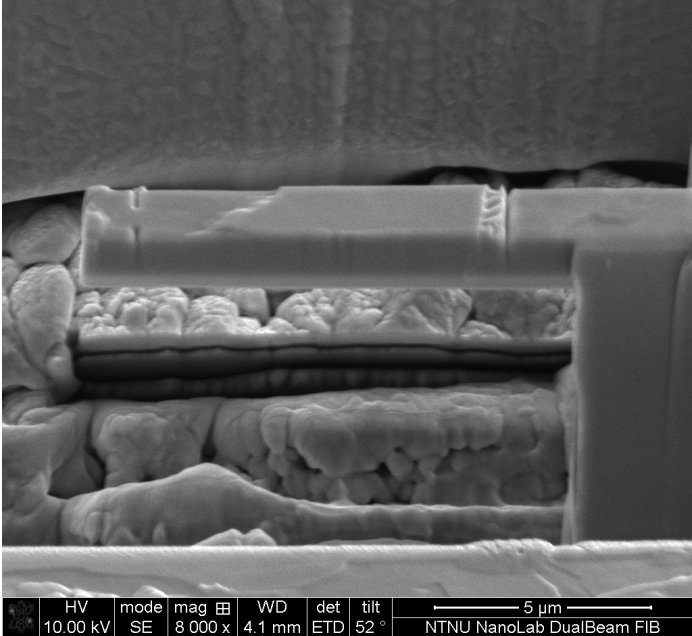


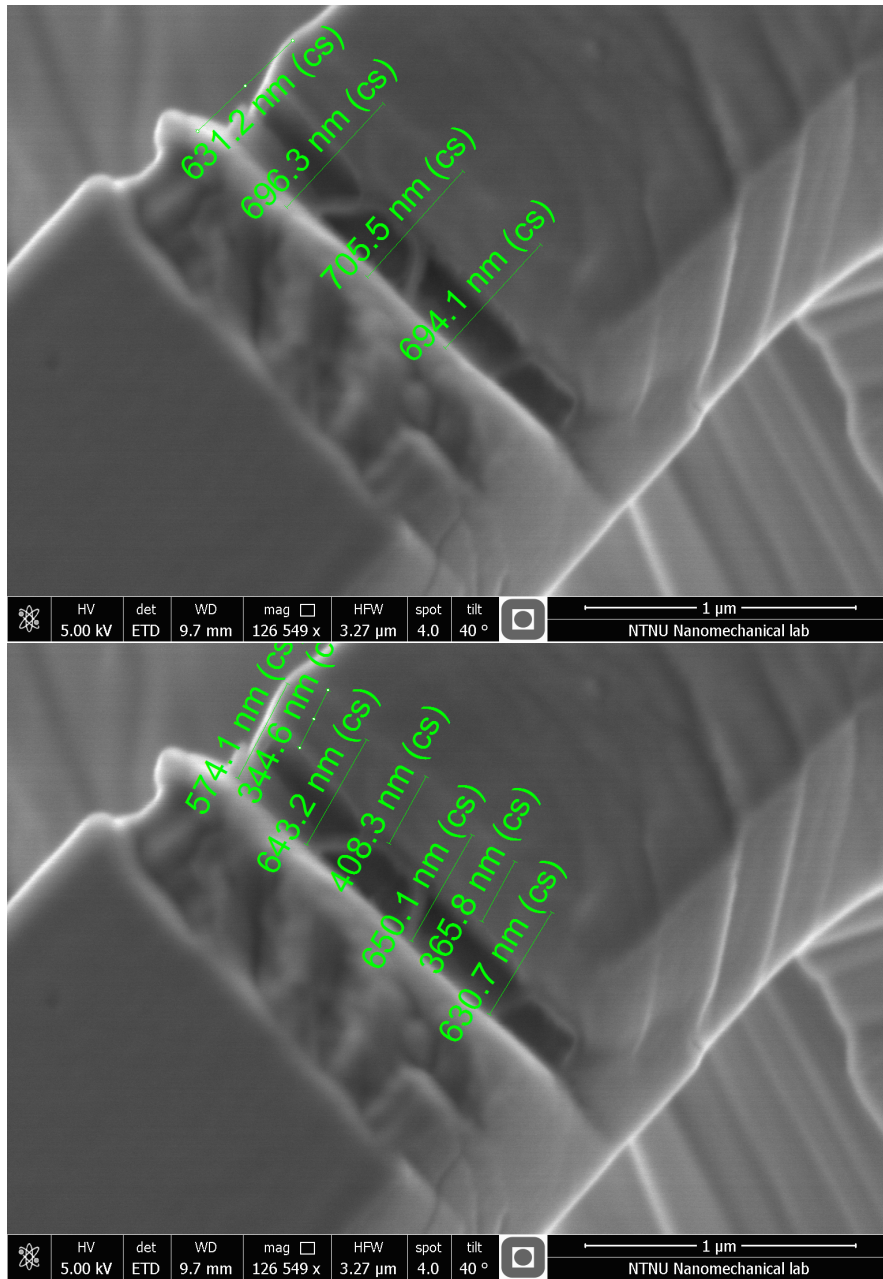
D.7 Cantilever 2 ICCGHAZ



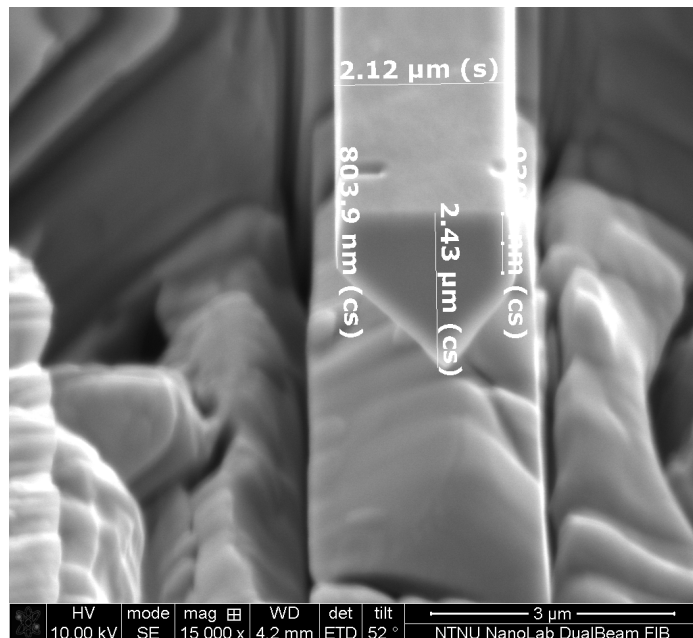
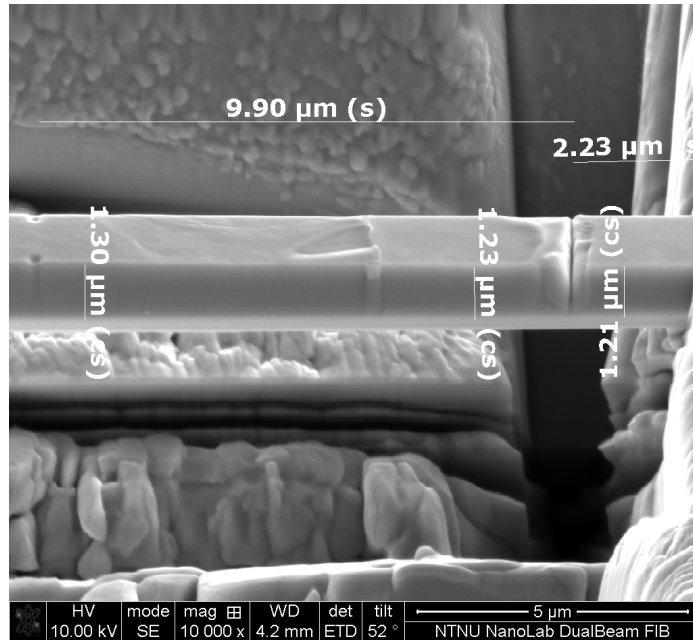


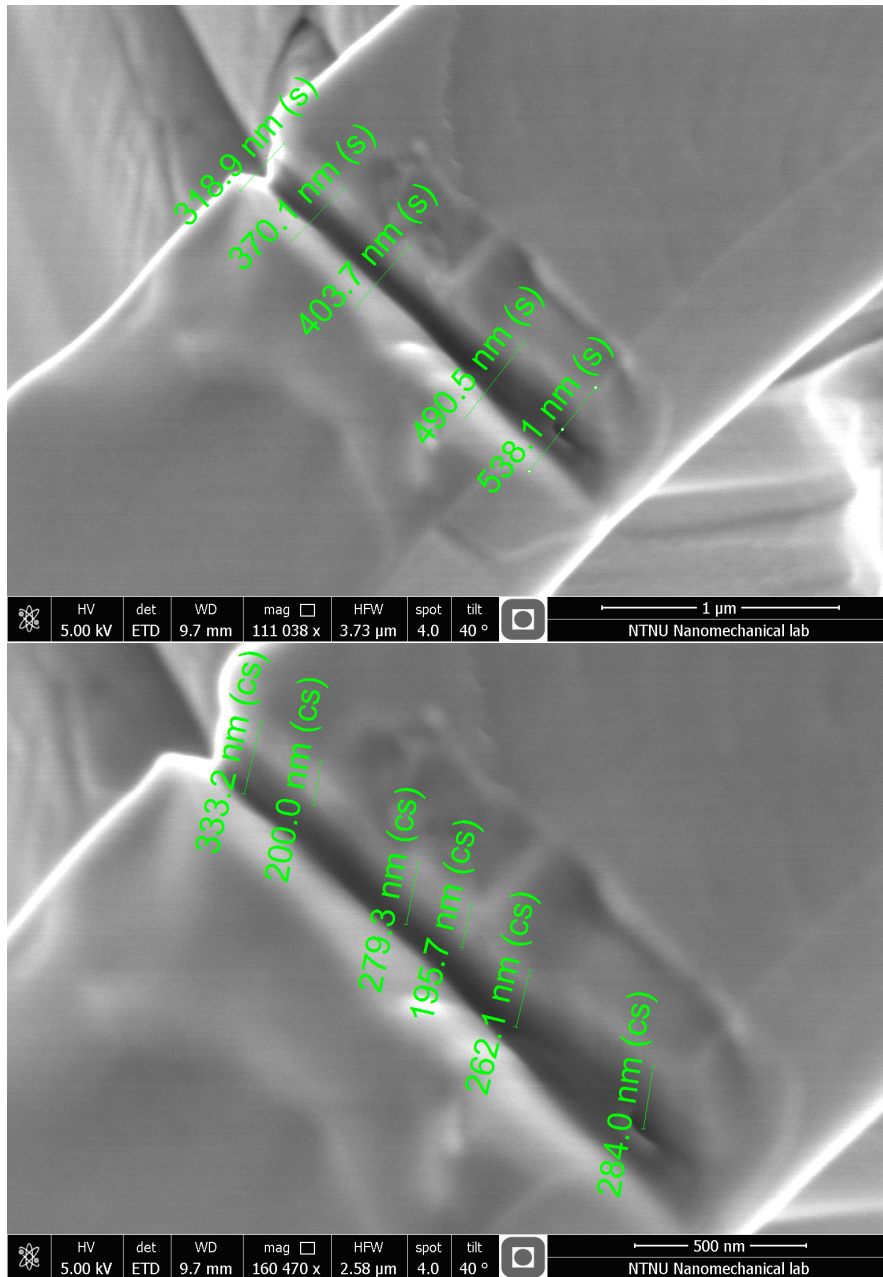
D.8 Cantilever 3D ICCGHAZ



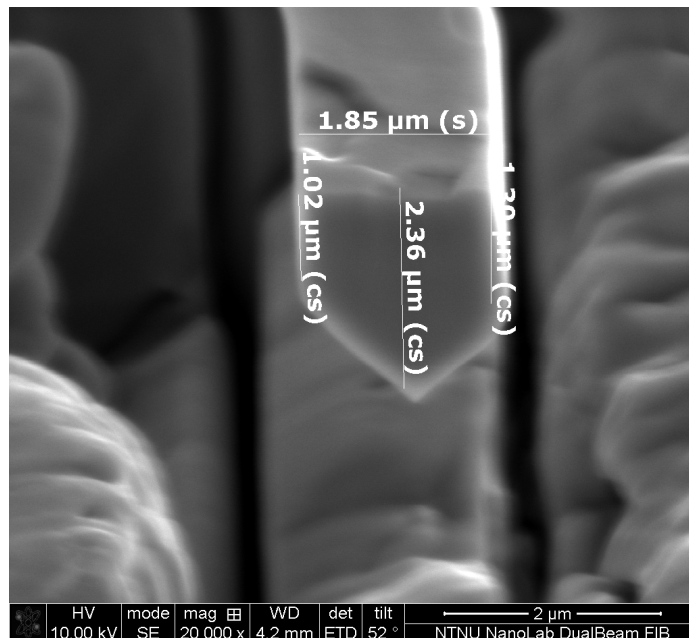
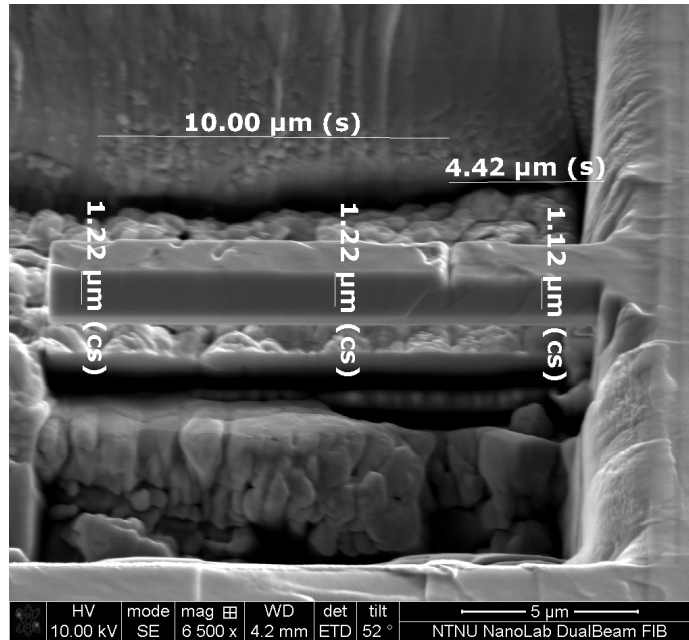


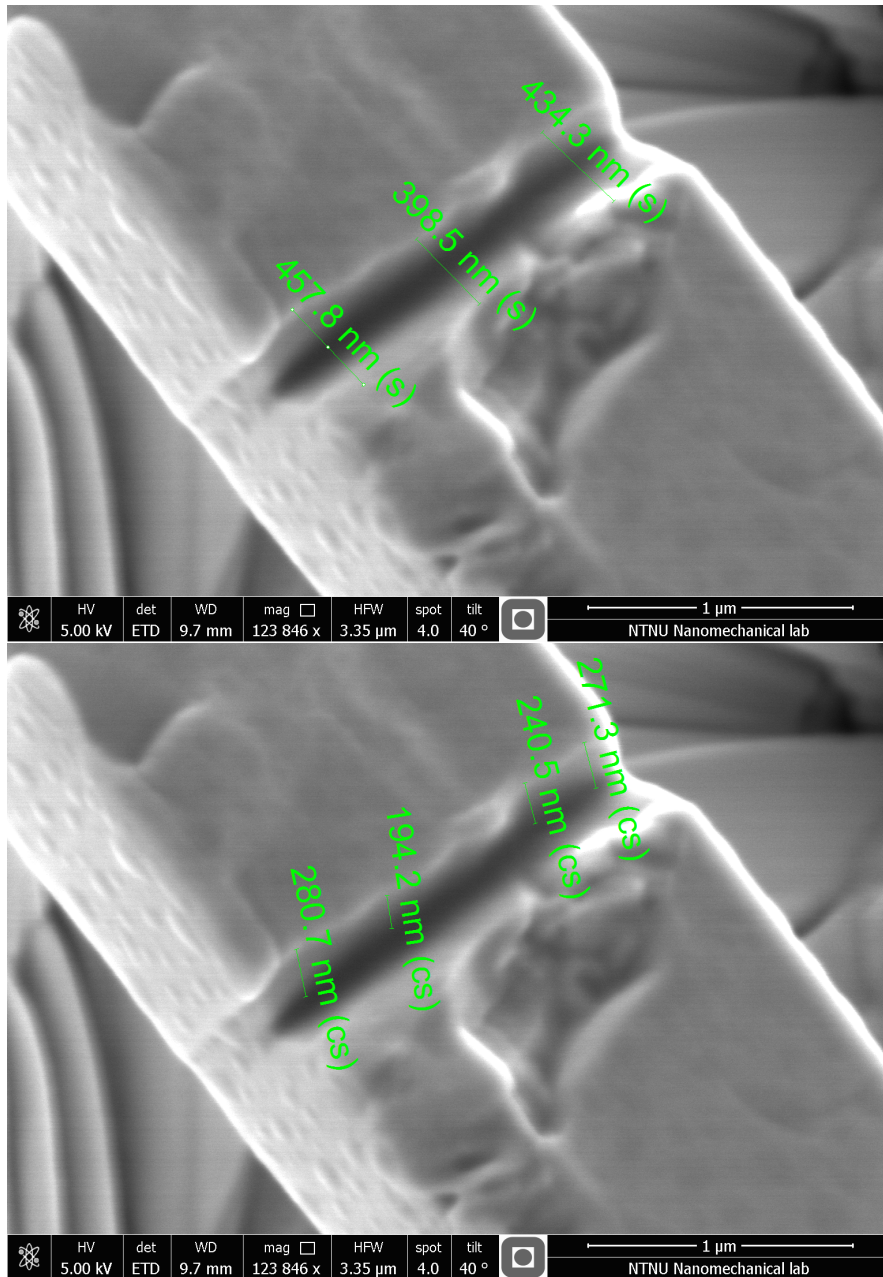
D.9 Cantilever 4 ICCGHAZ



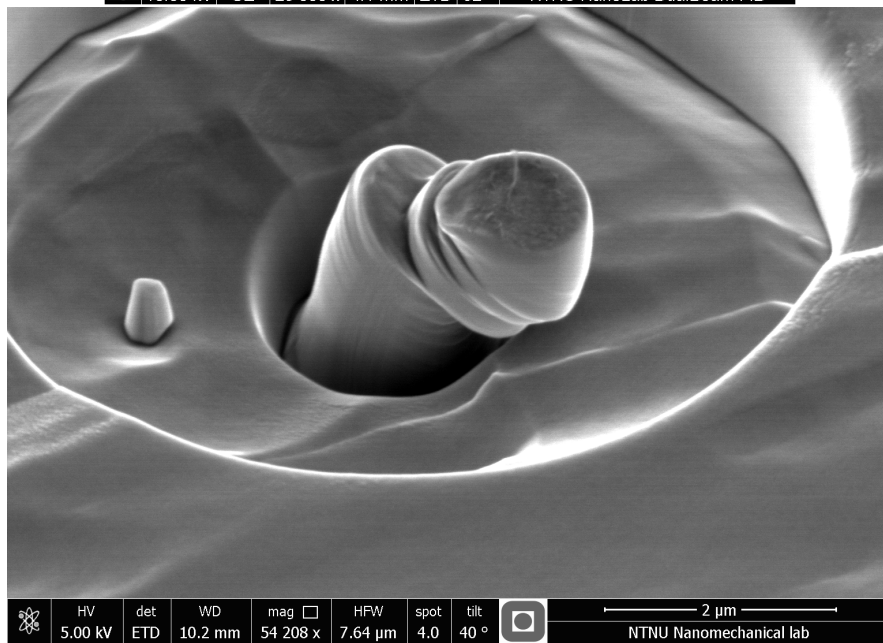
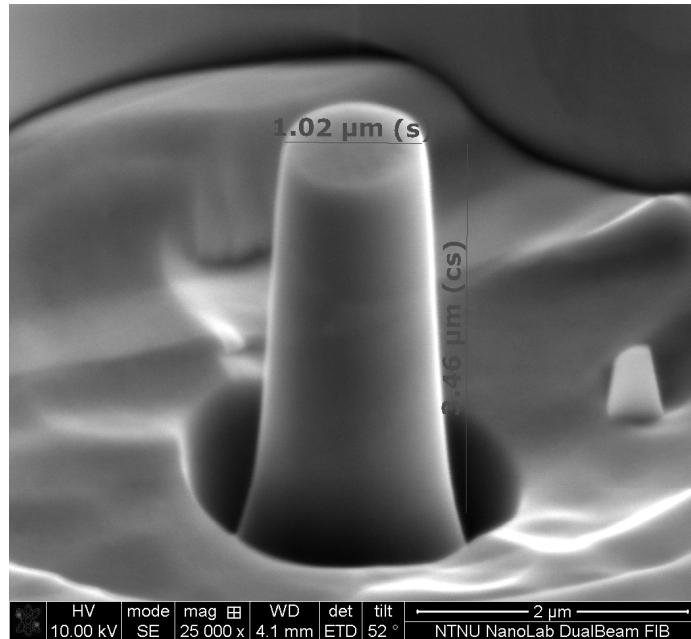


D.10 Cantilever 5D ICCGHAZ

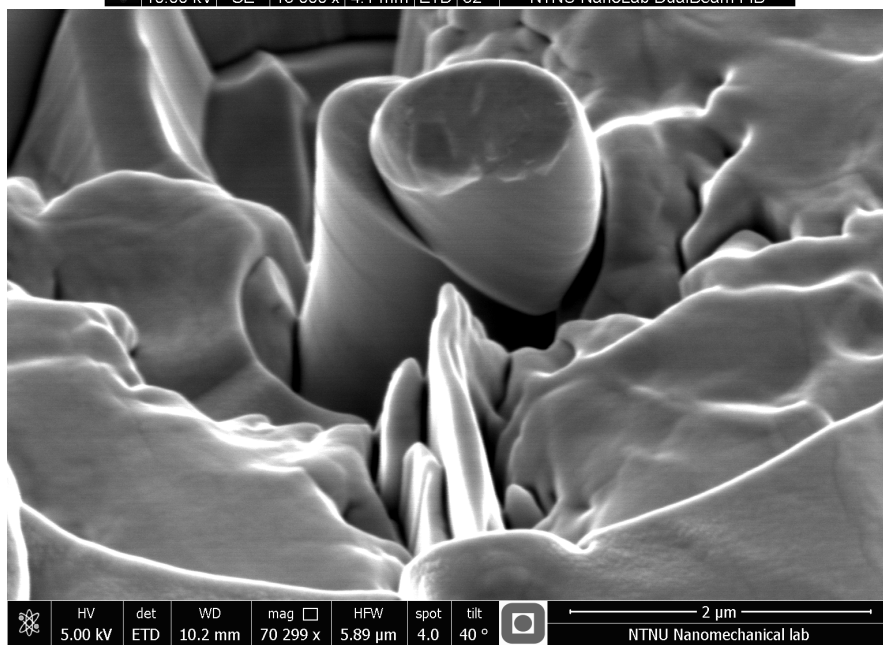
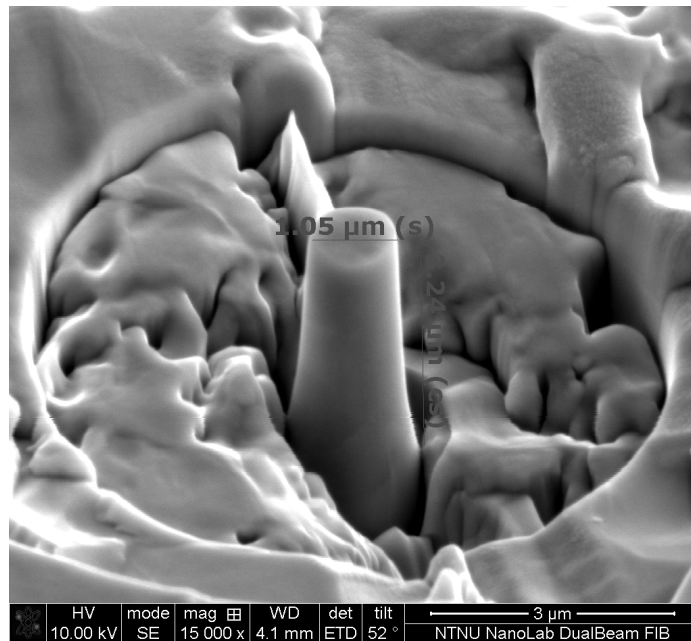




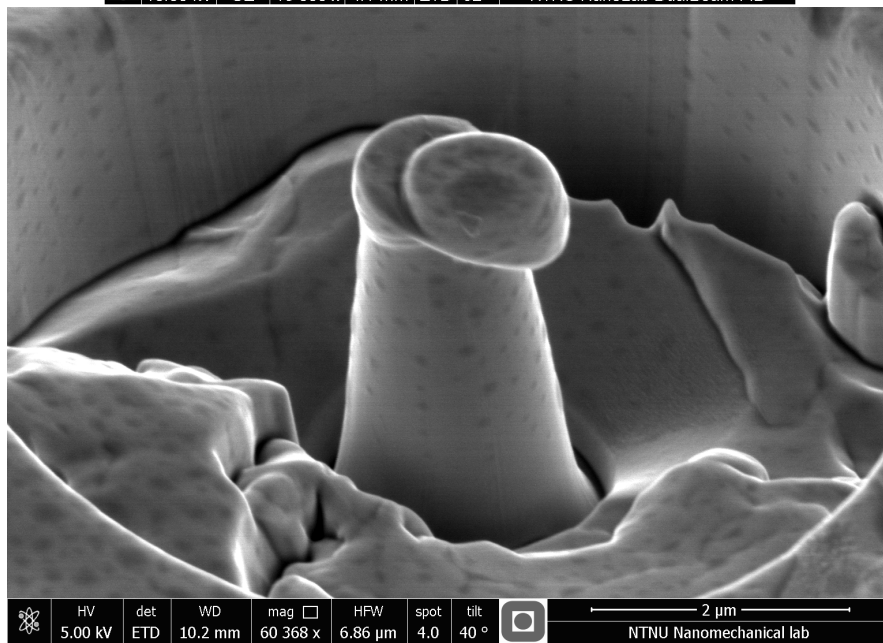
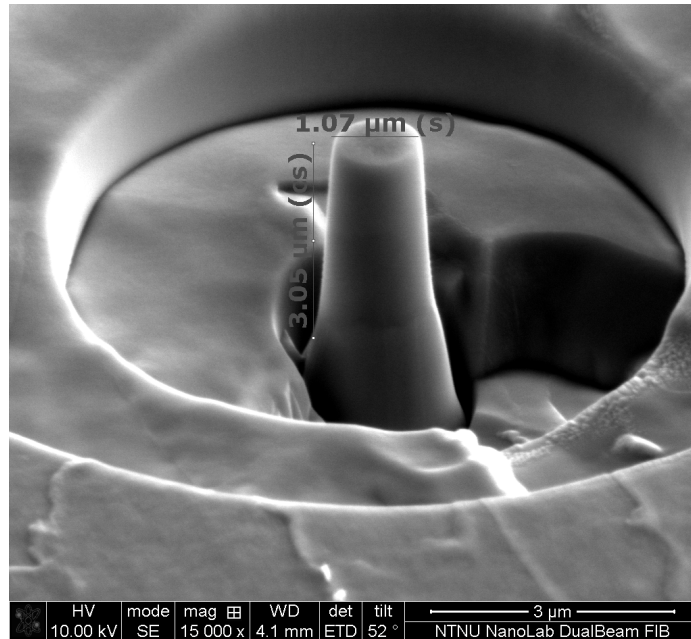
D.11 Pillar 4-1 CGHAZ



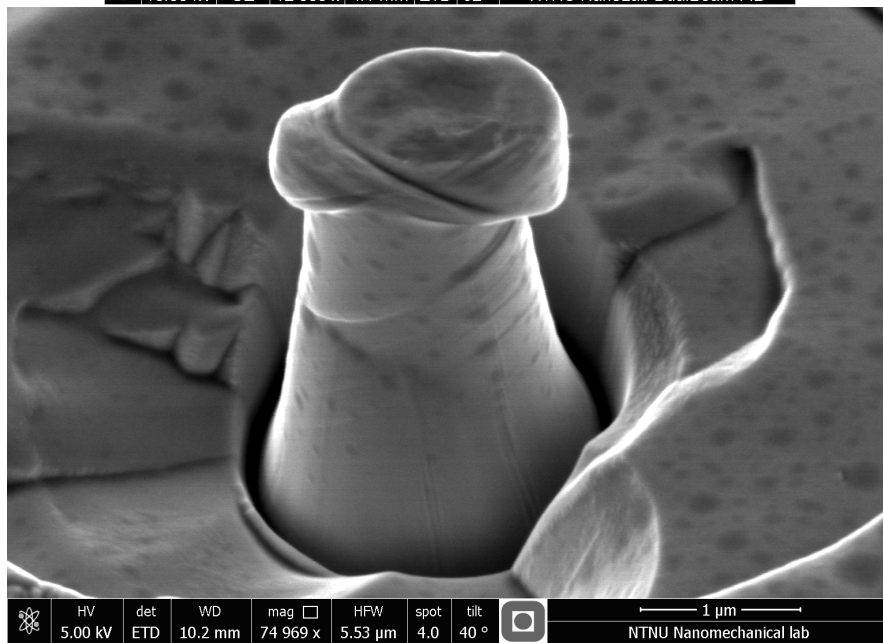
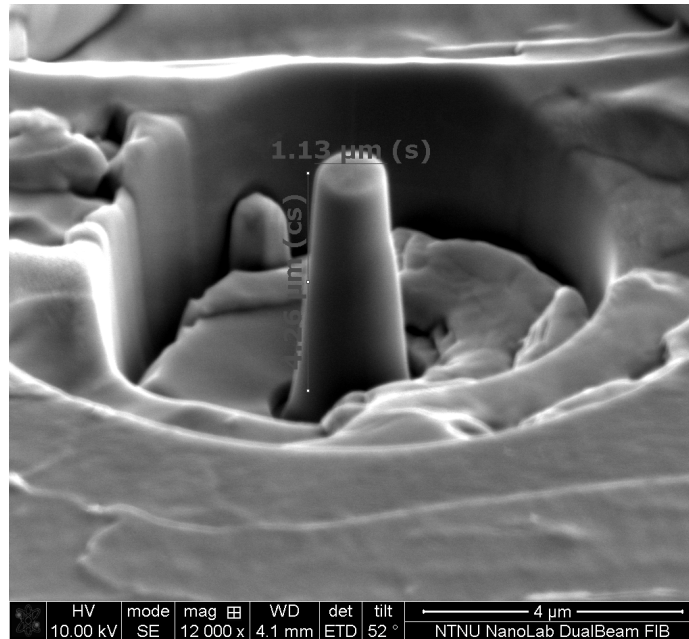
D.12 Pillar 4-2 CGHAZ



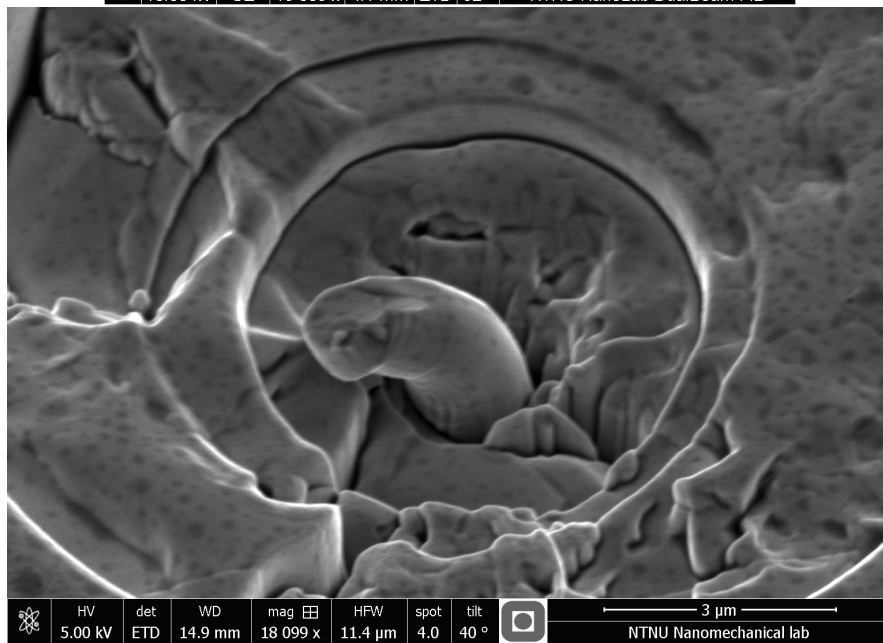
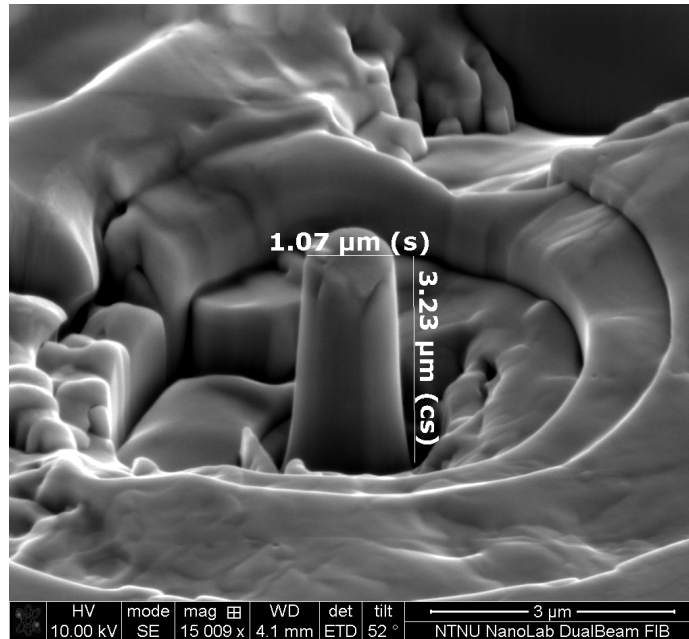
D.13 Pillar 6-1 CGHAZ



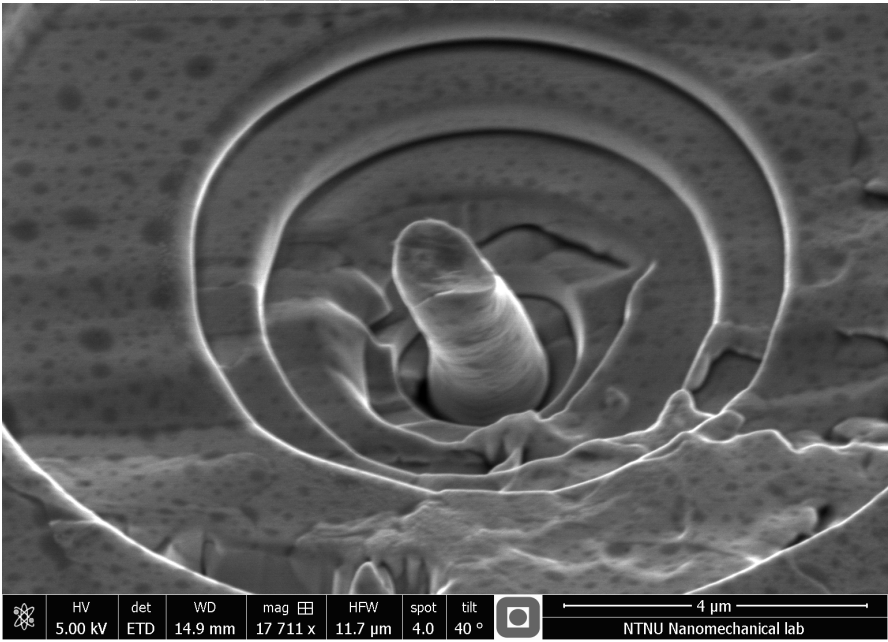
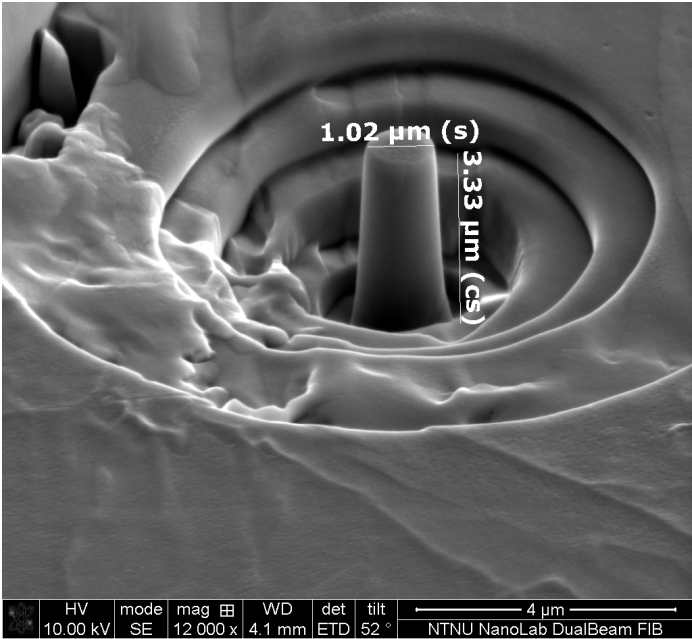
D.14 Pillar 6-2 CGHAZ



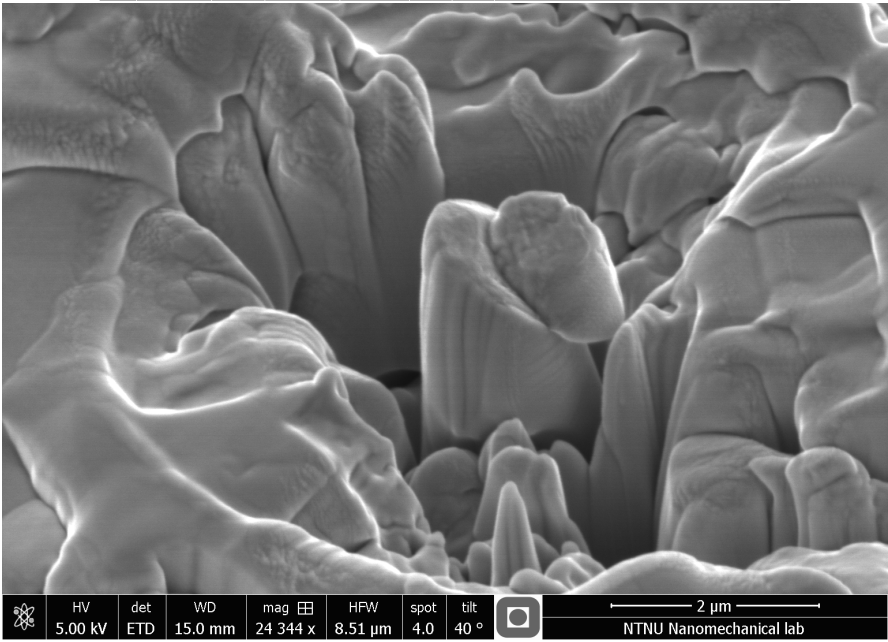
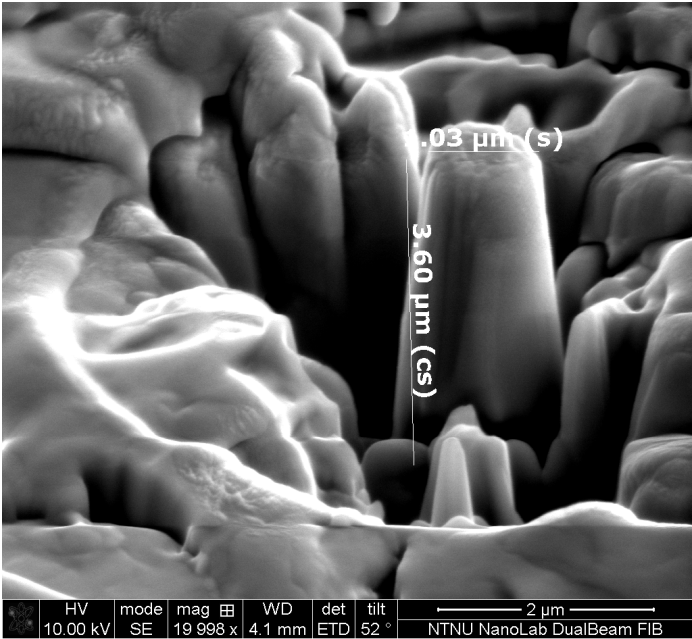
D.15 Pillar 7 ICCGHAZ



D.16 Pillar 8 ICCGHAZ



D.17 Pillar 10 ICCGHAZ



D.18 Pillar 11 ICCGHAZ

